SESSION

MEDICAL DEVICES AND SUPPORTING SYSTEMS

Chair(s)

TBA

Leakage Current Compensation in Switched Capacitor Circuits for Implantable Cardiac Devices

Santosh Koppa
Department of Electrical and Computer Engineering
UTSA, San Antonio, TX 78249, USA
qwd085@my.utsa.edu

Eugene John
Department of Electrical and Computer Engineering
UTSA, San Antonio, TX 78249, USA
eugene.john@utsa.edu

Abstract— **In this paper, the design and analysis of two circuits for leakage current compensation in switched capacitor sample and hold circuit used for low frequency biomedical devices such as pacemakers are presented. Both the circuits are analyzed using HSPICE simulation in 180nm technology node and the results show that both the circuits are capable of reducing the voltage drift by at least 14 times compared to the conventional sample and hold (S/H) circuit without adding significant chip area overhead. The first circuit consumes a current of ~5nA, but the rate of voltage drift is dependent on input level. The second circuit presented has a constant low voltage drift irrespective of the input voltage level.**

I. Introduction

Analog circuits are generally designed in long channel CMOS technology nodes which have less leakage currents. Leakage currents are negligible in most of the high speed S/H switched capacitor circuits and hence it is seldom considered while designing analog circuits [8]. As the device dimension decreases, leakage current increases and hence leakage current has to be considered while designing analog circuits for low sampling rate and low power circuits. For low speed implantable biomedical devices such as pacemakers, the charge that is sensed from the sensor or probe is sampled by a CMOS switch on to an on-chip capacitor [1]. The on-chip capacitor typically is in the range of few 100fF to few pico Farads. In the case of pacemakers, the data is sampled few times in a second approximately at a rate of 10 samples/s. Once the input is sampled, the charge must be held for approximately 100ms before being read by the readout circuit. During this large hold time, the charge is continuously leaked from the capacitor through the switch when the switch is turned off. Hence the sampled input and output read out during hold time is not the same. Also, the ambiguity of the read out output is high because the rate at which the capacitor leaks during the hold time depends on the input voltage level [9].

Fig.1 shows the conventional sample and hold circuit. In this figure M_{n2} and M_{p2} (minimum size) form the switch, M1 is the source follower amplifier. When the switch is turned on, V_{in} is sampled on to C_{sig}. V_{con} is equal to V_{in} before the switch is turned off. After the switch is turned off, the charge is either leaked to V_{dd} or to ground or to V_{in} through subthreshold conduction. There are three leakage mechanisms [2] identified in switches; namely subthreshold conduction, drain-bulk diode leakage and accumulation mode source-drain coupling. Fig.2 shows the simulation results of conventional S/H circuit. It shows the ideal S/H output V_{ideal} and conventional S/H output V_{con} when the switch is turned off. It can be observed that once the switch is off, the charge on the capacitor starts to leak towards V_{dd}. The voltage V_{con} drifts at 1.4V/s during the hold time. This leakage in analog circuits changes the information read from the sensors. As the rate at which the voltage drifts is not constant, the readout information is unacceptable for ultra low power medical devices. Even though the leakage currents are inevitable for the near submicron devices, it can be minimized and can be compensated through feedback circuit techniques [1] or using super cut-off CMOS circuits [3]-[4] or by using clock gating scheme [5]. To address this problem, low leakage switches were proposed in [6] and [7] which could reduce the leakage through the switches minimizing the errors. Implantable devices such as pacemakers are powered by a battery with a typical lifespan of approximately 10 years and hence limits on power consumption are critical in the design of such devices. This paper presents the design and comparative leakage charge analysis of leakage reduction circuits in sample and hold circuit designed in 180nm technology node with 1.8V V_{dd}. These circuit techniques reduce the ambiguity in readout output.

Rest of this paper is organized as follows. Section II elaborates the design and simulation of leakage cancellation technique. Section III describes a simple feedback scheme to compensate for leakage. These two leakage reduction schemes are compared in section IV and the paper is concluded in section V.

II. Leakage cancellation feedback Technique

Voltage drift in conventional S/H circuit can be reduced by using a very large capacitor. The larger the sampling capacitor, the longer it takes for it to discharge and hence reduced ambiguity in readout output. However, this on chip capacitor covers large area and hence not feasible for implantable devices.

To effectively reduce the voltage drift and not to add significantly to the area of the chip, a leakage cancellation scheme was proposed in [1]. Fig.3 shows this leakage cancellation scheme with a feedback technique for S/H circuit. This scheme has a duplicate S/H circuit identical to main S/H circuit with less S/H capacitance; C_{sig}=500fF and C_{dup}=100fF, respectively. The M_{n1}, M_{n2}, M_{p1} and M_{p2} are minimum size transistors. Because C_{dup} is smaller than C_{sig}, voltage drift on C_{dup} (V_{dup}) is much higher than voltage drift on C_{sig} (V_{sig}). Both S/H values i.e. V_{sig} and V_{dup} are connected as input to single stage differential error amplifier.

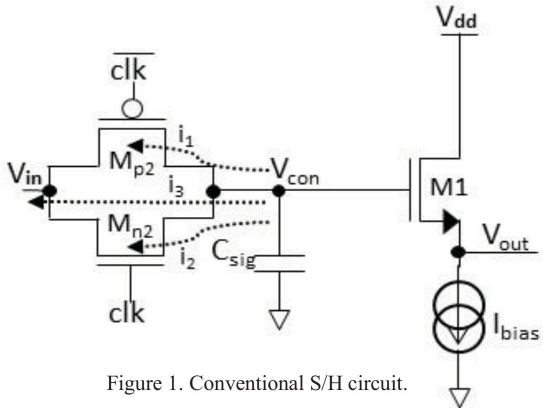

Figure 1. Conventional S/H circuit.

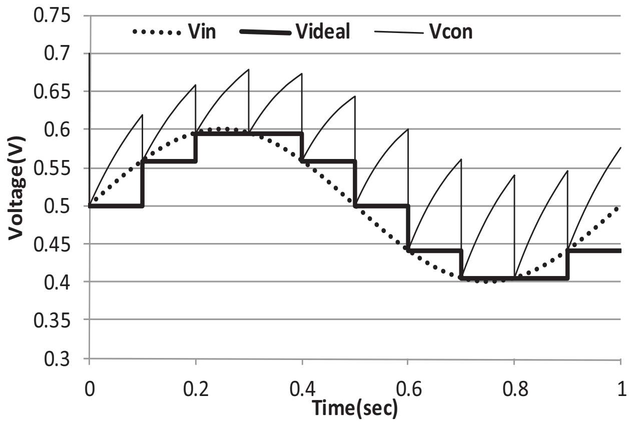

Figure 2. Conventional S/H circuit output and ideal S/H waveforms.

Length to Width (L/W) ratio of M1and M2 is 6 and L/W ratio for M3 and M4 is 13. M5-M8 (leakage transistors) has W/L ratio of 10 and M9-M12 are minimum size transistors. Output of leakage cancellation circuit is connected back to the S/H capacitors as shown in the figure. Error amplifier amplifies the difference between V_{sig} and V_{dup}. Output of the amplifier V_{amp} is connected to the leakage transistors and its output is fed back to the S/H capacitors.

This feedback compensates for the charge leaked and reduces the difference between V_{sig} and V_{dup}. Output of the amplifier becomes steady once the V_{sig} and V_{dup} are equal. The only difference between V_{sig} and V_{dup} is due to the amplifier offset voltage. Simulated waveforms are shown in Fig.4. The difference between the V_{sig} and V_{dup} signals reduces and approaches the offset voltage while minimizing the voltage drift during the hold time and hence maintains the sampled voltage.

This technique can reduce the voltage drift of 140mV in conventional S/H circuit to a maximum voltage drift of 10mV during one sampling period which is about 100ms in our simulations. This technique reduces the voltage drift by approximately 14 times compared to the conventional S/H circuit with least constraint to the area.

In this circuit, the rate of voltage drift depends on the input being sampled and hence the voltage drift is not same for each sampled voltage for a fixed hold time. It can achieve close to ideal S/H output by increasing the gain of the amplifier. Voltage difference between V_{sig} and V_{dup} is given by Equation (1).

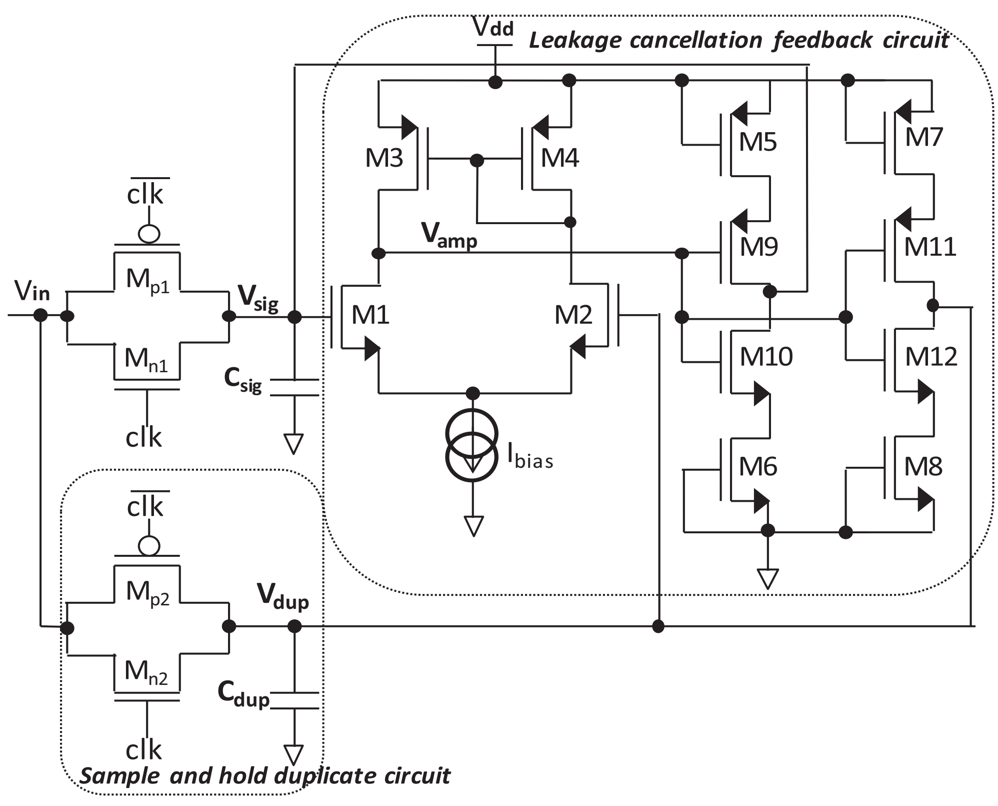

Figure 3. Leakage current cancellation scheme for S/H circuit.

$$Vdiff = \frac{Vamp}{Av} + Voffset \qquad (1)$$

Where V_{amp}, Av and V_{offset} is amplifier output, voltage gain and input offset voltage of the amplifier respectively.

From the simulation results it can be observed that the rate of voltage drift on V_{sig} changes for each hold period. In the first S/H time, the voltage drift is about 10mV and the sample at 0.3s the voltage drift is just 5mV by the end of hold time. The rate of voltage drift on V_{sig} is given by Equation (2)

$$\frac{dVsig}{dt} = \frac{Idiff}{Csig - Cdup} \qquad (2)$$

where I_{diff} is the current difference between the main S/H circuit and duplicate S/H circuit. To minimize the rate of voltage drift, difference between C_{sig} and C_{dup} must be increased. This rate of voltage drift can also be attributed to the dependency of the leakage current based on the potential at V_{in} when the switch is turned off. The higher the input voltage the higher will be the rate of voltage drift towards ground. To reduce the rate of voltage drift based on input, this paper presents a simple but effective feedback circuit in the next section.

Most of the power consumed in this technique is by the amplifier. This circuit was simulated in HSPICE and the simulation results show that the current consumption was approximately ~5nA. Leakage transistors M5-M12 consumed negligible current.

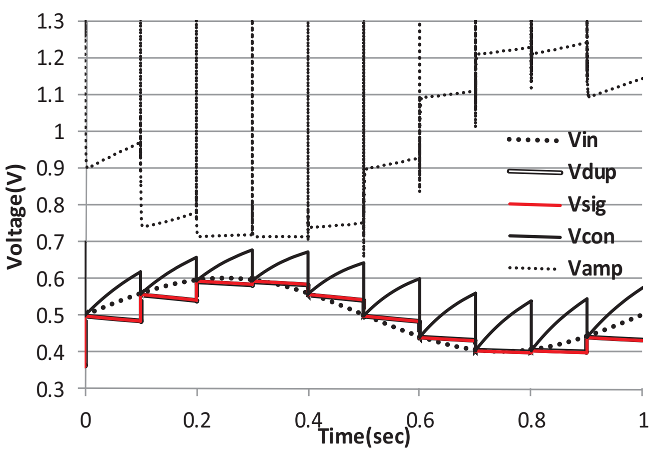

Figure 4. Output waveforms with and without leakage cancellation feedback technique for S/H circuit.

III. LEAKAGE COMPENSATION FEEDBACK TECHNIQUE

Fig.5 shows a novel and simple negative feedback leakage compensation circuit which uses only two transistors and a feedback capacitor. Transistor M_{p2} and M_{n2} are minimum size transistors which form the S/H switches. C_{sig} is the S/H capacitor, C_{com} is compensation capacitor. M1 and M2 form a simple common source amplifier. As the voltage V_{com} drifts due to charge leakage in C_{sig}, the amplifier amplifies the change in V_{com} and output of the amplifier V_{out} is fed back to V_{com} through C_{com}. This setup is in negative feedback configuration and hence the charge leaked in C_{sig} is compensated back through C_{com}. The rate of voltage drift at V_{com} is independent of input voltage and only depends on the C_{com}/C_{sig} ratio. Higher the ratio lower will be the voltage drift and the limit can be set by the area constraint.

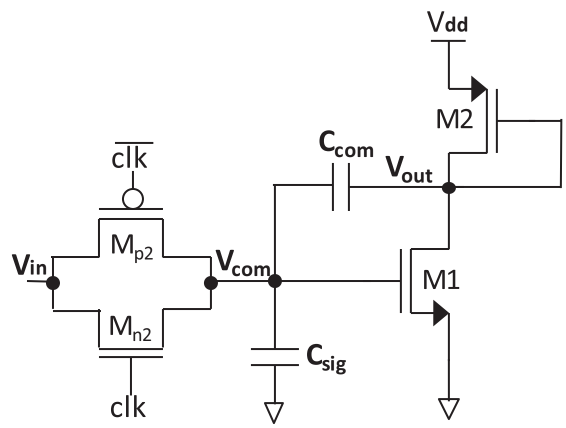

Figure 5. Leakage compensation S/H circuit.

Fig.6 shows the simulation results for the proposed circuit with C_{com}/C_{sig} = 6 and $(W/L)_{M1}$ /$(W/L)_{M2}$ = 10. From the simulation results, it can be observed that the voltage drift at the end of the hold time is approximately 10mV which is constant and independent of the input V_{in}. This circuit consumed a maximum current of approximately 0.7uA which is due to the diode connected transistor load (M2) of the amplifier.

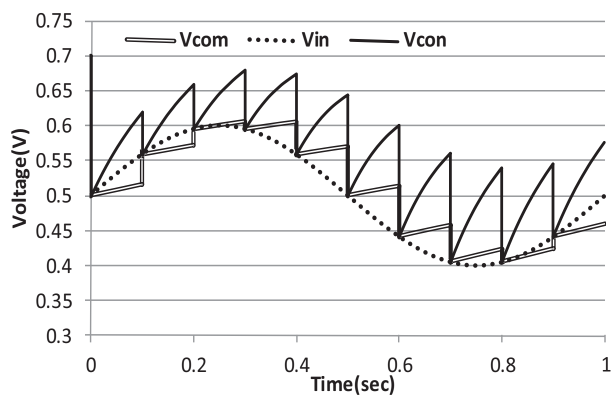

Figure 6. Output waveforms with and without leakage compensation feedback technique for S/H circuit.

IV. COMPARATIVE ANALYSIS

All the circuits analyzed in this paper were simulated in 180nm TSMC technology node using HSPICE. Both S/H leakage reduction feedback circuits could achieve very low voltage drift of 10mV (V_{sig}, V_{com}) during the hold period while the conventional S/H voltage drifted by 140mV (V_{con}) during the same hold period. Fig.7 shows the simulation results for both the circuits. V_{sig} drifts towards ground while V_{com} drifts towards V_{dd}. To measure the rate of voltage drift based on input, a ramp input signal was applied to V_{in}. Fig.8 shows the simulation results for the two leakage compensation circuits and conventional S/H circuit for a ramp input. For low V_{in}, rate of voltage drift at V_{sig} is low. As V_{in} increases, the rate of voltage drift increases. V_{sig} has a voltage drift ranging from 10mV-700mV for the input changing from 0V to 1.8V for a hold period of 100ms. This makes the circuit useful for only low input voltage levels. This input dependency can be attributed to the linearity and input voltage limitations of the feedback amplifier. In conventional S/H circuit, V_{con} drifts towards V_{dd} for low V_{in} and drifts towards ground for higher V_{in}. V_{con} has a drift ranging from 10mV to 250mV for rail-rail input swing. V_{com} has a fixed voltage drift of 10mV which is independent of rail-rail V_{in} swing as shown in the simulation result. Table.1 summarizes the comparison results with its advantages and disadvantages.

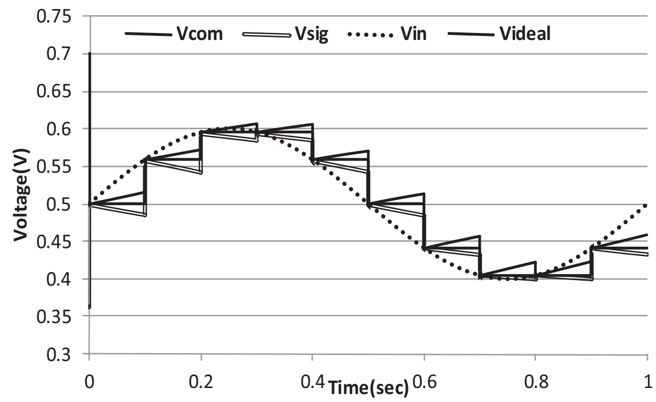

Figure 7. Comparison of voltage drift for both the feedback techniques.

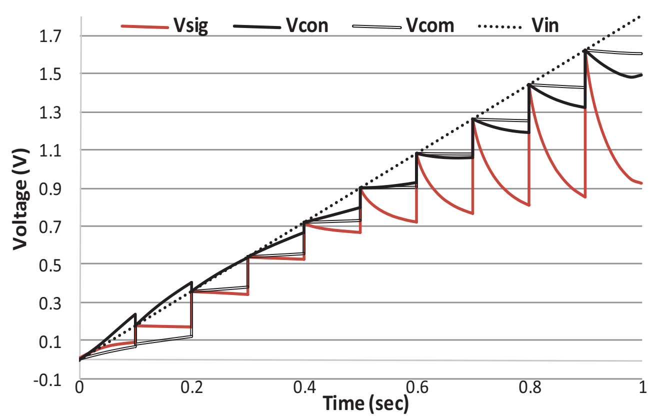

Figure 8. Comparison of voltage drift for ramp input.

V. CONCLUSIONS

In conclusion, in this paper we proposed and demonstrated two circuit designs which can reduce the voltage drift in a S/H circuit used for low power biomedical systems using feedback mechanism. The proposed circuits are able to reduce the voltage drift to 10mV as compared to 140mV drift for conventional S/H circuit. The first circuit had the input dependent voltage drift while the second circuit had input independent constant voltage drift. The first proposed leakage cancellation circuit consumed very less current and can reduce the voltage drift for small input levels. The second leakage compensation circuit consumed high current while having low voltage drift for rail-rail input swing.

TABLE I. PERFORMANCE COMPARISON OF DIFFERENT S/H CIRCUITS.

Circuit approach	Current consumption	Tech	Adv/Disadv
Uncompensated [1]	~30nA	0.5µm	Unacceptable drift
Compensated with larger sampling capacitor [1]	~200nA	0.5µm	Large area and current
Leakage cancel circuit [1]	~38nA	0.5µm	Small area, input dependent drift
Leakage cancellation circuit (Proposed Circuit 1) (Fig.3)	~5nA	0.18µm	Low power, small area, input dependent drift
Leakage compensation circuit (Proposed circuit 2) (Fig.5)	~0.7uA	0.18µm	Small area, input independent low drift, high power

Acknowledgement

Research reported in this paper was supported in part by National Institute of General Medical Sciences of the National Institutes of Health under award number 1SC3GM096937-01A1. The content is solely the responsibility of the authors and does not necessarily represent the official views of the National Institutes of Health

REFERENCES

[1] Wong, L. S., et al. (2001). Leakage current cancellation technique for low power switched-capacitor circuits. Proceedings of the 2001 international symposium on Low power electronics and design, ACM.

[2] Wong, L. S. Y., et al. (2004). "A very low-power CMOS mixed-signal IC for implantable pacemaker applications." Solid-State Circuits, IEEE Journal of 39(12): 2446-2456.

[3] Ishida, K., et al. (2005). Subthreshold-leakage suppressed switched capacitor circuit based on super cut-off CMOS (SCCMOS). Circuits and Systems, 2005. ISCAS 2005. IEEE International Symposium on.

[4] Kawaguchi, H., et al. (2000). "A super cut-off CMOS (SCCMOS) scheme for 0.5-V supply voltage with picoampere stand-by current." Solid-State Circuits, IEEE Journal of 35(10): 1498-1501.

[5] Min, K.-S., et al. ZigZag Super Cut-off CMOS (ZSCCMOS) Block Activation with Self-Adaptive Voltage Level Controller: An Alternative to Clock-Gating Scheme In Leakage Dominant Era, 2003 IEEE International Solid-State Circuits Conference, Feb. 12, 2003, Salon.

[6] Abhari, M. A. and A. Abrishamifar (2009). A novel ultra low-leakage switch for switched capacitor circuits. GCC Conference & Exhibition, 2009 5th IEEE.

[7] Lee, W. F. and P. K. Chan (2005). "An injection-nulling switch for switched-capacitor circuit applications." Instrumentation and Measurement, IEEE Transactions on 54(6): 2416-2426.

[8] Annema, A.-J., et al. (2005). "Analog circuits in ultra-deep-submicron CMOS." Solid-State Circuits, IEEE Journal of 40(1): 132-143.

[9] Mingliang Liu, "Demystifying switched capacitor circuits," 1st ed. MA, USA: Elsevier, April 2006, Ch.2, pp. 31.

Digital Blood Pressure Estimation with the Differential Value from the Arterial Pulse Waveform

Boyeon Kim[1] and Yunseok Chang[2]

[1]Department of Computer Engineering, Daejin University, Pocheon, Korea, 487-711
[2]Department of Computer Engineering, Daejin University, Pocheon, Korea, 487-711

Abstract –*In this study, we proposed the new method to estimate the blood pressure with the differential value of the digital arterial pulse waveform and BP relation equation. To get the digital arterial pulse waveform, we designed and implemented the arterial pulse waveform measurement system acquires from the digital air-pressure sensor device and transmits to the smartphone app through the Bluetooth communication. The acquired digital arterial pulse waveforms are classified as hypertension group, normal group, and hypotension group, and we can derive the average differential value between the highest point and lowest point of a single waveform of individuals along with the group. In this study, we found the functional correlation between the blood pressure and differential value as a form of BP relation equation through the regression process on the average of differential value and blood pressure value from a tonometer. The Experimental results show the BP relation equation can give easy blood pressure estimation method with high accuracy. Although this estimation method gives somewhat poor accuracy for the diastolic, the estimation results for the systolic show the high accuracy more than 90% compare to the commercial tonometer.*

Keywords: Digital arterial pulse waveform, Blood pressure measurement, Differential value, BP relation equation, Non-Kortokoff method

1 Introduction

The blood pressure measurement is a sort of the basic medical treatment and the blood pressure is one of the most important biomedical signals of one's health status. Therefore, every medical staff always measures and checks a patient's blood pressure and health status at the hospital. There are two traditional methods to measure a patient's blood pressure so called the Kortokoff's method and the oscillometric method. These methods have been used for a long time on lots of medical devices, and still adopted on the current electronics tonometer [1]. But the Kortokoff-type tonometer attacks the arteries and veins by high pressure until blocking the blood current, it would hurt the blood vessels. This is why the traditional methods have a great drawback that cannot be applied to a patient repetitive or continuous blood pressure measurement [2]. Therefore, we need a Non-Kortokoff blood pressure measurement method that can measure the blood pressure continuously without blocking the blood vessel.

1.1 Aim of the continuous blood pressure measurement

In many cases, hypertensives or pregnant women have to measure or monitor the blood pressure variation 24-hours continuously. Since the traditional Kortokoff-type tonometer has to block the blood current completely and release the vessel slowly, many trials cause a serious damage to the patient's artery or vein and make some dangerous hemorrhage in many cases. So we have to take continuous blood pressure measurement with a non-Kortokoff method not to press the blood vessel. If we can try to measure the blood pressure without heavy press on the vessel, we can check the blood pressure over 24-hours and more continuously [3]. In this study, we measured the arterial pulse waveform that represents the continuous pressure variation of the blood current in the artery by using the digital sensor unit and smartphone app, and composed the blood pressure estimation algorithm with the differential value of the arterial pulse waveform. With this method, we don't have to block the artery or to press the vessel deeply that can take a long time period blood pressure measurement.

1.2 Arterial pulse waveform measurement

The arterial pulse waveform from a digital sensor unit can be described as two types of waveform, integral waveform and differential waveform. The differential waveform shows the series of the blood pressure variation per unit time and the integral waveform shows the series of the blood pressure value itself as time flows. Figure 1 shows the same blood pressure variation with the differential waveform (a) and integral waveform (b) respectively.

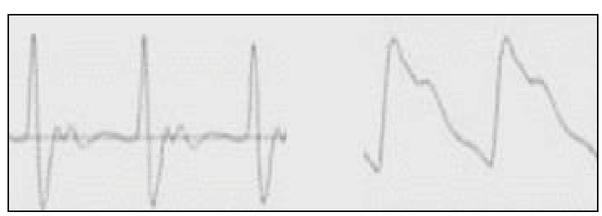

a) Differential form **b) Integral form**

Figure 1 Arterial pulse waveform

Since blood pressure is the pressure value of blood current directly oppresses the vessel, the integral waveform has more advantages than differential waveform to find out the relation between the blood pressure and arterial pulse waveform. Therefore, we adopted the integral type digital sensor unit that can produce a series of the digital signal in a form of the integral waveform that can be used to estimate the blood pressure value such as systolic and diastolic.

The remaining part of this paper is organized as follows: Section 2 describes the related works and studies concerned with the proposed method; in Section 3 we defined the relation between the arterial pulse waveform and blood pressure and in Section 4 we provide the experimental environment that carries the proposed method; Section 5 contains analysis of the proposed method including blood pressure relation equation, blood pressure estimation, and its experimental evaluations; the paper is concluded with some summarizing remarks and further studies in Section 6.

2 Related works

The blood pressure measurement has been studied by lots of researchers through various ways of the method for a long time. Most of the studies have been concentrated on the advance method based on the traditional Kortokoff's method or oscillometric method and its applications rather than focused on a new method development. In general, blood pressure can be checked the blood current pressure in the artery with non-invasive way from the outside of blood vessel. Some Japanese researchers had studied a kind of non-invasive method that can measure the blood pressure from the blood vessel inside [4]. Another research studied on the remote technique to monitor the patient's blood pressure and health status through the wrist-banded type sensor device [5]. Although the existing wrist-type tonometer based on the oscillometric method still oppresses the artery of the wrist by using the air-cuff at every blood pressure measurement trial, the electronics sensor based non-invasive methods measure the blood pressure with the pressure value from the sensor unit [6]. Since non-invasive method could not guarantee the accuracy within the acceptable error range, there are still many oscillometric method based electronics tonometer supported by digital techniques. Many types of research on the u-Healthcare area are interested in the Zigbee, Bluetooth and WiFi wireless communication environment that can connect the electronics healthcare devices to the smartphone, smart pad and smartwatch [7, 8, 9]. But these approaches has been tried to measure the blood pressure directly with the digital sensor. This way eventually has a kind of limitation on the method that has no other considering factors besides the pressure parameter. In this paper, we proposed the blood pressure estimation method with the arterial pulse waveform generated by the blood current in the artery by using digital sensor without oppressing the blood vessel and focused on the evaluation of its effectiveness.

3 Relation between the blood pressure and arterial pulse waveform

The arterial pulse is a kind of impact pulse generated by the heart beat and has closely related to the blood pressure, the pressure of the blood impact to the blood vessel [10]. If we assume there is always the same external pressure parameters such as the atmosphere or the pressure on the skin outside the artery, the amplitude of an arterial pulse waveform would be increased or decreased along with the blood pressure. So, if we find out the relation between the amplitude of the arterial pulse waveform and actual blood pressure, we can easily calculate the real blood pressure by measuring the amplitude of the arterial pulse waveform.

3.1 The differential value

The differential value of an arterial pulse waveform can be defined as the difference between the highest point and lowest point in a single waveform W_i from the continuous arterial pulse waveform W. It can be represented as $\Delta P_{i,}$ the same value as the difference between the S point and P point as shown in Figure 2. In a case of the continuous arterial pulse measuring, there are so many waveforms in the consecutive arterial pulse waveform data. So, we can get the differential values as many as the number of waveforms.

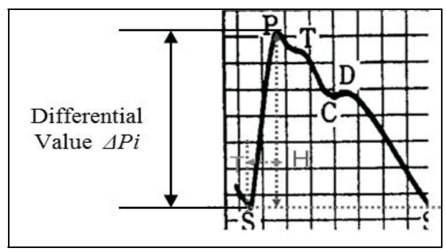

Figure 2 Differential value ΔP_i from waveform W_i

The arterial pulse waveform has various amplitudes and shapes in detail according to the individuals. Therefore, the differential value also has lots of different values also. In this study, we analyzed the relation between the differential value and blood pressure and researched the blood pressure estimation method through the differential value.

3.2 Relation between the blood pressure and arterial pulse waveform

Most of the arterial pulse waveform have almost the same shape for every patient but has a little difference among the detail shapes. The main characteristics of an arterial pulse waveform are the period, linear curve shape and a differential value of each pulse. The period of a waveform corresponds to the pulse count [11], and linear curve shape is concerned with the heartbeat and status of the artery [12]. The differential value of the waveform would be concerned with the blood pressure, but there is no research or report about the exact relation between two factors. In this study, we had investigated various types of volunteer and found out the typical pattern of the arterial pulse waveforms as shown in Figure 3. It shows that there are distinct differences of the differential value among the waveform types. In the clinical case of blood pressure, systolic pressure has more important than diastolic pressure. In general, a hypertensive has higher

ISBN: 1-60132-429-4, CSREA Press ©

systolic pressure than normal person's systolic pressure average, and a hypotension patient has a tendency to lower systolic pressure than normal person's systolic average [13]. Therefore, if we can find out the relation between the differential value and the systolic pressure or diastolic pressure, we can estimate the blood pressure with the differential value from one's arterial pulse waveform.

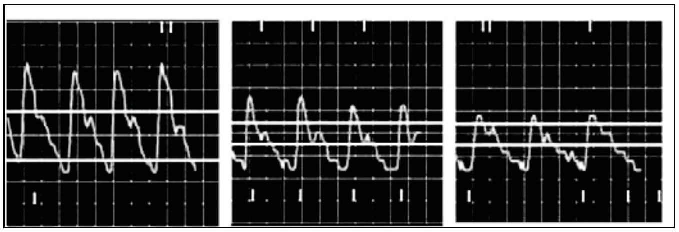

a) Hypertension b) Normal c) Hypotension

Figure 3 3-types of typical arterial pulse waveforms

3.3 Blood pressure relation deduction

To determine the relation between the differential value of the arterial pulse waveform and blood pressure, we have to know what kind of relation between the measured blood pressure from the tonometer and the differential value. To examine the relation, we measured the blood pressures and amplitude of waveforms from many volunteers and deducted the relation equation through regression process. If there is a sort of functional relation between the differential value and the real blood pressure as a result of regression, we can make the BP(Blood Pressure) relation function (1), (2) correspond to the differential value as follows:

$$Systolic\ (\Delta P) = Reg(Systolic_{avg}, \Delta P_{avg}) \quad (1)$$

$$Diastolic\ (\Delta P) = Reg(Diastolic_{avg}, \Delta P_{avg}) \quad (2)$$

ΔP_{avg}: *Average of ΔP_i, $i = 0, .., n$*
(n: number of peaks W_i in W)
$Systolic_{avg}$: Average systolic value of a volunteer
$Diastolic_{avg}$: Average diastolic value of a volunteer

To calculate the P_{avg} and $Systolic_{avg}$, we need lots of clinical data on systolic pressures and arterial pulse waveforms. In this study, we designed and implemented the experimental environment for blood pressure measurement, and gathered systolic pressures and arterial pulse waveforms from 3-kinds of samples: hypertensives, normal persons, and hypotension patients.

4 Experimental environments

4.1 Measurement environment

The arterial pulse waveform measurement system is composed of a digital sensor unit, Bluetooth communication network, and smartphone app. The digital sensor unit has air pressure sensor enclosed in a non-oppress round-type cuff that can detect the pressure variation from outer vessel [14]. The air pressure sensor can output the pressure variation as an integral form of signal that can help measuring the arterial pulse waveform directly. The round-type cuff includes air pressure sensor, Bluetooth communication module that can transmit the digital sensor output values to a specific smartphone, and battery module as shown in Figure 4. The arterial pulse waveform data measured through the digital sensor unit from the wrist vessel is transmitted to the smartphone through the Bluetooth module in the cuff and saved in the smartphone memory while showing the waveform on the screen via the smartphone app.

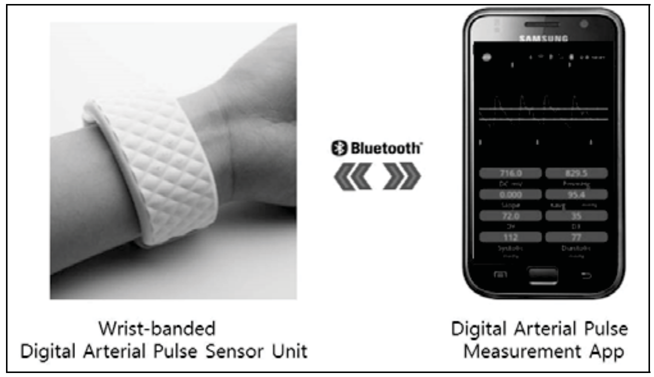

Figure 4 implemented arterial pulse measurement system

Table 1 shows the environment parameters for the arterial pulse waveform measurement system. The digital sensor unit can sample data with the maximum 120Hz sampling rate and 20bits digital data resolution. But the restriction of the maximum data rate of the Bluetooth communication module, actual data resolution of the arterial pulse waveforms has to down as 8bits transmission data that sends to the smartphone. The initial sensor pressure of the sensor oppresses the artery always has to sustain the same pressure during the experiment. If the initial sensor pressure has some variation during measurement, the amplitude of the arterial pulse waveform cannot reflect the corresponding differential value correctly.

Table 1 Environment parameters

System Parameters	Value
Sampling Rate	120Hz
ADC Resolution	20 bit (8bit downsampling)
Sensor Type	Integral Output
Initial Sensor Pressure	852 mmHg
Bluetooth Protocol	2.1+EDR

4.2 Measurement of the differential value

The arterial pulse waveform measurement system converts the waveform data into the differential value ΔP_k

and finally conducts the average of differential value ΔP_{avg} as shown in Figure 5.

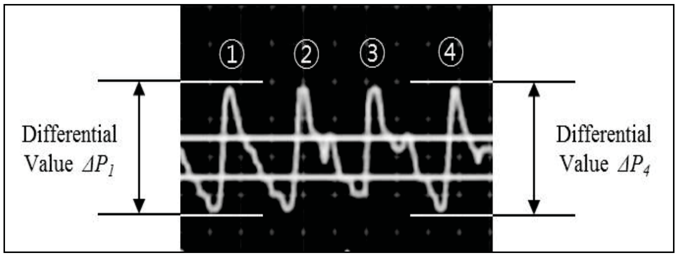

Figure 5 Differential values ΔP_1 and ΔP_4 from arterial pulse waveform ① and ④

ΔP_{avg}, the average of differential values ΔP_k from the arterial pulse waveform of individual volunteer, can be used as input data for building the BP relation equation and can be applied to calculate the systolic pressure.

In this experiment, all volunteers are categorized into three independent groups. All members in Group#1 participated in the experimental data collection to get the BP relation equation. Group#2 and Group#3 participated in the experiments for estimating blood pressure by using BP relation equation. Table 2 shows numbers of volunteers and samples in each group. Group#1 samples were picked from the college students in a class. Group#2 and Group#3 samples were picked from the college men and college women in another class respectively. Each sample was categorized as hypertension that has the systolic pressure over 130mmHg, normal between 105mmHg and 130mmHg, hypotension under 105mmHg.

Table 2 Samples in volunteer groups

	Hypertension	Normal	Hypotension	Total Volunteers
Group #1	11	32	11	54
Group #2	4	12	10	26
Group #3	8	17	4	29

For each volunteer, we attempted 5 times for arterial pulse waveform measurement and 3 times for tonometer alternatively. All measurement tried with 5 minutes interval. In the experiment, we used two brands of tonometer. One is OMRON101 wrist type electronics tonometer, and another is MEDITEC desk type electronics tonometer. For each volunteer, we tried tonometer measurement 3 times, twice with OMRON101 and once with MEDITEC.

The most important thing on every trial is the fact that the sensor has to oppress the skin on the artery with constant initial sensor pressure during the measurement. But it is very difficult to constant the initial sensor pressure all over the measurement process. Therefore, we had to discard all break-away data over 10% of initial sensor pressure on Table 1, and should take 5 effective arterial pulse waveform data within the unavoidable bandage per individual for deducing the BP relation equation. At the same time, for more precise blood pressure estimation, we also deduced another BP relation equation with data those have 5% of initial sensor pressure variation range and performed extra experiments if this equation can enhance the blood pressure estimation precision or not.

5 Experiment results and analyses

5.1 BP relation equation

To get the BP relation equation, we first had to measure the average differential values ΔP_{avg} from each volunteer's arterial pulse waveform data and average systolic pressures $Systolic_{avg}$ with tonometer for all samples in Group#1. Next, we run the regress process by using Microsoft Excel for all $Systolic_{avg}$ and ΔP_{avg} and conducted the first-order regression function as equations (3), (4). Figure 6 shows the regression graphs for systolic pressures vs differential values.

$$Systolic(\Delta P_{avg}) = Systolic\_angle * \Delta P_{avg} + Systolic\_offset \quad (3)$$

$$Diastolic(\Delta P_{avg}) = Diastolic\_angle * \Delta P_{avg} + Diastolic\_offset \quad (4)$$

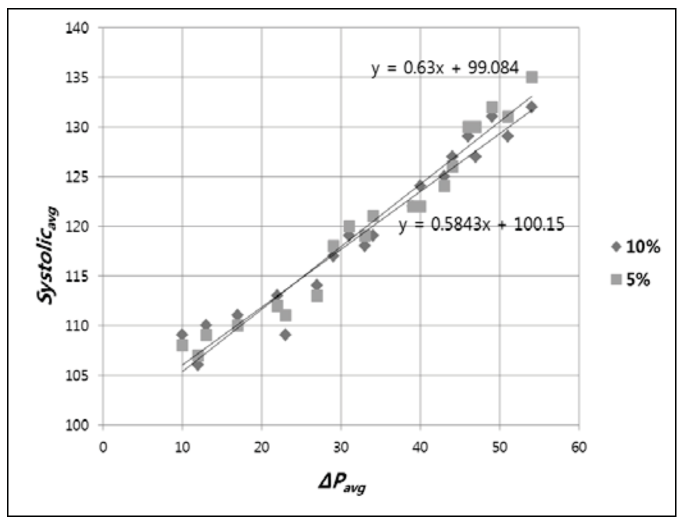

Figure 6 Regression graphs for systolic vs ΔP_{avg} at 10% and 5% initial sensor pressure error range

Table 3 shows the regression results of *Systolic_angle*, *Diastolic_angle*, *Systolic_offset* and *Diastolic_offset*. for all volunteers in Group#1. The *Systolic_angle* and *Systolic_offset* show almost the same value at the case of 10% and 5% of initial sensor pressure breakout bandage within 0.05 of standard deviation. Therefore, we can estimate the systolic pressure by using the BP relation equation with over 95% of accuracy. Otherwise, the standard deviation for diastolic has not affordable values, the estimation results would be unreliable.

Table 3 Results of regression for BP relation function for 10% and 5% initial sensor pressure error range

Factors	Value		St. deviation	
	10%	5%	10%	5%
Systolic_angle	0.5843	0.6300	0.046	0.043
Systolic_offset	100.150	99.084		
Diastolic_angle	0.3617	0.4414	0.264	0.221
Diastolic_offset	71.380	63.224		

5.2 Blood pressure estimation results

To make sure of the reliability and usability of the BP relation equation (3) and (4), we have to validate the precision of the BP relation equation. Therefore, we extracted the differential values ΔP_i from the arterial pulse waveform data for the samples in Group#2, calculated the average differential value ΔP_{avg}, and estimated the systolic pressure and diastolic pressure corresponded to the ΔP_{avg}. Figure 7 and Figure 8 show the analysis results of the differences between the tonometer and blood pressure estimation with ΔP_{avg} for Group#2 and Group#3 by using BP relation equation at 10% initial sensor pressure variation range.

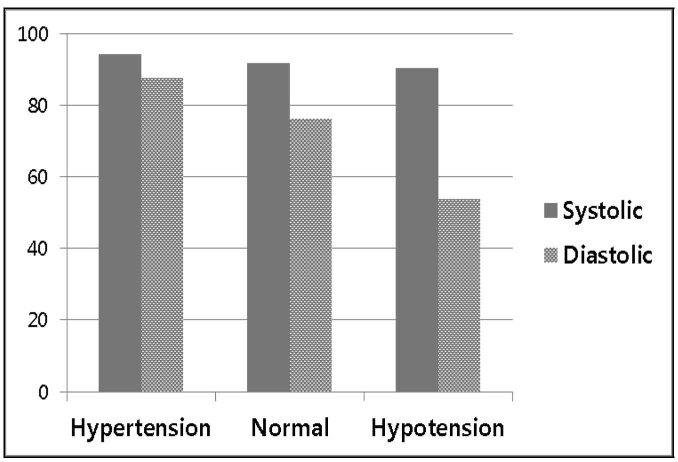

Figure 7 Analysis results for Group #2 with 10% initial sensor pressure variation range

The analysis results show that systolic pressure estimations for Group#2 and Group#3 have less than 10% errors. Otherwise, diastolic pressures have unreliable maximum 66% error rate. It was already expected at the stage of the regress function of the BP relation equation for the diastolic pressure. Though the BP relation equation has high reliability for the systolic pressure, it has also unacceptable standard deviation for the diastolic pressure and expected the high error on experimental estimation.

Figure 8 shows that estimation results for Group#3have lower precision than Group#2. It can explain the fact that the blood pressures of the college women were lower than the college men, and overall blood pressure distribution skews at hypotension. Therefore, Group#3 has remarkable estimated diastolic pressure error than Group#2.

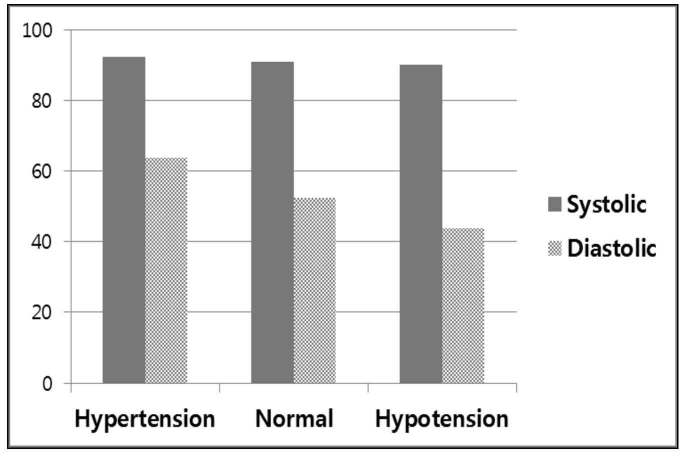

Figure 8 Analysis results for Group #3 with 10% initial sensor pressure variation range

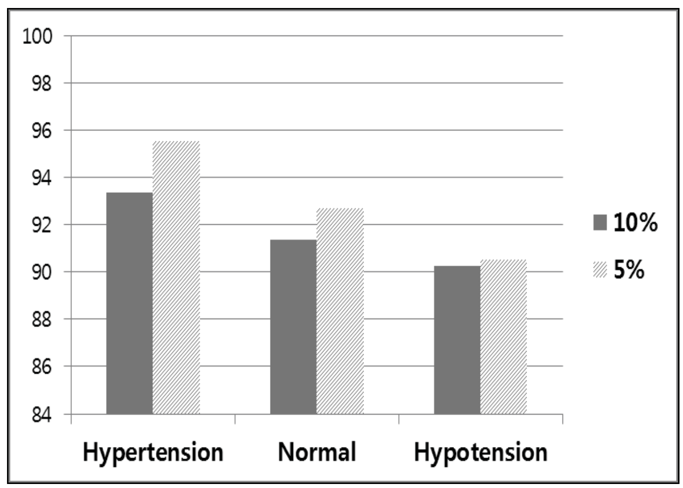

Figure 9 Systolic pressure estimation accuracies at 10% and 5% initial sensor pressure variation range

Figure 9 shows the systolic pressure estimation accuracies for Group#2 and Group#3 at 10% initial sensor pressure variation range and at 5% variation range. Both two cases, though the BP relation equation is almost the same, the accuracies of the estimated systolic pressures are somewhat different, especially for the hypertension case. This result shows that accuracy of the estimated systolic pressure depends on how to sustain constant initial sensor pressure. Therefore, a technique to make the constant initial sensor pressure all over the measurement process is very important to enhance the systolic pressure estimation accuracy.

As the experimental results on systolic pressure estimation, although the blood pressure estimation method with the proposed differential value from the arterial pulse waveform has nice estimation accuracy on the systolic pressure, but has poor performance on diastolic pressure. If there are more volunteers, we also can get more accurate regression function for BP relation equation. But it can enhance the BP relation equation only for systolic pressure estimation, not for the diastolic pressure estimation. Therefore, the proposed blood pressure estimation method can be used effectively to estimate the systolic pressure. Moreover, the initial sensor pressure should be sustained constantly and it is very difficult to contact the sensor on the skin with constant pressure. But if we can reduce the variation of the initial sensor pressure, we can also reduce the error between the estimated systolic pressure and tonometer and enhance the precision of the blood pressure estimation method.

6 Conclusions

This paper proposed a new blood pressure estimation method by using a differential value from one's arterial pulse waveform and BP relation equation. The BP relation equation deduced from the regression function between blood pressure measured by the tonometer and differential value measured with the digital sensor unit. As the experimental results with the BP relation equation, although the diastolic pressure estimation has a little bit poor performance, but the systolic pressure can be estimated with over 90% accuracy.

This work has very high possibility to open a new approach for non-Kortokoff-type continuous blood pressure measurement with the BP relation equation and the digital measurement system. But this method should be more precise to have the low error less than 5% compares to a commercial tonometer for clinical blood pressure measurement method. To make this, we have to get more precise BP relation equation through more experimental trials. Moreover, we need to solve many technical problems in maintaining the initial sensor pressure during the experiment to get more precise differential value through stable arterial pulse waveform measurement. Therefore, we will improve the BP relation equation and enhance the stable, non-Kortokoff-type digital arterial pulse waveform measurement system at further research.

7 Acknowledgement

This work was supported by the National Research Foundation of Korea(NRF) grant funded by the Korea government(MEST)(No. NRF-2015R1D1A1A01057703)

8 References

[1] K. Barbe, W. Van Moer. "An Innovative Oscillometric Blood Pressure Measurement: Getting Rid of the Traditional Envelope"; Proceedings of the 2012 Medical Measurements and Applications (MeMeA), IEEE Conference Publications, 2012.

[2] Bryan. Williams. "Achieving Blood Pressure Control in Clinical Practice"; Journal of the American Society of Hypertension, Vol. 2 No. 4, 10-15, Aug 2008.

[3] Gen Yasuda, Nariaki Ogawa, Gaku Shimura, Daisaku Ando, Kazuhiko Shibata, Satoshi Umemura, Osamu Tochikubo. "Effects of Perindopril on 24-H Blood Pressure in Hypertensive Patients with Diabetic Nephropathy"; American Journal of Hypertension, Vol. 17 No. 5, May 2004.

[4] Osamu Tochikubo, Yoshihiro Kaneko, Youji Yukinari, Ikuo Takeda. "Noninvasive Measurement of Baroreflex Sensitivity Index using an Indirect and Continuous Blood-Pressure Recorder"; Japanese Heart Journal, Vol. 27 No. 6, 849-857, Dec 2008.

[5] Jae Min Kang, Taiwoo Yo and Hee Chan Kim. "A Wrist-Worn Integrated Health Monitoring Instrument with a Tele-Reporting Device for Telemedicine and Telecare"; IEEE Transactions on Instrument and Measurement, Vol. 55, No. 5, 2006.

[6] Myung Cheon. Ahn, Jong Gu Choi, Il Ho Son, Sang Seok Lee and Keun Ho Kim. "Estimated Blood Pressure Algorithm of Wrist Wearable Pulsimeter using by Hall Device"; Journal of the Korean Magnetics Society, Vol. 20 No. 3, 106-113, Jun 2010.

[7] Wookjae Ryu, Euntae Kim, Kyungho An, Sunghoon Woo and Yunseok Chang. "A Bluetooth based 5-HD Measurement System for u-Healthcare"; International Journal of Control and Automation, Vol. 6 No. 1, 141-150, Feb. 2013.

[8] Yong Dae Cha and Gilwon Yoon. "Ubiquitous Health Monitoring System for Multiple Users using a Zigbee and WLAN Dual-Network"; Telemedicine and e-Health, Vol. 15 No. 9, 891-897, Nov 2009.

[9] Yunseok Chang and Boyeon Kim. "A Wireless ECG Measurement System based on Zigbee USN"; The Korea Information Processing Society Transactions: Part C, Vol. 18-C No. 3, 195-198, Mar 2011.

[10] D. Nair, S-Y Tan, H-W Gan, S-F Lim, J. Tan, M. Zhu, H. Gao, N-H Chua, W-L Peh and K-H Mak. "The Use of Ambulatory Tonometric Radial Arterial Wave Capture to Measure Ambulatory Blood Pressure: The Validation of a Novel Wrist-Bound Device in Adults"; Journal of Human Hypertension, Vol. 22 Issue No. 3, 220-222, Mar 2008.

[11] Youngzoon Yoon, Jung Ho Choi, and Gilwon Yoon. "Non-Constrained Blood Pressure Monitoring using ECG and PPG for Personal Healthcare"; Journal of Medical Systems, Vol. 33 Issue No. 4, 261-266, Aug 2009.

[12] Woosik Shin, Young Cha and Gilwon Yoon. "ECG/PPG Integer Signal Processing for a Ubiquitous Health Monitoring System"; Journal of Medical Systems, Vol. 34 Issue No. 5, 891-898, Oct 2010.

[13] Gretchen Ray, James Nawarskas, Joe Anderson. "Blood Pressure Monitoring Technique Impacts Hypertension Treatment"; Journal of General Internal Medicine, Vol. 27 No. 6, 623-629, Jun 2012.

[14] Boyeon Kim, Wenhai Jin, Sung Hoon Woo and Yunseok Chang. "A New Approach on Digital Blood Pressure Measurement Method for u-Healthcare Systems"; International Journal of Bio-Science and Bio-Technology, Vol. 7, No. 1, 169-178, Jan 2015.

Performance and Energy Evaluation of ARM Cortex Variants for Smart Cardiac Pacemaker Application

Safwat Mostafa Noor and Eugene John
Department of Electrical and Computer Engineering,
University of Texas at San Antonio, San Antonio, TX, USA

Abstract - *Embedding microprocessors in implantable devices such as cardiac pacemakers improved their ability to treat complex heart conditions effectively. Future cardiac pacemakers are expected to evolve in features, gaining secure wireless connectivity, longer battery life, and increased operational reliability. Implementing such features in a power constrained pacemaker requires a deep understanding of the power consumption behavior of the underlying processor, especially for computing the expected workloads. In this paper, the popular ARM Cortex series of processors are evaluated against anticipated future workloads of a smart cardiac pacemaker. Simulation results are analyzed to understand the tradeoffs in instruction set design and the importance of a dedicated floating point calculation unit. The simulation results are backed by data collected from the execution of the programs on an actual Cortex-M4 processor with a floating point unit. The instantaneous power consumed by the processor is monitored, and possible improvement techniques are discussed. Execution time and total energy per operation are summarized to conclude the feasibility of existing embedded processors for future cardiac pacemaker application.*

Keywords: ARM, Thumb, Cardiac Pacemaker, Pacemaker Security, STM32

1 Introduction

The use of cardiac pacemakers for the treatment of common heart diseases, such as arrhythmia, increased by 55.6% between the years 1993 to 2009 with approximately 2.9 million patients receiving a permanent pacemaker implant [1]. A pacemaker monitors the cardiac signals of the heart, determines the need for artificial pacing and generates electric impulses to synchronize the heart's rhythm. The technology used in cardiac pacemakers matured over the years in ensuring efficient and reliable operation of its primary functionality. The introduction of microprocessors in cardiac pacemakers in the 1980s [2] made it possible to achieve programmable operating behavior and configurable pacing logic for individual patients; significantly improving the effectiveness of this treatment method. Present day cardiac pacemakers are carefully crafted embedded systems, typically hosting ASIC (Application Specific Integrated Circuit) components, low power processing units, analog filters and charge pump circuitry and a low self-discharge battery [3] as the source of energy. With the help of recent technological advancements, pacemaker manufacturers can equip modern pacemakers with advanced features such as adaptive pacing [2], ultra-low power operation for longer battery life (7-10 years) [3] and wireless telemetry for programming and monitoring [4].

Future cardiac pacemakers are expected to push the boundaries of low-power embedded system design and take advantage of the ubiquitous wireless connectivity present around the patient and in the hospital's infrastructure. Similar to existing wearable devices, future pacemakers can benefit immensely from having the ability to communicate with the patient's smartphone via Bluetooth Low Energy (BLE) or connect to other low power wireless networks. One can imagine a scenario, where a pacemaker can be programmed to transmit alerts automatically via the connected smartphone or low power network when an emergency occurs. This technology can also be used to enable remote diagnosis and treatment. However, the integration of smart computing and connectivity into such a critical application introduces security concerns and power consumption challenges. Secure communication is a serious demand for next generation pacemakers due to vulnerabilities and risks that are currently present [5]. The increase in power consumption from the addition of new features also appears as an obstacle to fulfilling the requirement of a long battery life. A wirelessly connected pacemaker will require higher degrees of security, combined with extreme power efficiency. The energy footprint of both existing and anticipated features must conform to the current power budget of the cardiac pacemaker's battery to ensure a sustainable move forward.

This research attempts to determine the potential workloads in a future cardiac pacemaker and evaluate the performance of these workloads on popular embedded processors, namely the ARM Cortex variants. Utilizing architectural simulation, the computational requirements for each benchmark program are analyzed, and the appropriateness of existing ISAs (Instruction Set Architecture) are studied. The analysis is further authenticated by utilizing an MCU (Micro-Controller Unit) development board to measure the energy consumption of representative programs to evaluate real world performance of the ISA.

2 Pacemaker workloads and Processors

2.1 Heart Signal Processing

The human heart contracts and expands in a specific sequence periodically to distribute blood to the body and lungs.

This movement consists of two steps called the *"diastole"* and *"systole"*. In these two stages, electric impulses are generated and sent to the heart's myocardium muscles via special conduction fibers. These impulses are the cardiac signals that are typically monitored in an ECG (Electrocardiogram). Cardiac signals which are monitored by sensing leads inserted in the heart are called IECG (Intra-cardiac Electrocardiogram). IECG usually contains noise due to muscle activity and physical movement of the lead [2]. This signal is filtered and sampled by dedicated circuitry and then digitally processed to detect the fundamental features of the signals associated with the heart's diastole and systole stages. A complete ECG cycle consists of P, Q, R, S and T components and are visualized in Figure 1.

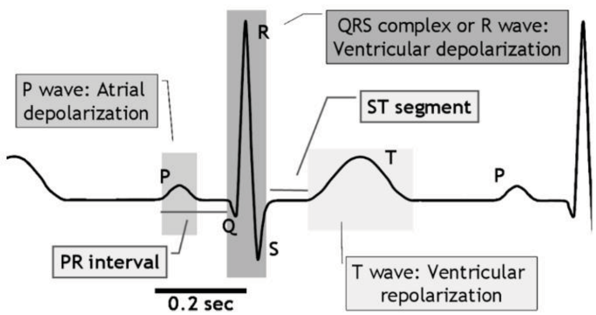

Figure 1: Illustration of a typical electrocardiogram [6]

The nature of an ECG signal has been thoroughly studied and is typically found to have an amplitude in the range of *2mV* peak-to-peak and a bandwidth of *0.05Hz-150Hz* [6]. To accurately determine the existence and occurrence time of a P wave, QRS complex, ST segment and T wave, the time-frequency component of the signal needs to be extracted via a frequency domain analysis. Common signal processing techniques for this purpose include Fourier transform or Short Time Fourier Transform [6]. Detection of an abnormality in the electrocardiogram after extracting the frequency information is trivial compared to the computation involved in the Fourier transform of a large sample size. The Fast Fourier Transform (FFT) is an efficient algorithm for this task and is used as one of the benchmark programs in this paper. The *"FFT"* program is collected from the *MiBench* embedded benchmark suite [7] and a large sample size (8192) is used to examine the performance of the simulated processors. To cover other mathematical operations that might be a part of the detection process, the *"basicmath"* benchmark from *MiBench* is also selected. The *basicmath* program performs a series of common mathematical operation. To simulate the process of generating an artificial pacing signal, the *"ECGSYN"* benchmark program from *ImplantBench* [8] is used in this research. The *ECGSYN* program generates a synthesized ECG signal which can be utilized by the pacemaker's processor to determine the pacing amplitude and duration.

2.2 Security and Reliability

Security is one of the prime concerns in any wireless communication. When wireless functionality is introduced in a cardiac pacemaker, new life-threatening risks emerges. Exploitable vulnerabilities have been demonstrated by researchers [5] in multiple present day wireless cardiac pacemakers which relied on proprietary encryption mechanisms for securing their wireless data transmission. To eliminate such risks, the adoption of industry standard security schemes used in TLS (Transport Layer Security) is desirable. Unfortunately, such computational load requires feasibility study in the power constraint environment of a pacemaker. The *AES* (Advanced Encryption Standard) used by TLS for securing communication data packets is a computationally demanding task and is studied in this research as a benchmark.

To ensure the reliability of transmitted and received data, error checking hash functions are typically used. For a wirelessly connected pacemaker, cryptographic hash functions such as *SHA* (Secure Hash Algorithm) and *CRC* (Cyclic Redundancy Check) can be employed to ensure the reliability of the critical configuration and transmitted data. The list of simulations, therefore, includes benchmark programs for 32 bit *CRC* and *SHA* function as well. The programs representing *AES*, *SHA* and *CRC* are named *"rijndael"*, *"SHA"*, and *"CRC32"* respectively and are all collected from the *MiBench* suite.

2.3 ARM Cortex Processors

ARM Cortex processors are popular choices for embedded systems ranging from high-performance applications to low-power battery operated deeply embedded systems. The Cortex range mainly has three variants, the Cortex-A series, Cortex-R series and Cortex-M series. The major differences between these variants are shown in Table 1.

Table 1. ARM Cortex series comparison [11]

Features	Cortex-A	Cortex-R	Cortex-M
ISA	ARM	ARM	Thumb
Inst. Bits	32	32	16
FPU	Yes	Yes	Optional
DSP Inst.	Yes	Yes	Yes (M4)
Dynamic Power	80µW/MHz	120µW/MHz	8µW/MHz
Application	High Performance	Real Time	Embedded

Cortex-A and Cortex-R processors are intended for high-performance real-time applications such as smartphones and automotive applications. Cortex-M processors cater for low power embedded applications. Despite the similar naming, these variants are largely different at the ISA level. The Cortex-A/R supports the full 32-bit ARM instruction set whereas the Cortex-M only supports a compact 16-bit subset called the "Thumb Instruction Set". The ISA domains can be visualized in Figure 2. The Cortex-M series is less capable but is more efficient in code size and power consumption for simpler workloads typically found in deeply embedded systems. Given the fact that Cortex-M processors can be coupled with an optional floating point unit; it is expected to perform equally well as a Cortex-A for certain applications. To run the simulations, the selected benchmark programs are compiled for

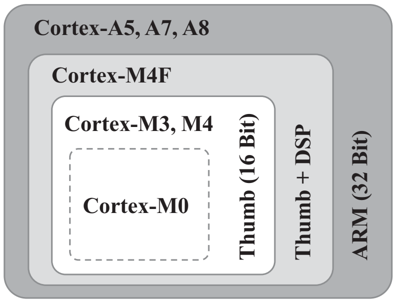

Figure 2: The ARM and Thumb instruction set domains.

three ISA and FPU (Floating Point Unit) configurations: ARM-FPU, THUMB-FPU, and THUMB-NoFPU. Subsequently, an MCU development board bearing a Cortex-M processor coupled with an FPU is used to run some representative programs. The execution time and power consumption footprint on the actual hardware are measured and analyzed.

3 Simulation and Test Methods

The GEM5 architectural simulator [9] was used for simulating ARM and THUMB ISA. The binaries were compiled with *–O3* level optimization and static linking. The standard input files/parameters provided with the benchmarks were used during simulations. The hardware used for measuring power and execution time was an STM32F4-DISCOVERY board shown in Figure 3.

Figure 3: The STM32F4-Discovery Board used for execution time and power measurement.

The onboard MCU (STM32F407VG) was clocked at a relatively slow clock speed of *16MHz*. The clock was generated using the internal RC oscillator to reduce the power consumption. The MCU also includes a low power standby mode which was measured to consume *~2μA* at *3V*. With the built-in RTC (Real Time Clock) enabled this figure goes up to *~3.4μA*. For measuring the current consumption for the benchmark subroutines, the execution sequence shown in Figure 4(a) was followed. The MCU was put in standby mode

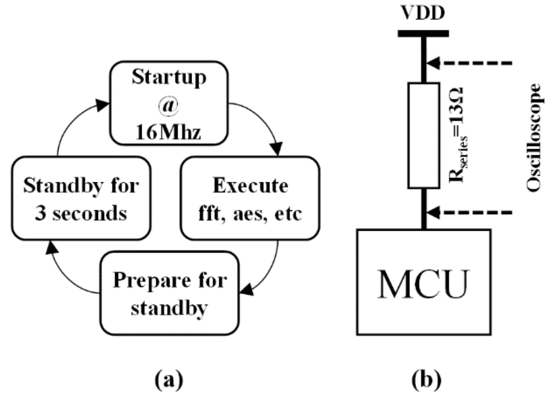

Figure 4: (a) The program sequence for testing (b) The test hardware setup for measuring current

with the RTC running, configured with an RTC wakeup interrupt. The MCU remained in standby mode for a predefined amount of time and consumed *3.4μA* as measured previously. After the standby time passes, the RTC generated interrupt wakes the processor up. The subroutine under test is the first code that is executed after wake up. After the computation is done, the MCU returns to standby mode. This cycle repeats. Since actual processing lasts for a very limited time, it was not possible to use a regular ampere meter to perform the current measurement. To capture the current consumed during this fast transition between active and sleep state, a small valued resistance was connected in series between the VDD and the MCU. The voltage drop across this resistor was measured using an Oscilloscope. The measurement configuration is shown in Figure 4(b). The measured voltage was later converted to current and the total energy consumption was calculated.

4 Experimental Results

4.1 Simulation Results

The GEM5 simulator reports detailed statistics about each simulation. The parameters of interest are execution time, IPC and instruction mix. The statistics of floating point instructions are especially important as it helps to justify the need for a dedicated FPU for a given task. The instruction mix of the programs compiled for three different ISA configurations is shown in Figure 5. In both the ARM-FPU and Thumb-FPU configurations, only three benchmarks (*basicmath, FFT, ecgsyn*) utilized floating point instructions. From this point onwards, these programs will be referred to as floating point benchmarks. The remaining benchmarks (*AES encode, AES decode, SHA,* and *CRC32*) did not perform any floating point calculations and will be referred to as integer benchmarks. For the Thumb-NoFPU configuration, the compiler did not generate any floating point instructions as there was no floating point unit available on the processor. In this configuration all floating point operations were performed through floating point emulation subroutines that rely on the integer calculations, thus resulting in a larger percentage of integer instructions. The most important observation in instruction mix was the similarity of the instruction distribution between ARM-FPU

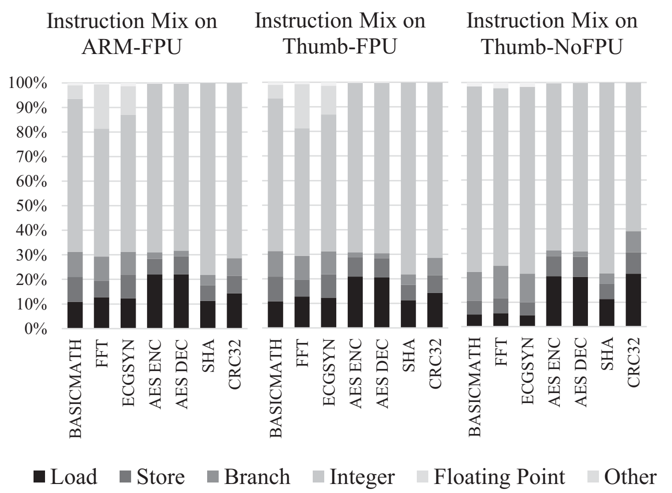

Figure 5: Instruction mix of the benchmark programs compiled for three different ISA platforms.

and Thumb-FPU configurations. This indicates that for the set of workloads at hand, the ARM ISA does not provide any substantial benefit over the Thumb subset in terms of functionality and code size. The program execution performance of the two ISA can still be different given the dissimilarity in their datapath and pipeline configuration.

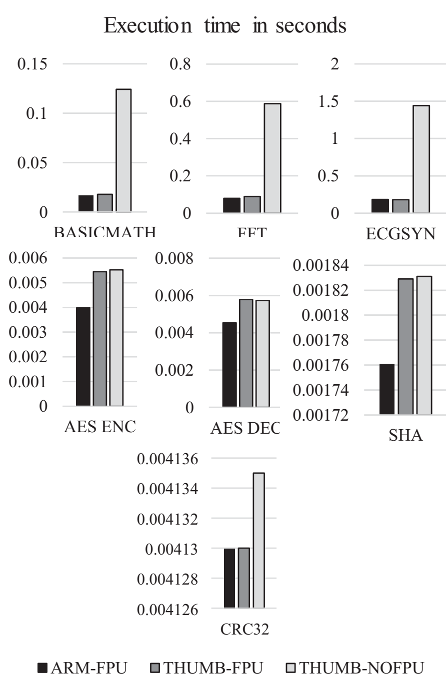

Figure 6: Comparison of execution time of the benchmark programs compiled for three different ISA platforms.

The execution time and IPC for the three configurations can be observed in Figure 6 and Figure 7 respectively. For the floating point benchmarks, the execution time difference for Thumb-NoFPU is substantially greater. This large time requirement is not acceptable for programs such as *FFT*, which is a critical operation that needs to process heart signal samples in real time. In these benchmarks, the Thumb-FPU configuration yields similar execution time as the more capable ARM-FPU configuration. For the remaining integer benchmarks, the ARM ISA exhibits faster execution time than the Thumb sets. However, the time requirement of these programs are smaller, and the difference can be considered as negligible. In the IPC chart of Figure 7, benefits of the ARM

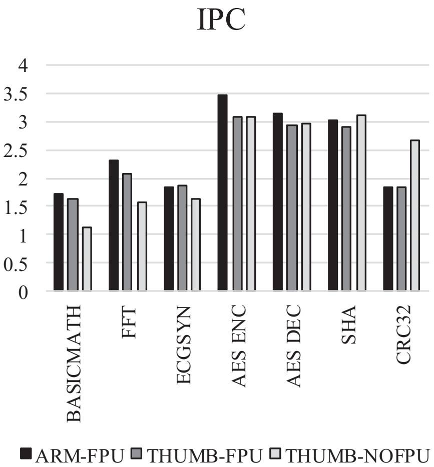

Figure 7: Instruction Per Cycle (IPC) of the benchmark programs compiled for three different ISA platforms

ISA can be observed as it achieves more instruction per cycle (IPC) than other configurations. The average difference with the Thumb-FPU offering and Thumb-NoFPU is *0.14* and *0.16* respectively.

The simulation results clearly indicate that for the set of tasks in future cardiac pacemakers both the ARM-FPU and Thumb-FPU are favorable ISA configurations for performance. Looking at power consumption, the better option is the Thumb or Cortex-M offerings given their low dynamic power consumption of *8µW/MHz* [11]. In contrast, the Cortex-A offers *80µW/MHz* [11]. Modern pacemakers consume *6µW* to *13µW* at *2.8V* [3] depending on their operating state. The power consumption of Cortex-M remains mostly within these limited power budgets.

4.2 Power Consumption Measurements

The benchmarks used in the simulations are designed to evaluate the processor's ability to compute the algorithms of the given task. For practical power consumption estimation, representative programs for *FFT*, *AES encode/decode* [10] and *SHA-256* hash function [10] are used. These programs are optimized for embedded platforms but do not utilize any dedicated hardware on the MCU. Figure 8 shows the voltage measured across the series resistor for the *FFT* operation. The duration of the operation for a 2,048-point input data is about *70ms* with the FPU enabled and *144ms* without the FPU enabled. Figure 9 shows oscilloscope readings for the *AES* (encode and decode) and *SHA* programs. As expected, enabling the FPU did not make any difference in the execution time. The measurements are taken with the FPU disabled to avoid any unwanted power consumption. At the beginning of the *AES* and *SHA* hash functions, the algorithms need to load a large key value stored in the flash memory resulting in the large current

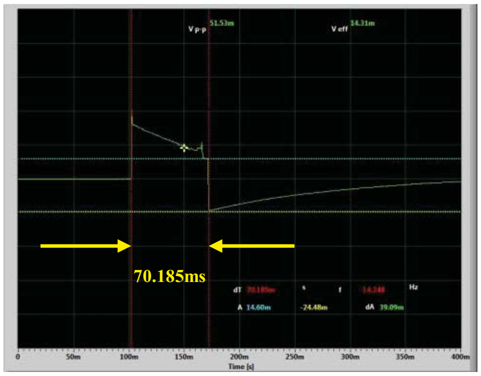

(a)

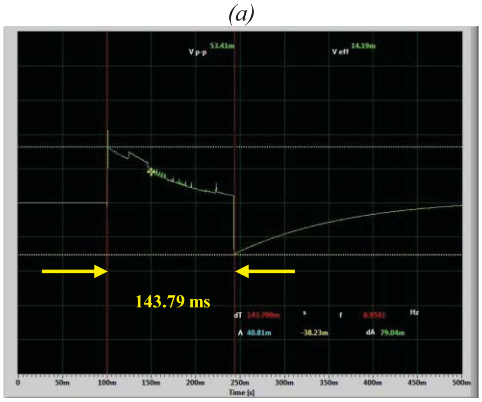

(b)

Figure. 8. Execution time measurement for FFT operation (a) with FPU (b) without FPU.

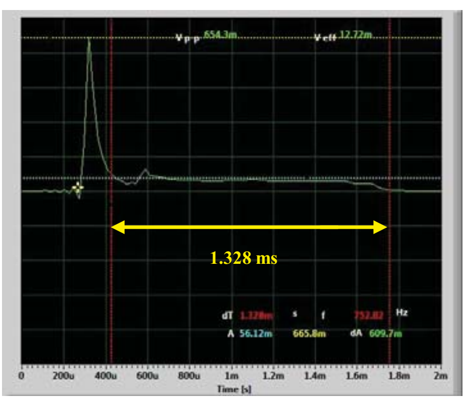

(a)

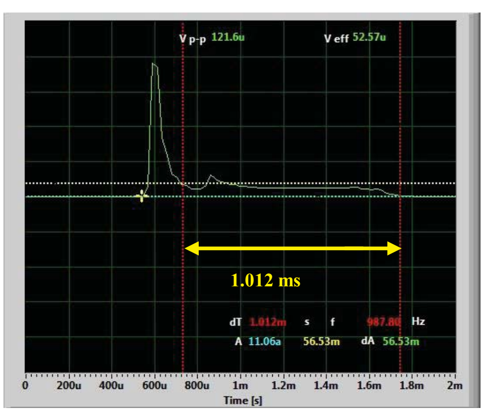

(b)

Figure 9. Execution time measurement for (a) AES operation (encode followed by decode) (b) SHA hash function calculation

spike seen on the oscilloscope. The remaining portion of the consumption envelope is contributed from the actual computation. To avoid the initial surge, the key values can be pre-loaded in the RAM if large enough memory is available. The execution time for *AES* and *SHA* was *1.33ms* and *1.01ms* respectively. The total energy consumed can be calculated by the following equation:

$$E_{total} = \frac{Vdd}{R_{series}} \sum V_s \times t_s [J] \quad (1)$$

Where, E_{total} is the total energy in Joules, V_{dd} is the supply voltage (3V), R_{series} is the series resistor for measurement *13Ohms*, V_s is the amplitude of the sampled voltage and t_s is the oscilloscope sample hold time. Using equation (1), the energy calculated for the three selected programs are listed in Table. II. The results indicate the FFT as the largest power consuming

Table II. Execution time and energy consumption of selected programs.

Program	Time	Energy
FFT_FPU	70.2ms	7.96mJ
FFT_NoFPU	143.8ms	10.8mJ
AES	1.3ms	32µJ
SHA	1.0ms	25.8µJ

program among the other selected tasks. Given this demanding nature of Fourier transform computation, many pacemaker manufacturers rely on ASIC-based approaches for signal processing needs. However, the FFT operation on an ARM based SoC can be further optimized by implementing an integer based algorithm and utilizing DMA (Direct Memory Access) peripherals to transfer data from the source to the RAM. Some additional power consumption was captured in this experiment by reading the input data from the onboard flash memory. Further studies can be conducted by executing critical operations from only RAM with properly determined sample size to reduce the current.

5 Conclusion

The Thumb instruction subset from ARM was designed to be energy efficient in deeply embedded applications. Coupled with a dedicated FPU, this platform can perform efficiently in both floating point and integer workloads. However, for integer based workloads, energy consumption can be further reduced by using more streamlined FPU-less and slowly clocked processing chips. Positive results were observed for encryption and secure hash calculation, which consumed energy in the range of micro joules on the test hardware. On the other hand, Signal processing tasks were more demanding. The execution time and power consumption observed in this paper bring forward the differences in the energy footprint of potential workloads of a future cardiac pacemaker. Given the asynchronous execution nature of the programs and the difference in their energy footprint, the use of heterogeneous architectures such as ARM *"Big.Little"* architecture [12] promises lower power operation. Application specific optimization of each processing core on a heterogeneous architecture can be potentially utilized for low power operation in next generation of cardiac pacemakers.

6 Acknowledgement

Research reported in this paper was supported in part by National Institute of General Medical Sciences of the National Institutes of Health under award number 1SC3GM096937-01A1. The content is solely the responsibility of the authors and does not necessarily represent the official views of the National Institutes of Health

7 References

[1] Greenspon, Arnold J., Jasmine D. Patel, Edmund Lau, Jorge A. Ochoa, Daniel R. Frisch, Reginald T. Ho, Behzad B. Pavri, and Steven M. Kurtz. "Trends in permanent pacemaker implantation in the United States from 1993 to 2009: increasing complexity of patients and procedures." J. of the American College of Cardiology. Vol. 60(16), pp.1540-1545, (2012)

[2] Haddad, Sandro AP, Richard PM Houben, and W. A. Serdijin. "The evolution of pacemakers." IEEE Engineering in Medicine and Biology Magazine, May/June (2006)

[3] Biotronik Effecta Pacemaker Technical Manual, BIOTRONIK SE & Co. KG, Available: http://www.biotronikusa.com/manuals/ (2010)

[4] Lakshmanadoss, U., Shah, A., Daubert, J. P., in "Modern Pacemakers: Present and Future", M. K. Das, Editor, Intech Publisher, Croatia (2011), Chapter 8, pp.129-145.

[5] Halperin, D.; Heydt-Benjamin, T.S.; Ransford, B.; Clark, S.S.; Defend, B.; Morgan, W.; Fu, K.; Kohno, T.; Maisel, W.H., "Pacemakers and Implantable Cardiac Defibrillators: Software Radio Attacks and Zero-Power Defenses". Proceedings of IEEE Symposium on Security and Privacy, (2008) May 18-22; Oakland, California

[6] Haddad, Sandro AP, and Wouter A. Serdijn. "In Ultra Low-Power Biomedical Signal Processing", Springer Netherlands, (2009), Chapter 2, pp.14-26

[7] Guthaus, Matthew R., Jeffrey S. Ringenberg, Dan Ernst, Todd M. Austin, Trevor Mudge, and Richard B. Brown. "MiBench: A free, commercially representative embedded benchmark suite." Proceedings of the IEEE International Workshop on Workload Characterization, (2001) December 2; Austin, Texas

[8] Jin, Zhanpeng, and Allen C. Cheng. "ImplantBench: Characterizing and projecting representative benchmarks for emerging bio-implantable computing." IEEE Micro issue 28, no. 4, pp 71-91, (2008)

[9] Nathan, Binkert, Beckmann Bradford, and Black Gabriel. "The gem5 simulator." ACM SIGARCH Computer Architecture News, vol. 39(2), pp.1-7, (2011)

[10] Texas Instruments, C Implementation of Cryptographic Algorithms, Application Report. Available: http://www.ti.com/lit/an/slaa547a/slaa547a.pdf, (2013)

[11] ARM Cortex Series Documentation, ARM, Available: http://www.arm.com/products/processors/cortex-a/index.php (2015)

[12] Jeff, Brian. "Big. LITTLE system architecture from ARM: saving power through heterogeneous multiprocessing and task context migration." Proceedings of the 49th Annual Design Automation Conference. ACM, 2012.

SESSION

COMPUTATIONAL BIOLOGY: DATA PROCESSING, NOVEL ALGORITHMS AND APPLICATIONS

Chair(s)

TBA

ISBN: 1-60132-429-4, CSREA Press ©

Adaptive Control for a Two-Compartment Respiratory System

Jiann-Shiou Yang
Department of Electrical Engineering, University of Minnesota, Duluth, MN, 55812 USA

Abstract – *This paper provides a preliminary study of using an adaptive inverse dynamics control technique to a two-compartment modeled respiratory system. Based on the nonlinear respiratory model and desired respiratory volumes, the adaptive inverse dynamics control scheme consisting of a control law and an adaptation law is then applied. The control law has the structure of the two-compartment inverse dynamical model but uses estimates of the dynamics parameters in the computation of pressure applied to the lungs. The adaptation law uses the tracking error to compute the parameter estimates for the control law. The preliminary results indicate that the tracking errors can be improved if the parameter values associated with the adaptation law are properly chosen, and the performance is also robust despite relatively large deviations in the initial estimates of the system parameters.*

Keywords: Adaptive inverse dynamics control, respiratory system.

1 Introduction

Respiration is the trading of oxygen and carbon dioxide (CO_2) between the environment and the body cells. In human body, this procedure incorporates spark and termination, dispersion of oxygen from alveoli to the blood and of CO_2 from the blood to the alveoli, and the vehicle of oxygen to and CO_2 from the body cells by method for the circulatory framework. Respiratory failure, that is, the lacking trade of CO_2 and oxygen by the lungs, is a typical clinical issue which needs immediate help with mechanical ventilation while the hidden reason is recognized and treated. For example, a patient with pneumonia may require mechanical ventilation while the pneumonia is being dealt with anti-toxins, which will in the end adequately cure the disease. Since the lungs are vulnerable against discriminating disease and respiratory failure is regular, backing of patients with mechanical ventilation is important in the intensive care unit. The objective of mechanical ventilation is to provide an adequate exchange of oxygen and CO_2 in order for the lungs to function normally. However, without proper control, mechanical ventilation can damage the lungs if the applied ventilation pressure is too high. Therefore, it is desirable to provide the desired blood levels of CO_2 and oxygen with limited pressure to avoid causing the lung injury, either by inflating the lungs to excessive volumes or by applying excessive pressures to inflate the lungs.

A single compartment respiratory lung model characterized by its compliance (i.e., volume/pressure) and the resistance to air flow into the compartment is the most commonly used model [1-3]. In this paper, we use a two-compartment model [4-6] to mirror the way that there are two lungs although a more complicated multi-compartment respiratory model has also been considered by some other researchers [7-10]. The mechanical ventilation via various control techniques such as model predictive control, classical calculus of variations minimization technique, adaptive sliding model control, etc. can be found in the literature (e.g., [8-10]). The inverse dynamics (or computed torque) control is a well known technique for the robot motion control [11-15]. However, to the best knowledge of the author, the adaptive inverse dynamics control technique applying to a lung-rib-cage system has not been reported, even though its effectiveness in the biped locomotion control has been reported [16, 17]. Therefore, it is interesting and worthwhile to investigate whether the adaptive inverse dynamics based methods can still be effectively used to a nonlinear respiratory system despite various other approaches that have been reported in the literature.

2 A Two-Compartment Lung Model

In this section, a two-compartment model is briefly described. The motion of one complete breathing cycle can be divided into two phases: inspiration and expiration. Starting from a parent airway, we assume that each airway unit branches into two airway units of the subsequent generation (i.e., a dichotomy architecture is considered) as shown in Fig. 1. At time $t = 0$, a driving pressure $p_{in}(t)$ is applied to the opening of the parent airway by the respiratory muscles or a mechanical ventilator over the time interval $0 \leq t \leq T_{in}$, with T_{in} the inspiration duration time. At $t = T_{in}$, the applied airway pressure is released and expiration takes place passively during the interval $T_{in} \leq t \leq T_{in}+T_{ex}$, where T_{ex} is the duration of expiration. Let x_i ($i = 1, 2$) be the lung volume in the ith compartment, $c_i^{in}(x_i)$, $i = 1, 2$ ($c_i^{ex}(x_i)$) be the compliance of the compartment i at inspiration (respectively, expiration) which is a nonlinear function of x_i, $R_{j,i}^{in}$, $j = 0, 1$ ($R_{j,i}^{ex}$, $j = 0, 1$) be the resistance to air flow of the ith airway in the jth generation during the inspiration (respectively, expiration) phase with $R_{0,1}^{in}$ ($R_{0,1}^{ex}$) the inspiration of the 0th generation (parent) airway, then the equations for a two-compartmental lung model can be expressed as follows

Inspiration Phase:

$$\mathrm{R}^{in}\,\dot{x}(t) + C^{in}x(t) = p_{in}(t), 0 \le t \le T_{in}; x(0) = x_0^{in} \quad (1)$$

Expiration Phase:

$$\mathrm{R}^{ex}\,\dot{x}(t) + C^{ex}x(t) = p_{ex}(t), T_{in} \le t \le T_{in} + T_{ex}; x(T_{in}) = x_0^{ex} \quad (2)$$

where $x = [x_1, x_2]^T$ (the superscript T means the transpose), and the diagonal compliance matrix C^{in} (C^{ex}) is

$$C^{in} = \begin{pmatrix} \frac{1}{C_1^{in}} & 0 \\ 0 & \frac{1}{C_2^{in}} \end{pmatrix}, C^{ex} = \begin{pmatrix} \frac{1}{C_1^{ex}} & 0 \\ 0 & \frac{1}{C_2^{ex}} \end{pmatrix}$$

and

$$R^{in} = \begin{pmatrix} R_{0,1}^{in} + R_{1,1}^{in} & R_{0,1}^{in} \\ R_{0,1}^{in} & R_{0,1}^{in} + R_{1,2}^{in} \end{pmatrix}, R^{ex} = \begin{pmatrix} R_{0,1}^{ex} + R_{1,1}^{ex} & R_{0,1}^{ex} \\ R_{0,1}^{ex} & R_{0,1}^{ex} + R_{1,2}^{ex} \end{pmatrix}$$

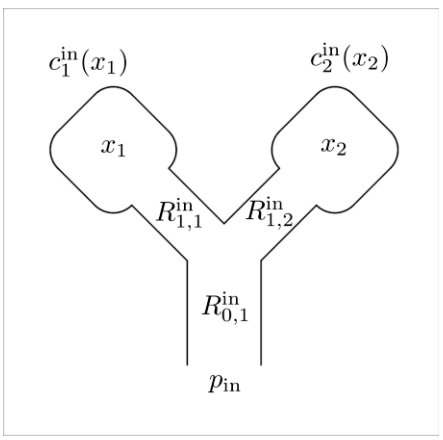

Fig. 1. Two-compartment lung model.

In order for the system to achieve ideal performance, a set of volume and airflow pattern (i.e., trajectories) corresponding to the inspiration and expiration for both the phases will be used as our reference trajectories.

3 Adaptive Inverse Dynamics Control

Since linearized system equations cannot always be trusted to accurately predict the responses of real (nonlinear) systems, we directly consider nonlinear control and briefly review the adaptive control scheme [11-15] to be used in our respiratory system. Consider a nonlinear dynamical robotic system described as

$$D(q)\ddot{q} + C(q,\dot{q})\dot{q} + g(q) = \tau \quad (3)$$

where q is the n×1 vector of robot joint coordinates, τ is the n×1 vector of applied joint torques (or forces). $D(q)$ is the n×n symmetric positive definite inertia matrix, $C(q,\ddot{q})\dot{q}$ is the n×1 vector of centrifugal and Coriolis torques, and $g(q)$ is the n×1 vector of gravitational torques. It is well known that by the property of linearity in the parameters [12-14] the dynamical equation can be written as

$$D(q)\ddot{q} + C(q,\dot{q})\dot{q} + g(q) = Y(q,\dot{q},\ddot{q})p \quad (4)$$

where $Y(q,\dot{q},\ddot{q})$ is an n×m matrix of known functions, known as the regressor, and $p = [p_1, p_2, \cdots, p_m]^T$ is an m-dimensional vector of parameters.

Inspecting (3) we see that if the (nonlinear) control τ is chosen as

$$\tau = D(q)a + C(q,\dot{q})\dot{q} + g(q) \quad (5)$$

then, by substituting (5) into (3) and using the property of $D(q)$ one obtains

$$\ddot{q} = a \quad (6)$$

The vector term a can be defined in terms of a given linear compensator K as

$$a = \ddot{q}^d - Ke \quad (7)$$

with the tracking error $e = q - q^d$, where $q^d(t)$ is an n-dimensional vector of desired joint trajectories. Substituting (7) into (6) leads to the linear error equation in the s-domain as

$$[s^2 I_n + K(s)]e(s) = 0 \quad (8)$$

where I_n is an n x n identity matrix. Letting $K(s) = K_v s + K_p$ leads to the familiar second-order error equation (in the time-domain)

$$\ddot{e} + K_v\dot{e} + K_p e = 0 \quad (9)$$

If the gain matrices K_v and K_p are chosen as diagonal matrices with positive diagonal elements then the closed-loop system is linear, decoupled, and exponentially stable.

The above approach is based on exact cancellation of all nonlinearities in the system. However, in any physical system there is a degree of uncertainty regarding the values of various parameters. There will always be inexact cancellation of the nonlinearities in the system due to this uncertainty and also due to computational round-off, etc. In addition, the burden of computing the complete model may be prohibitively expensive or impossible within the bounds imposed by the available computer architecture. In such cases, it is desirable to simplify the equations of motion as much as possible by ignoring certain of the terms in the equations in order to speed the computation of the control law. Therefore, it is much more reasonable to suppose that, instead of (5), the nonlinear control law is actually of the form

$$\begin{aligned} \tau &= \hat{D}(q)a + \hat{C}(q,\dot{q})\dot{q} + \hat{g}(q) \\ a &= \ddot{q}^d - K_v\dot{e} - K_p e \end{aligned} \tag{10}$$

where $\hat{D}$, $\hat{C}$, and $\hat{g}$ are the estimates of D, C, and g, respectively.Assume that $\hat{D}$, $\hat{C}$, and $\hat{g}$ have the same functional form as D, C, and g with estimated parameters $\hat{p}_1, \hat{p}_2, \ldots, \hat{p}_m$, then

$$\hat{D}(q)\ddot{q} + \hat{C}(q,\dot{q})\dot{q} + \hat{g}(q) = Y(q,\dot{q},\ddot{q})\hat{p} \tag{11}$$

where $\hat{p} = [\hat{p}_1, \hat{p}_2, \ldots, \hat{p}_m]^T$ is the vector of the estimated parameters. Substituting (10) into (1) gives

$$D\ddot{q} + C\dot{q} + g = \hat{D}(\ddot{q}^d - K_v\dot{e} - K_p e) + \hat{C}\dot{q} + \hat{g} \tag{12}$$

Adding and subtracting $\hat{D}\ddot{q}$ on the left-hand side of (12) and using (11), we obtain

$$\hat{D}(\ddot{e} + K_v\dot{e} + K_p e) = \tilde{D}\ddot{q} + \tilde{C}\dot{q} + \tilde{g} = Y(q,\dot{q},\ddot{q})\tilde{p} \tag{13}$$

where $(\tilde{\cdot}) := (\hat{\cdot}) - (\cdot)$. Finally, the error dynamics can be written as

$$\ddot{e} + K_v\dot{e} + K_p e = \hat{D}^{-1}Y\tilde{p} = \Phi\tilde{p} \tag{14}$$

The system (14) can further be expressed in the state-space form as

$$\dot{x} = Ax + B\Phi\tilde{p} \tag{15}$$

where

$$A = \begin{pmatrix} 0 & I_n \\ -K_p & -K_v \end{pmatrix}, B = \begin{pmatrix} 0 \\ I_n \end{pmatrix}, x = \begin{pmatrix} e \\ \dot{e} \end{pmatrix} \tag{16}$$

Based on (15) and (16), we choose the update law

$$\dot{\tilde{p}} = -\Gamma^{-1}\Phi^T B^T P x \tag{17}$$

where $\Gamma = \Gamma^T > 0$ and P is the unique, symmetric, positive definite solution to the Lyapunov equation

$$A^T P + PA = -Q \tag{18}$$

for a given symmetric, positive definite Q. Since the parameter vector p is constant, we have $\dot{\tilde{p}} = \dot{\hat{p}}$. Assume that $\ddot{q}$ is measurable and $\hat{D}^{-1}$ is bounded, then the solution of (15) satisfies $x \to 0$ as $t \to \infty$ with all signals remaining bounded (for proof, see [12]).

There are several different versions of the above technique. For example, the boundedness of the estimated inertia $\hat{D}^{-1}$ is removed in [14], while in [18] the requirement on measurement of $\ddot{q}$ is removed but still needs the boundedness of $\hat{D}^{-1}$. Several papers have been devoted to the implementation of the above adaptive inverse dynamics method without measuring $\ddot{q}$. For example, estimate $\ddot{q}$ from $\dot{q}$ via a first-order filter. In practice, this approach should be expected to work well.

4 Preliminary Results

Based on the desired volume pressures and the two-compartment model equation, the adaptive inversed dynamics control scheme is used to control the pressure parameters. The values of the inspiratory and expiratory lung resistance constants and compliances for the two-compartment lung model were taken from [9] and they are: $R_{0,1}^{in}$ = 9 cm H_2O/*l*/*s*, $R_{1,1}^{in}$ = $R_{1,2}^{in}$ = 16 cm H_2O/*l*/*s*, $R_{0,1}^{ex}$ = 18 cm H_2O/*l*/*s*, $R_{1,1}^{ex}$ = $R_{1,2}^{ex}$ = 32 cm H_2O/*l*/*s*. The expiratory resistance is assumed two times higher than the inspiratory resistance. The lung compliance is chosen to be 0.1 *l*/cm H_2O. The inspiration duration time T_{in} = 2 s and the expiration time T_{ex} = 3 s. The desired air pressures were taken from [8, 9]. During the adaptive inverse dynamics control process, the total number of parameters to be estimated is six and Fig. 1 shows the three estimated parameters p_2, p_4 and p_6 over time during one breathing cycle. Figure 2 shows the tracking errors; for instance, e_2 is the difference between the desired and actual pressures entering the 2nd compartment. Overall, the tracking errors are reasonable small.

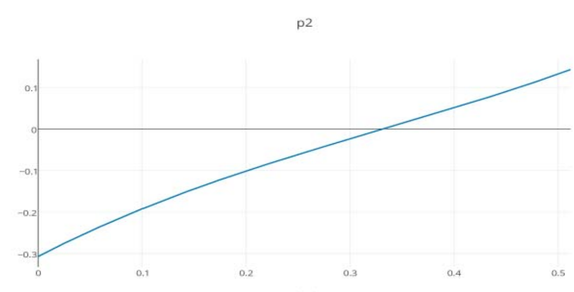

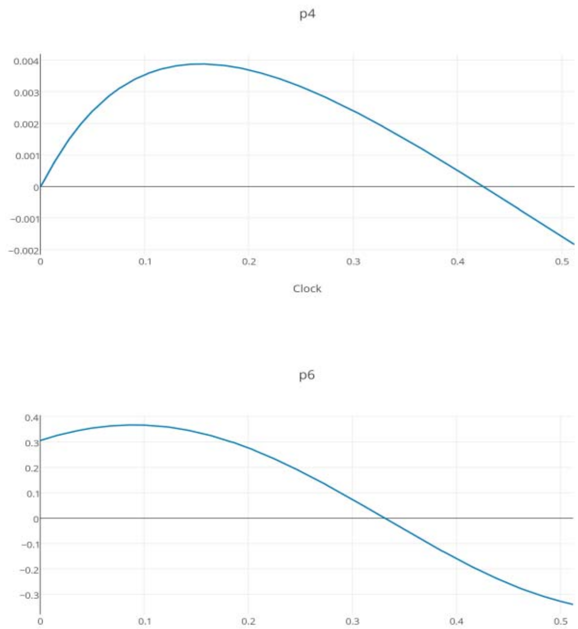

Fig. 2. Parameter estimates during one breathing cycle.

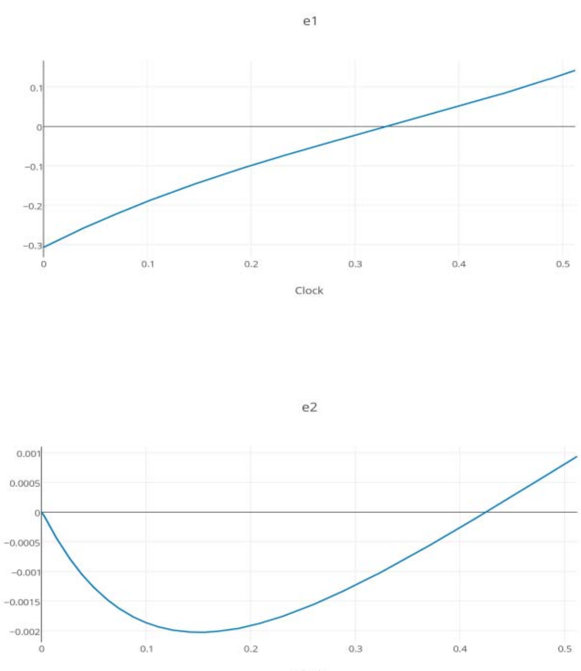

Fig. 3. Tracking errors.

5 Conclusions

We have applied the adaptive inverse dynamics control method to a two-compartment respiratory system. The implementation of the control scheme consists of a control law and an adaptation law. The control law has the structure of the two–compartment inverse dynamics servo but uses estimates of the dynamics parameters in the computation of pressure applied to the lungs. The adaptation law uses the tracking error to compute the parameter estimates for the control law, stops updating a given parameter when it reaches its known bounds, and resumes updating as soon as the corresponding derivative changes sign. The advantage of using the inverse dynamics control method is that it formulates a globally convergent adaptive controller which does not require approximations such as local linearization, time-invariant, or decoupled dynamics to guarantee the tracking convergence. Simulations show that the tracking errors are acceptably small. The future work includes the robustness study of the control method to the multi-compartment model.

Acknowledgements

The author would like to thank Sujnana Korrapati for helping with computer simulations.

6 References

[1] Campbell, D. and Brown, J. (1963). The Electrical Analog of the Lung. *British Journal of Anesthesia*, vol. 35, pp. 684–693.

[2] Wald, A., Murphy, T., and Mazzia, V. (1968). A Theoretical Study of Controlled Ventilation. *IEEE Trans. Biomedical Engineering*, vol. 15, no. 4, pp. 237-248.

[3] Laubscher, T., Heinrichs, W., Weiler, N., Hartmann, G., and Brunner, J. (1994). An Adaptive Lung Ventilation Controller. *IEEE Trans. Biomedical Engineering*, vol. 41, no. 1, pp. 51-59.

[4] Crooke, P., Head, J., and J. Marini, J. (1996). A General Two-Compartmental Model for Mechanical Ventilation. *Mathematical and Computer Modeling*, vol. 24, no. 7, pp. 1-18.

[5] Hotchkiss, J., Crooke, P., Adams, A., and Marini, J. (1994). Implications of a Biphasic Two-compartment Model of Constant Flow Ventilation for the Clinical Setting. *Journal of Critical Care*, vol. 9, no. 2, pp. 114–123.

[6] Similowski, T. and Bates, J. (1991). Two-Compartment Modeling of Respiratory System Mechanics at Low Frequencies, Gas Redistribution or Tissue Rheology. *European Respiratory Journal*, vol. 4, no. 3, pp. 353-358.

[7] Crooke, P., J. Marini, J., and J. Hotchkiss, J. (2002). Modeling Recruitment Maneuvers with a Variable Compliance Model for Pressure Controlled Ventilation," *Journal of Theoretical Medicine*, vol. 4, no. 3, pp. 197-207.

[8] Li, H. and Haddad, W. (2011). Optimal Determination of Respiratory Airflow Patterns Using a Nonlinear Multi-Compartment Model for a Lung-Rib-Cage System.

Proceedings of the 2011 American Control Conference, San Francisco, CA, pp. 3524-3529.

[9] Li, H. and Haddad, W. (2013). Model Predictive Control for a Multi-compartment Respiratory System. *IEEE Tran. Control Systems Technology*, vol. 21, no. 5, pp. 1988-1995.

[10] Chellaboina, V., Haddad, W., Li, H., and Bailey, J. (2010). Limit Cycle Stability Analysis and Adaptive Control of a Multi-Compartment Model for a Pressure-Limited Respirator and Lung Mechanics System. *Internal Journal of Control,* vol. 83, no. 5, pp. 940-955.

[11] Craig, J. J., Hsu, P., and Sastry, S. (1986). Adaptive Control of Mechanical Manipulator. *Proc. IEEE Int'l Con on Robotics and Automation*, pp. 190-195, San Francisco, CA.

[12] Craig, J. J. (1988). *Adaptive Control of Mechanical Manipulators*, Addison-Wesley, Reading, MA.

[13] Spong, M. and Vidyasagar, M. (1989). *Robot Dynamics and Control*, John Wiley & Sons, New York, NY.

[14] Spong, M. and Ortega, R. (1990). On Adaptive Inverse Dynamics Control of Rigid Robots. *IEEE Trans. Automatic Control*, vol. 35, pp. 92-95.

[15] Ortega, R. and Spong, M. (1990). Adaptive Motion Control of Rigid Robots: a Tutorial. *Automatica*, vol. 25, pp. 92-95.

[16] Yang, J.-S. (1994). A Control Study of a Kneeless Biped Locomotion System. *Journal of the Franklin Institute*, vol. 331B, no. 2, pp. 125-143.

[17] Yang, J.-S. (1997). Control of a Five-Link Biped Using an Adaptive Inverse Dynamics Method. *Control and Computers*, vol. 25, no. 2, pp. 56-64.

[18] Middleton, R. and Goodwin, G. C. (1988). Adaptive Computed Torque Control for Rigid Link Manipulator. *Systems and Control Letter*, vol. 10, pp. 9-16.

Towards human brain signal preprocessing and artifact rejection methods

Raja Majid Mehmood[1] and Hyo Jong Lee[1, 2, *]

[1] Division of Computer Science and Engineering
[2] Center for Advanced Image and Information Technology
[*]Corresponding author
Chonbuk National University, Jeonju, SOUTH KOREA
rmeex07@gmail.com, hlee@chonbuk.ac.kr

Abstract – *In the brain computer interface (BCI) research field, a neurological occurrence is the only source of control in any BCI system. Artifacts are contrary signals that can affect with neurological phenomena. These artifacts may lead to the source of control in BCI systems. Electromyography (EMG) and electrooculography (EOG) artifacts are physiological artifacts that are carefully processed in BCI systems. This paper describes the common EOG, EMG, and non-physiological artifacts associated with our experiment and the procedure for artifact rejection. During artifact rejection, we considered the presence of EMG and EOG artifacts in the brain signals. Results had shown the stability in brain signals after applying the artifact rejection such as, eye blink, eye movement, muscle movement, and bad channels.*

Keywords: *Artifact Rejection, EEG, Emotion Recognition, Brain Computer Interface*

1 Introduction

A brain computer interface (BCI) system works in combination of the user's brain and computing device or system. A successful BCI system enables a human to control some aspects of their environment, for example; controlling computer system, computer aided education system, etc. [1-9]. There are some artifacts and noises occurring during the communication of BCI system. These artifacts are undesired signals which lead to wrong interpretations and affect the neurophysiological results. Artifacts are recognized as either non-physiological or physiological sources. Non-physiological sources include high power line noise, changes in electrode impedances, etc. and physiological sources include eye or muscle movements, etc. Even though BCI researchers consider essential safety measures to control non-physiological artifacts, physiological artifacts, particularly artifacts generated by eye or body movements. These artifacts may cause a significant problem in the design of BCI systems [10-12].

Artifacts are adverse potentials that corrupt brain signals, and are mostly of non-cerebral location of the brain. Unfortunately, these artifacts may change the meaning of a neurological phenomenon used to drive a BCI system in real time. Therefore, even cerebral potentials may sometimes be considered as artifacts. For example, in movement related potentials (MRP) [13] based BCI system, a visual evoked potential (VEP) is considered as an artifact. McFarland et al. presented the visual alpha rhythms appeared as artifacts in a Mu-based BCI systems [14]. A common issue with such artifacts is that they could mistakenly result in controlling the device or system [15]. Therefore, there is a need to avoid, reject or remove artifacts from recordings of brain signals, initially [16-22].

Artifacts can be originated from both non-physiological and physiological sources. Non-physiological artifacts produce from external sources of the human body, for example 50 or 60 Hz power line noise or changes in EEG channels impedances, lack of proper filtering, shielding, etc. Previous researches mentioned about non-physiological artifacts and the methods of avoiding, rejecting or removing them [23]. Physiological artifacts arise from a various human body related activities. For example, electrocardiography (ECG) artifacts are caused by heart beats which may produce a rhythmic activity into the EEG signal. Respiration can also cause artifacts by producing a rhythmic activity that is coordinated with the human respiratory movements. Skin responses such as sweating may alter the impedance of electrodes and cause artifacts in the EEG signals [24]. The common physiological artifacts that have been most examined in BCI studies, however, are ocular (EOG) and muscle (EMG) artifacts [18, 23, 25, 26].

In this paper, we describe the common electrooculography (EOG), electromyography (EMG), and other non-physiological artifacts. Artifacts produced by eye blinks or movements (EOG) or muscle movements (EMG) are reviewed in the context of our experiment settings. The aim of the current study is to examine the outcomes after the rejection of aforementioned artifacts from brain signals. Our experiment was based on four emotions in arousal valence domain. Emotions were induced in subjects by presentation of different emotional stimuli. Further, we explained the methodology of this paper in Section 2. Section 3 contained the results and discussion of our experiment. Finally, we presented the conclusion of this paper in Section 4.

2 Material and Methods

The purpose of this experiment is to induce the emotional response in human subject during the visual presentation. We adopted the international affective picture system (IAPS) in this research. IAPS is a two dimensional picture database in arousal and valence domain [27, 28]. We selected four emotional states in our experimental study, such as, happy, scared, calm and sad. We selected 180 stimuli (45 stimulus x 4 emotional-states) from equally distributed groups along the arousal-valence axes from IAPS database. The EEG signals were recorded through Emotiv-EPOC headset. It included 14 EEG channels with 2 reference channels. These channels were placed according to the international 10/20 electrode placement. The sampling rate of this device is 128 samples per seconds [29]. A detail description of our experiment settings is explained through Fig. 1. Where, we can see the starting point of our experiment is stimulus-presentation-computer and it completes after artifact rejection process. The resultant EEG signals show the clean signal patterns at the end of the following process flow. Artifact rejection includes the eye blink, eye movement, muscle movement, and bad channels.

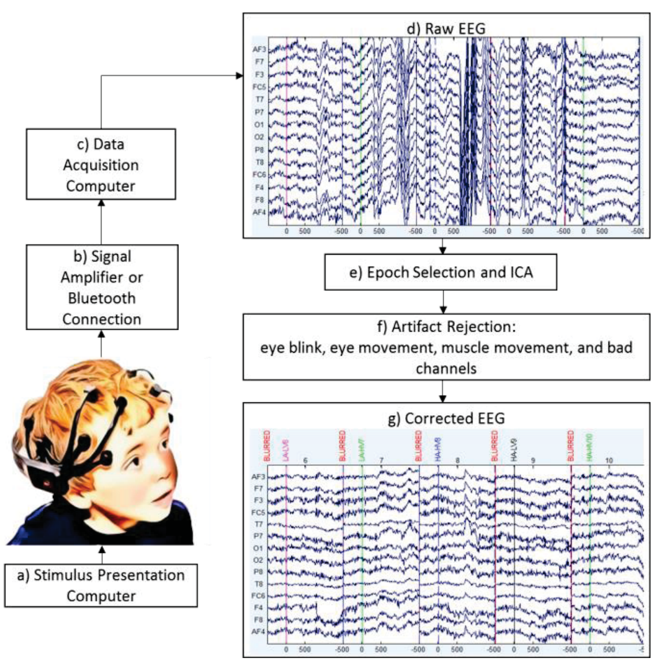

Fig. 1. EEG experiment with recording procedure and preprocessing steps.

We recorded the EEG signal data of every subject, separately through Emotiv device. The emotional picture was presented randomly for 1500ms following another 500ms with a blank image. This procedure continued for the whole session. The blank image was useful to release the emotional activity of a subject which was elicited due to the previous picture. We presented a cross window for four seconds at start and end each training session. The duration of this training session is about 368 seconds for every subject. The recorded EEG brain signal was processed in the EEGLAB toolbox which belongs to SCCN Lab [10]. This toolbox is running on the Matlab platform. EEG signals were preprocessed through band pass filtering with low and high pass filters which are 0 and 50 Hz, respectively. Further, we processed the brain recorded EEG data into independent component analysis (ICA). We also performed a manual rejection of artifacts such as, eye blinks, eye movement, muscle movement, and bad channel, etc. We used 14 electrodes for recoding our experiment such as, AF3, F7, F3, FC5, T7, P7, O1, O2, P8, T8, FC6, F4, F8, and AF4 as displayed in Fig. 2.

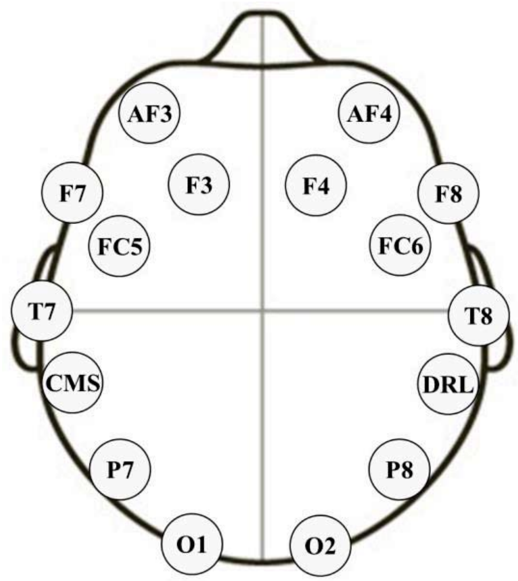

Fig. 2. Emotiv-EPOC headset 14 channel placement with two reference channels

3 Result and Discussion

A total 21 long-term EEG recordings were recorded and later used in this study. The data were collected from 14 scalp electrodes placed according to the international 10-20 System with additional electrodes CMS and DRL besides the ear side. The sampling frequency was 128 Hz. The EEG recordings contain emotion related activity from normal subject. Fig. 1 shows a few seconds EEG epochs of one of the recordings used in this study. This EEG epoch contains the activity of the emotional stimulus onset. The initial raw EEG (Fig. 1 (d)) is contaminated with EOG and muscle artifacts. Fig. 1 (g) shows the same EEG recording after EOG artifact correction by the proposed procedure in this study. Fig. 3 shows the sample subject information EEGLAB toolbox. It shows the number of EEG channels, epochs, sampling rate, etc. ICA analysis was performed during the preprocessing phase of recorded EEG data on each subject, separately. A sample ICA components of single subject are displayed in Fig. 4. During the artifact rejection, we found various artifacts in different subjects. Here, we will show all possible examples of artifacts rejections in EEG data of all subjects. In the following, we will try to demonstrate the common examples of artifact rejection from our EEG data. Fig. 5 shows the example of eye blinks in ICA component number 2 (IC2). Where we can see the high amplitude at the frontal side of IC2 scalp map. Similarly, Fig. 6 shows the eye movements and it can be observed by looking at frontal left and right side of IC5 scalp map. IC7 in Fig. 7 shows the muscle movements that can be observed and analyzed from ERP amplitude in the ERP-image. Bad channel was appeared in Fig. 8, where FC6 channel is located at the frontal-central of the human brain, which shows the high noise or amplitude of EEG signals. Finally, Fig. 9 shows the pulse artifact in activity power spectrum graph, where we can easily see two peaks between 5 and 10 Hz. A detailed analysis of the corrected recordings showed that virtually all blinking artifacts. Results shown that the artifacts (such as, eye blinks, eye movements, muscle movements, bad channels, and pulse artifacts) were removed through above mentioned procedure of artifact rejection.

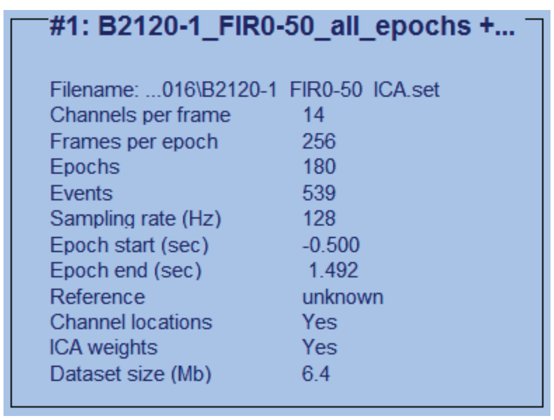

#1: B2120-1_FIR0-50_all_epochs +...

Filename: ...016\B2120-1 FIR0-50 ICA.set	
Channels per frame	14
Frames per epoch	256
Epochs	180
Events	539
Sampling rate (Hz)	128
Epoch start (sec)	-0.500
Epoch end (sec)	1.492
Reference	unknown
Channel locations	Yes
ICA weights	Yes
Dataset size (Mb)	6.4

Fig. 3. Subject information in EEGLAB toolbox

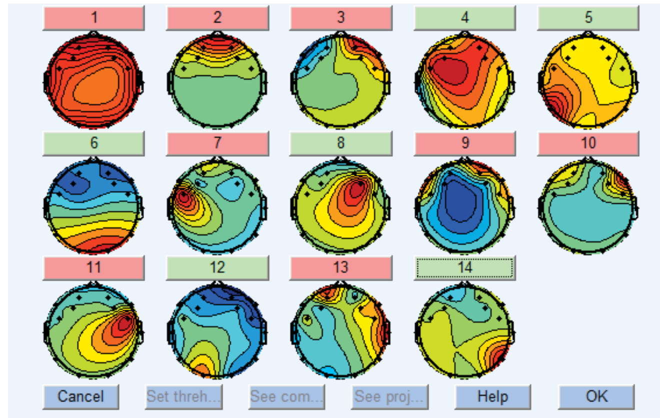

Fig. 4. ICA components of single subject after epoch selection

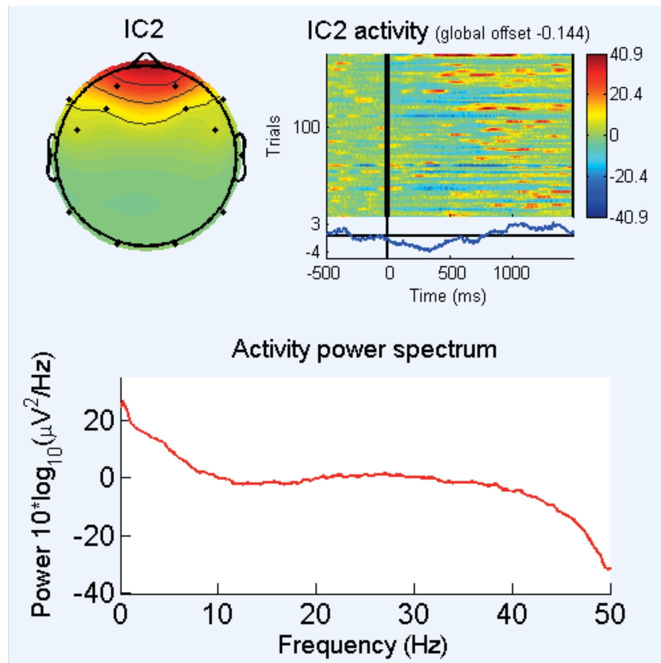

Fig. 5. Eye blinking, IC2 shows the high amplitude at anterior frontal side in component map

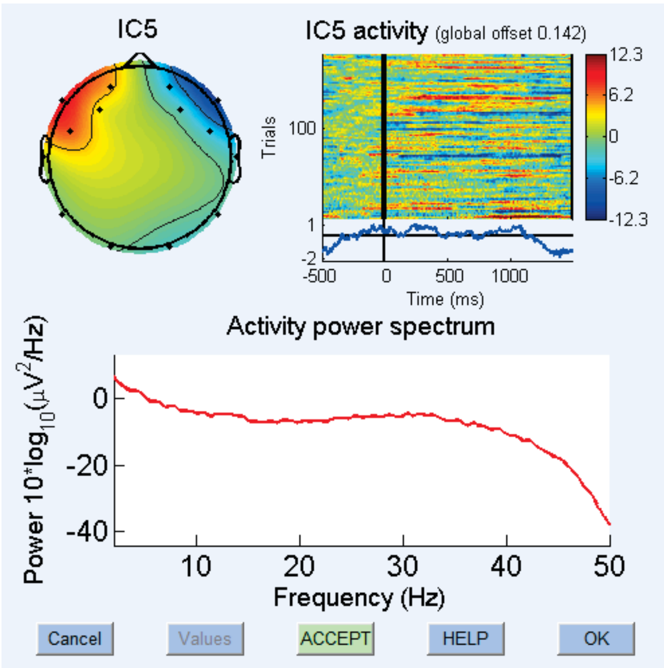

Fig. 6. Eye movements, IC5 shows the activity at left-right frontal side in component map

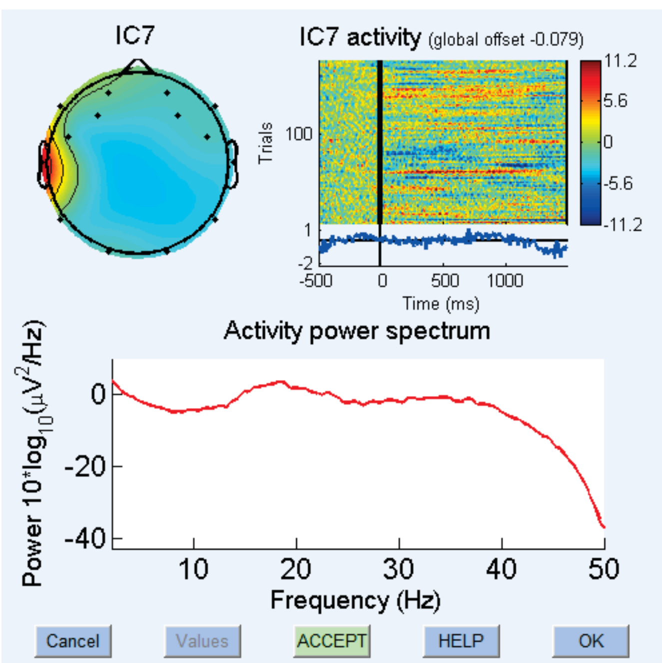

Fig. 7. Muscle movements, appeared in ERP image

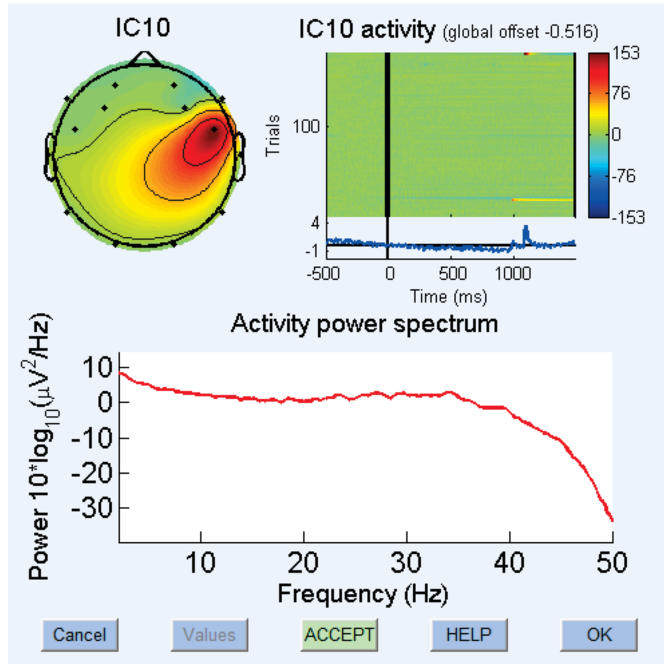

Fig. 8. Bad channels, IC10 shows the abnormal activity at FC6

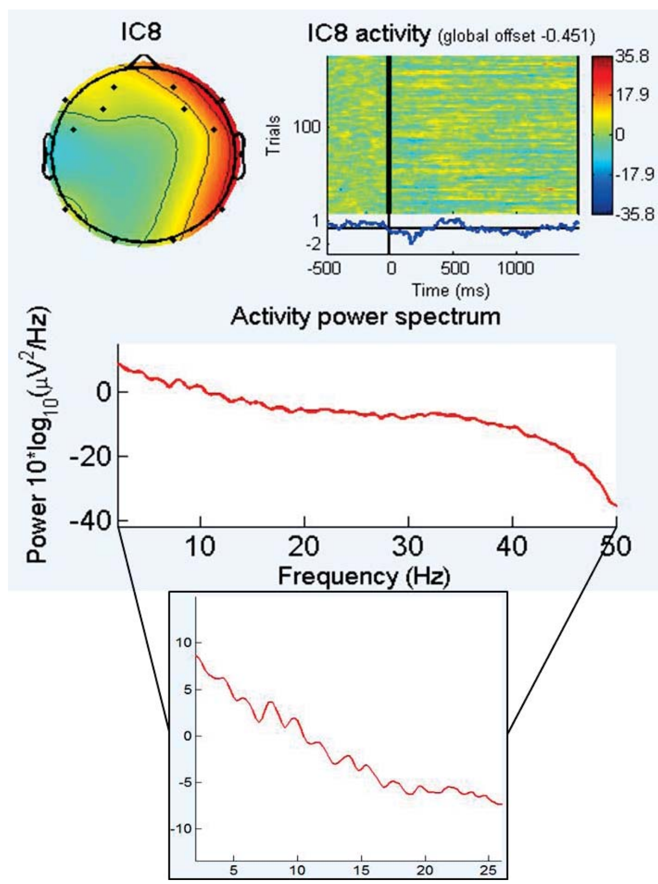

Fig. 9. Pulse artifacts, power spectrum shows two peaks between 5 and 10 Hz

4 Conclusions

A neurological occurrence is the only source of control in any BCI system. Artifacts are problematic signals that can affect with neurological phenomena. These artifacts may lead to the source of control in BCI systems. EMG and EOG artifacts are physiological artifacts that are carefully processed in BCI systems. This paper explained the common EOG, EMG, and non-physiological artifacts associated with our experiment. Artifact rejection procedure indicated the possibility of improvement into raw EEG signals. During artifact rejection, we considered the presence of EMG and EOG artifacts in the brain signals. Our results had shown the stability in brain signals after applying the artifact rejection such as, eye blink, eye movement, muscle movement, and bad channels.

Acknowledgement

This work was supported by the Brain Korea 21 PLUS Project, National Research Foundation of Korea, Business for Academic-Industrial Cooperative establishments that were funded by the Korea Small and Medium Business Administration in 2015 (Grants No. C0221114), MSIP (Ministry of Science, ICT and Future Planning), Korea, under the ITRC (Information Technology Research Center) support program (IITP-2016-R0992-16-1023) supervised by the IITP (Institute for Information & communications Technology Promotion), and National Research Foundation of Korea (NRF) grant funded by the Korea government (MEST) (No. 2012R1A2A2A03).

References

[1] O.-H. Cho and W.-H. Lee, "BCI Sensor Based Environment Changing System for Immersion of 3D Game," *International Journal of Distributed Sensor Networks,* vol. 2014, p. 8, 2014.

[2] L. Mayaud, M. Congedo, A. Van Laghenhove, D. Orlikowski, M. Figère, E. Azabou, and F. Cheliout-Heraut, "A comparison of recording modalities of P300 event-related potentials (ERP) for brain-computer interface (BCI) paradigm," *Neurophysiologie Clinique/Clinical Neurophysiology,* vol. 43, pp. 217-227, 2013.

[3] A. Alamri, M. M. Hassan, M. A. Hossain, M. Al-Qurishi, Y. Aldukhayyil, and M. S. Hossain, "Evaluating the impact of a cloud-based serious game on obese people," *Computers in Human Behavior,* vol. 30, pp. 468-475, 2014.

[4] M. S. Hossain, "Cloud-supported Cyber-Physical Framework for Patients Monitoring," *IEEE Systems J,* 2015.

[5] M. S. Hossain and G. Muhammad, "Cloud-based collaborative media service framework for healthcare," *International Journal of Distributed Sensor Networks,* vol. 2014, 2014.

[6] M. S. Hossain and G. Muhammad, "Cloud-assisted speech and face recognition framework for health monitoring," *Mobile Networks and Applications,* pp. 1-9, 2015.

[7] M. S. Hossain and G. Muhammad, "Audio-visual emotion recognition using multi-directional regression and Ridgelet transform," *Journal on Multimodal User Interfaces,* pp. 1-9, 2015.

[8] M. S. Hossain and G. Muhammad, "Cloud-assisted Industrial Internet of Things (IIoT)–Enabled framework for health monitoring," *Computer Networks,* 2016.

[9] M. S. Hossain, G. Muhammad, M. F. Alhamid, B. Song, and K. Al-Mutib, "Audio-Visual Emotion Recognition Using Big Data Towards 5G," *Mobile Networks and Applications,* pp. 1-11, 2016.

[10] A. Delorme and S. Makeig, "EEGLAB: an open source toolbox for analysis of single-trial EEG dynamics including independent component analysis," *J Neurosci Methods,* vol. 134, pp. 9-21, Mar 15 2004.

[11] G. Gómez-Herrero, W. De Clercq, H. Anwar, O. Kara, K. Egiazarian, S. Van Huffel, and W. Van Paesschen, "Automatic removal of ocular artifacts in the EEG without an EOG reference channel," in *Signal Processing Symposium, 2006. NORSIG 2006. Proceedings of the 7th Nordic*, 2006, pp. 130-133.

[12] A. Widmann and E. Schroger, "Filter effects and filter artifacts in the analysis of electrophysiological data," *Front Psychol,* vol. 3, p. 233, 2012.

[13] C. Babiloni, F. Carducci, F. Cincotti, P. M. Rossini, C. Neuper, G. Pfurtscheller, and F. Babiloni, "Human movement-related potentials vs desynchronization of EEG alpha rhythm: a high-resolution EEG study," *Neuroimage,* vol. 10, pp. 658-665, 1999.

[14] D. J. McFarland, L. M. McCane, S. V. David, and J. R. Wolpaw, "Spatial filter selection for EEG-based communication," *Electroencephalography and clinical Neurophysiology,* vol. 103, pp. 386-394, 1997.

[15] T. M. Vaughan, W. Heetderks, L. Trejo, W. Rymer, M. Weinrich, M. Moore, A. Kübler, B. Dobkin, N.

Birbaumer, and E. Donchin, "Brain-computer interface technology: a review of the Second International Meeting," *IEEE transactions on neural systems and rehabilitation engineering: a publication of the IEEE Engineering in Medicine and Biology Society,* vol. 11, pp. 94-109, 2003.

[16] R. Du, R. M. Mehmood, and H. J. Lee, "Alpha activity during emotional experience revealed by ERSP," *Journal of Internet Technology,* vol. 15, pp. 775-782, 2014.

[17] Y. Gao, H. J. Lee, and R. M. Mehmood, "Deep learninig of EEG signals for emotion recognition," in *Multimedia & Expo Workshops (ICMEW), 2015 IEEE International Conference on*, 2015, pp. 1-5.

[18] R. M. Mehmood and H. J. Lee, "ERP analysis of emotional stimuli from brain EEG signal," in *Int'l Conf. Biomedical Engineering and Science*, 2015, p. 5.

[19] R. M. Mehmood and H. J. Lee, "Exploration of Prominent Frequency Wave in EEG Signals from Brain Sensors Network," *International Journal of Distributed Sensor Networks,* 2015.

[20] R. M. Mehmood and H. J. Lee, "Emotion classification of EEG brain signal using SVM and KNN," in *Multimedia & Expo Workshops (ICMEW), 2015 IEEE International Conference on*, 2015, pp. 1-5.

[21] R. M. Mehmood and H. J. Lee, "EEG based Emotion Recognition from Human Brain using Hjorth Parameters and SVM," *International Journal of Bio-Science and Bio-Technology,* vol. 7, pp. 23-32, 2015.

[22] R. M. Mehmood and H. J. Lee, "Towards emotion recognition of EEG brain signals using Hjorth parameters and SVM," 2015.

[23] J. E. Moore Jr and D. J. Maitland, *Biomedical technology and devices*: CRC press, 2013.

[24] J. S. Barlow, "Artifact processing (rejection and minimization) in EEG data processing," *Handbook of electroencephalography and clinical neurophysiology,* vol. 2, pp. 15-62, 1986.

[25] Z. Khalili and M. Moradi, "Emotion detection using brain and peripheral signals," in *Biomedical Engineering Conference, 2008. CIBEC 2008. Cairo International*, 2008, pp. 1-4.

[26] M. Murugappan, N. Ramachandran, and Y. Sazali, "Classification of human emotion from EEG using discrete wavelet transform," *Journal of Biomedical Science and Engineering,* vol. 3, p. 390, 2010.

[27] P. J. Lang, M. M. Bradley, and B. N. Cuthbert, "International affective picture system (IAPS): Instruction manual and affective ratings," *The center for research in psychophysiology, University of Florida,* 1999.

[28] M. Bradley and P. J. Lang, *The International affective digitized sounds (IADS)[: stimuli, instruction manual and affective ratings*: NIMH Center for the Study of Emotion and Attention, 1999.

[29] EMOTIV. (2014, 12/12/2015). *EMOTIV EPOC BRAIN COMPUTER INTERFACE & SCIENTIFIC CONTEXTUAL EEG*. Available: https://emotiv.com/product-specs/Emotiv%20EPOC%20Specifications%202014.pdf

SESSION

BIOMEDICAL ENGINEERING AND IMAGING SCIENCE

Chair(s)

TBA

MELANOMA IMAGE SEGMENTATION USING SELF ORGANIZED FEATURE MAPS

Anirudh Munnangi[1], **Prabir Bhattacharya**[2]
[1]Electrical Engineering and Computer Science, University of Cincinnati, Cincinnati, OH, USA
[2]Electrical Engineering and Computer Science, University of Cincinnati, Cincinnati, OH, USA

Abstract - *This paper presents a SOFM (Self Organizing Feature Maps) model addressing the problem of segmentation of Dermoscopic skin cancer images. It proposes a unique way of passing information from the image to the network and shows how to interpret the output of the network. The main aim is to train the network so that it segments novel images correctly. The performance has been compared with standard existing methods and relevant comparative observations have been made. Experimental testing has been done on 420 Dermoscopic images which demonstrate the effectiveness of the model.*

Keywords: Dermoscopy, Kohonen networks, Image processing, Melanoma, Segmentation.

1 Introduction

Skin cancer (melanoma) detection is one of the most challenging problems faced by mankind. However, as per research, it is proven that it can be cured given its early and accurate detection. One of the established ways to perform the detection is through Dermoscopy. Dermoscopy is a non-invasive diagnostic technique for the in vivo observation of pigmented skin lesions used in dermatology [1]. Dermoscopy uses tools like non-polarized light, coupled with liquid medium and a transparent plate so as to get an effective image. The role of the specialist is to check these images and give the opinion regarding the status of the cancer. One major drawback of human based inference is that it subjects the detection process to human error based on the skills and experience of the person performing the diagnosis. So, it becomes prudent to have a second opinion which is given by the automated computerized detection approach [1].
The process of skin cancer detection is done stepwise and the individual steps are as follows:

1) Cleaning of images and artifacts;
2) Detection of the lesion segment;
3) Extracting required features
4) Classification.

Segmentation is an important step among them. Further processing is performed over the area where the segment lies on the image. If we don't have an efficient segment, the result can be quite misleading. There have been many approaches towards segmentation of Dermoscopic images.

G. Subha et al. [2] used Neural Network and related approaches towards the detection of cancerous lesion. The authors discuss various models like Radial basis Neural Network, Back Propagation based network which is generally a Multi-Layer Perceptron model and Extreme learning machine approach. A comparative performance survey was demonstrated. In [1], all the common and popular segmentation approaches have been discussed and have been applied towards the skin cancer problem. Techniques include Adaptive thresholding, Gradient Vector flow, Adaptive snakes, Level Set Methods, Expectation Maximization algorithm and fuzzy based approaches. Region growing and Region merging algorithm supported by Evolutionary model GA is discussed in [3]. In [4] an effective implementation of Neural Network based segmentation approach is discussed.

Neural Networks have always been debated in the literature and have been proven to generate better and promising results. In most cases, it acts like a good heuristic algorithm and in some sense we have limited information on how the algorithm is able to perform with an edge over traditional approaches. Also, Neural Networks are quite fast due to inherent parallelism. The reason for this is that each node in a Neural Network is essentially its own autonomous entity and each performs only a small computation in the grand-scheme of the problem and the aggregate of all these nodes, the entire network, is where the true capability lies [5].

Self-Organized Feature Maps (SOFM) are a sub domain of Neural Networks which is generally applied to clustering purposes. As the name suggests, SOFMs are unsupervised algorithms and they learn to organize their decisions in unison with other neurons towards the problem in focus. They have been used in many applications involving clustering, classification and speech/text recognition.

Self-Organized feature maps are directly related to the network model developed by Kohonen [9]. The Self-Organizing Map has the special property of effectively creating spatially organized "internal representations" of various features of input signals and their abstractions thereby enabling them to recognize semantics in various situations [9]. In a general SOFM system, only few neurons get the activation signal and due to the location of these neurons in the map, the whole system tends to be ordered as if some meaningful coordinate system has been generated [9].

To our knowledge, there is little literature on using SOFMs towards the problem of Dermoscopic skin cancer detection and hence that is one of the main motivations in presenting this work.

2 Self-Organized Feature Maps: Details

2.1 SOFM in General

Technically, the SOFM learns from examples by mapping (projection) from a high-dimensional continuous input space onto a low-dimensional discrete space (lattice) of N neurons which are arranged in fixed topological forms, e.g., as a rectangular 2-dimensional array [7]. A rectangular field is preferable for easy computational and array based approaches.

In SOFM, the neurons learn by unsupervised competitive learning amongst the other neurons and they try to map their weights in accordance to the input [5]. We present our input to the neurons in a desired way and the neurons try to learn those inputs and in the end up mimicking the inputs roles. The resulting map preserves the topology of the input samples in the sense that adjacent patterns are mapped into adjacent regions on the map and due to this topology-preserving property, the SOFM is able to cluster input information and spatial relationships of the data on the map [7]. In this way, a novel input can be easily shown to the network and its right niche or group can be found out. Competitive learning is also called Winner take all Networks where from a whole field of neurons, only the winning neuron is able to learn positively.

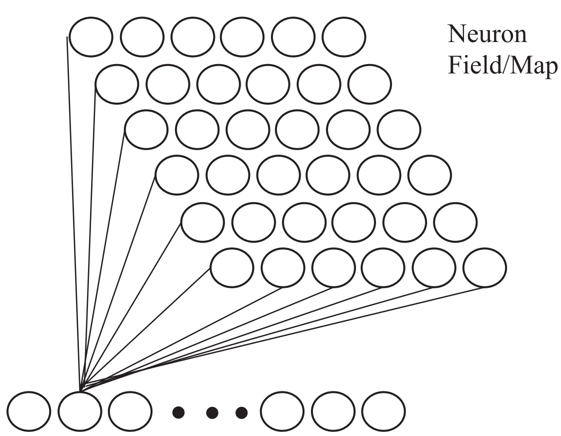

Figure 1. SOFM model [10]

The final organized Feature Map can be used for a lot of purposes out of which few are Clustering, Exploratory data analysis [6], visualization, removal of redundancy in data etc.

2.2 SOFM model

Here, we will see an example of a Neural Map and how the inputs are connected to the neurons.

In Figure 1, we can see a 6x6 map and a vector of inputs. The input vector is generated by the input values through some specific scheme. All the neurons are connected to all the input elements in the vector. Only one element and its connection is shown for better understanding. In this way the inputs are mapped to the neuron by vectors generated from the actual input values.

As the training process progresses, one of the neuron in the whole field wins and the weight gets mapped closer to its corresponding input. If we follow the winner take all rule, the winning neuron will get updated at the expense of others. This paper uses schemes where the update of other neurons involves dependency on their proximity to the winning neuron and that is seen in *section 2.3*

2.3 Mathematical Definitions

We can define the equation involved in the implementation of SOFM as follows:

As discussed earlier, that the SOFM field is generally in the shape of a square. For example in Figure 1, we see an example of a 6x6 field.

Let r_i be the ith neuron in the SOFM field.

Let the number of inputs to each neuron be n.

Let x^k be the vector of n inputs and X be the set of input vectors.

Then we can define the weight matrix with respect to that neuron as:

$$w_i = [w_{i1}, w_{i2}, \dots w_{in}]^T; \quad (1)$$

The training algorithm goes as follows:

1) Present $x^k \in X$(the set of input vectors)
2) Find the winning neuron as follows:
$$i^* = \text{argmin}||w_i - x_k|| \quad (2)$$
After finding the winning neuron, we can determine the location in the field of neurons.
3) We can then update the other weight by using the schemes below:

$$\Delta w_{ij} = \eta \Lambda(i, i^*, t)(x_j^q - w_{ij}) \tag{3}$$

Where,

$$\Lambda(i, i^*, t) = \exp[\frac{-\|r_i - r_{i*}\|^2}{2\sigma^2(t)}] \tag{4}$$

&

$$\sigma(t) = \sigma_0 \exp(\frac{-t}{\tau_n}) \tag{5}$$

Where σ_0 and τ_n are fixed parameters. r_i is the location of the neuron in the field.

From the above equations we can see that as the training time increases, we tend to decrease to the neighborhood impact on the learning of the neurons. As the training progresses the different training data result into different wining neurons and the weights are updated according to it.

3 Segmentation Algorithms

This section deals with the different segmentation algorithms used for comparison including the proposed approach using Self Organizing Feature Maps.

3.1 Otsu's Method

3.1.1 Method in general.

Otsu's methods is a regularly utilized method in the problem of segmentation and it has been used against the skin cancer issue quite regularly. The basic assumption in the application of Otsu's method is the existence of a bimodal histogram or class of pixels [12]. Other assumptions include uniform illumination and less or no usage of spatial values i.e. the structure. It generally results into a binary image which is the output with the segment being highlighted and the rest becoming the background. The benefit of Otsu's method stems from the fact that it uses an iterative scheme to find that factor so that in the end the intra-class variance in the pixels is minimized or the inter-class variance is maximized.

3.1.2 Mathematical definitions.

Let us assume that that the grayscale values are within [0, L-1] which implies there are L different levels. Let's say that the algorithm divides the image at the grayscale level't'. It will then result into two classes of grayscale levels which are [0, t] and [t+1, L-1]. These two classes will then be tested for the within-class as well as between-class variances.

The class probabilities are given as follows:

$$Pr_1(t) = \sum_{i=0}^{t} P(i) \tag{6}$$

$$Pr_2(t) = \sum_{i=t+1}^{L-1} P(i) \tag{7}$$

The class means can be found as follows:

$$\mu_1(t) = \sum_{i=0}^{t} \frac{iP(i)}{Pr_1(t)} \tag{8}$$

$$\mu_2(t) = \sum_{i=t+1}^{L-1} \frac{iP(i)}{Pr_2(t)} \tag{9}$$

The weighted within class variance can be calculated as follows:

$$\sigma_w^2(t) = Pr_1(t)\sigma_1^2(t) + Pr_2(t)\sigma_2^2(t) \tag{10}$$

Where the individual class variances can be found as follows:

$$\sigma_1^2(t) = \sum_{i=0}^{t} [1 - \mu_1(t)]^2 \frac{P(i)}{Pr_1(t)} \tag{11}$$

$$\sigma_2^2(t) = \sum_{i=t+1}^{L-1} [1 - \mu_2(t)]^2 \frac{P(i)}{Pr_2(t)} \tag{12}$$

The most efficient't' can be found out and the segment will then be generated.

3.2 Fuzzy C Means

3.2.1 Method in general.

Fuzzy C Means is an algorithm which partitions a set of n objects such as x={x_1, x_2, ….. x_N}in R^d dimensional space to C(1<C<N) fuzzy clusters with set y={y_1, y_2, ….y_C} being the cluster heads/centroids of the fuzzy clusters [13].
The fuzzy association is defined by a matrix μ which is also called the fuzzy matrix. As one can notice, the dimensions of the matrix is NxC. For example μ_{ij}, an element in the i^th row and j^th column in the matrix represents the association of the i^th object with the j^th cluster. The process starts with random clusters and then the association of the objects is found based on Euclidian distance metric. The centroids are then recalculated using Equation (13). This process is repeated until the centroid allotments match successively.

3.2.2 Mathematical definitions.

FCM algorithm aims to minimize the following equation

$$J_m = \sum_{j=1}^{C} \sum_{i=1}^{N} \mu_{ij}^m d_{ij} \tag{13}$$

Where

$$d_{ij} = \|x_i - y_j\| \tag{14}$$

In the above equations, m defines the fuzziness. In our implementation, after many trials, we have selected m=2 as it has shown better results. d_{ij} refers to the Euclidian distance between element x_i to cluster center in y_j.

3.3 Proposed approach using SOFM

Here, we describe our model and how we present the data to the neurons. Our data consists of skin cancer images as well as their segmented counterparts. Each image is of size 150x200 and its segment is also of the same size. We use data from an image and its segment together to form the training vector.

3.3.1 Neuron field.

Our neuron field consists of basically 150x200 neurons, each one of which caters to the decision at that pixel location as you can see from the size of the image. While training, we pass input vectors related to each pixel after consideration of both the images i.e. the image and its training segment; and this is done for all the pixels of an image. Also, similar steps are done for all the training images.
Since the size is 150*200, there are 30k neurons in our field and each neuron has weights of size 1x26. The reason of 26 weights is described in section 3.3.2.

3.3.2 Input vector generation.

The model which we are going to use is inspired by the one used in [10]. As discussed earlier, for every training image we have its corresponding segmented image. So let us denote the main image as X and its segmented image is Y.

Image X is in grayscale.
Image Y is in binary where '1' depicts segment pixel and '0' depicts surrounding pixel.

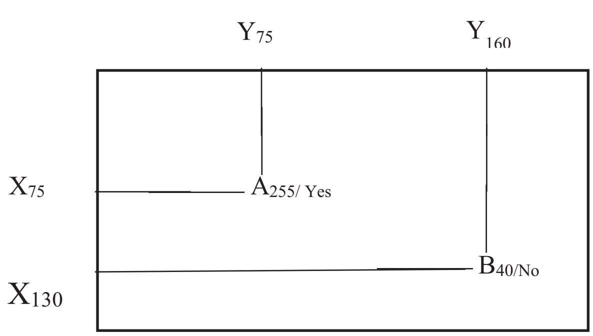

Figure 3. Image, pixel, location and grayscale value

While considering a certain pixel location at [a, b] where a and b are the coordinates;
- There will be a grayscale value (say g) in image X with 0<=g<=255.
- There will be binary value 0/1 in image Y.

We use the binary values of the coordinates, grayscale value in image X and the binary value in image Y altogether to form the input vector.
Mathematically, the input vector can be depicted as follows:

Inp_vec=[1x8 binary , 1x8 binary, 1x8 binary, 1x2 binary]
Where,The 'first' [1x8] binary is the binary value of the X-coordinate at the location of the pixel;

The 'second' [1x8] binary is the binary value of the Y-coordinate at the location of the pixel;
The 'third' [1x8] binary is the binary value of the grayscale value at the location of the pixel;
The 'fourth' [1x2] binary is the binary value of the segment decision which is sent as [1 0] for a segment pixel and [0 1] for a surrounding pixel.
So the total dimension of the Input Vector is [1x26].

For example in Figure 3, A and B are pixels. The subscript defines its grayscale value and whether it's a segment pixel or not. The coordinate locations are also mentioned.

$\text{Inp\_Vec}_{(A)}$ = [01001011 01001011 11111111 10]
$\text{Inp\_Vec}_{(B)}$ = [10000010 10100000 00101000 01]
The above vectors are sent for every pixel regarding one image and its segmented counterpart. Similar operations are done for all the training images.

3.3.3 Input vector generation while "Testing"

While testing, there is little change in the input vector. Only the last [1x2] binary matrix is replaced by [00]. We would only send the required location and pixel information. We let the network figure out whether the pixel should be a segment or not and we find it after thresholding the weights of the winning neuron.

4 Implementation and Comparisons

4.1 Datasets

In [17], Dermoscopy based work has been performed by the authors and the dataset including the results have been shared. It has been used as the training set mostly which consists of around 350 training images. Other testing source datasets are from dermis and dermquest which are public and thus open source.

4.2 Evaluation Methods

For the purpose of evaluation of our algorithm, we have selected five factors which are accuracy, sensitivity, specificity, Jaccard index and dice coefficient.
They can be calculated as follows:

$$Sensitivity = \frac{true_{positives}(TP)}{true_{positives}(TP)+false_{negatives}(FN)} \quad (15)$$

$$Specificity = \frac{true_{negatives}(TN)}{true_{negatives}(TN)+false_{positives}(FP)} \quad (16)$$

$$Accuracy = \frac{TP+TN}{TP+TN+FP+FN} \quad (17)$$

$$Jaccard_{index} = \frac{TP}{TP+FP+FN} \quad (18)$$

Jaccard Index is defined as the size of interaction of the two sets divided by the size of their union [14].

$$Dice_{coefficient} = \frac{TP}{\frac{1}{2}(TP+FN+TP+FP)} \quad (19)$$

Dice Coefficient is defined as the size of interaction of the two sets divided by their average size [15].

4.3 Table of measures

The values in table 1 are generated on average of all the *420* testing images together.

Segmentation Algorithm	Accuracy	Sensitivity	Specificity	Jaccard index	Dice coefficient
OTSU's Method	0.9464	0.7877	0.9643	0.7147	0.8179
FCM	0.9561	0.7960	0.9723	0.7080	0.8121
Proposed SOFM	0.9748	0.8624	0.9857	0.8586	0.9234

Table 1. Evaluation Parameters

4.4 Inferences

From Table 1 we can infer that, the proposed method has demonstrated better overall accuracy than the other two algorithms and this is an essential point. Sensitivity values are appreciable for the algorithms and are competitive amongst each other. The proposed method performs in a way which provides better results in comparison to Otsu's and FCM methods. It also shows improvements in other evaluation parameters.

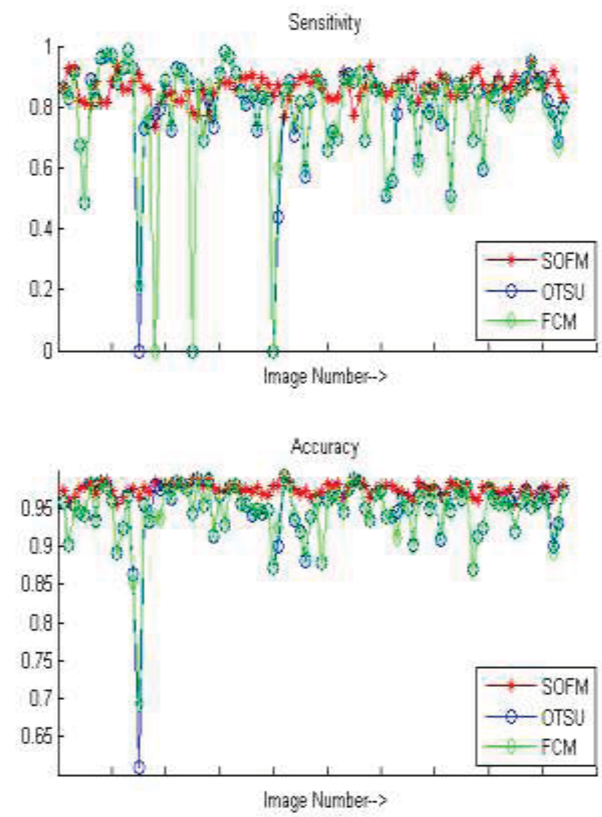

Figure 4: Comparison of Accuracy and Sensitivity of the algorithms

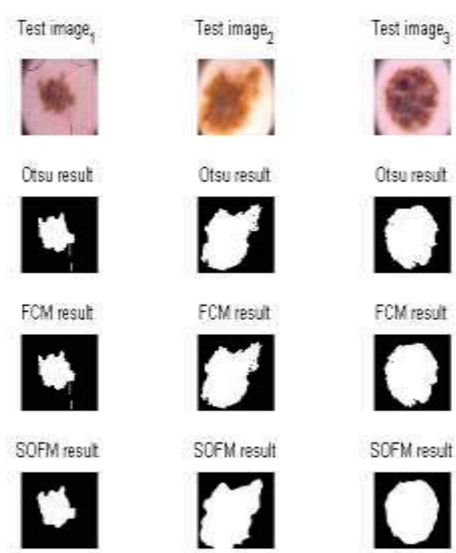

Figure 5: Comparison of Segmented images.

ISBN: 1-60132-429-4, CSREA Press ©

Figure 4 shows the variability of the parameters. We can see that the proposed method has comparatively better and consistent results which can be inferred by the lesser variability.

Figure 5 shows the different segments formed by the three algorithms and we can see that the proposed algorithm also works competitively against the other two.

5 Conclusion

As has been discussed in the paper, the proposed methodology has resulted relatively better results than the other existing methods. It has lesser fluctuation in the evaluation parameters which is a considerable sign of it being able to deal with novel data effectively. The main drawback noticed is the computational time in the proposed algorithm. However, after sufficient training, the method works very well in comparison to the other algorithms.

To further reinforce the findings of this paper, table 1shows how the methods have performed on an average over a large number of images together. We can see that our proposed algorithm has better performance when averaged over many test samples. Any discrepancies and variations in the results stem from the fact that all test samples are from entirely different datasets when compared to the training set. Further efforts will include improvements to the algorithm by adopting evolutionary/metaheuristic approaches.

6 References

[1] M Silveria, J C Nascimento, J S Marques, André R S Marcal, T Mendoca, S Yamauchi, J Maeda & J Rozeira, Comparison of Segmentation Methods for Melanoma diagonosis, in Dermoscopy images, IEEE journal of selected topics in Signal Processing, Vol 3 No 1, Feb-2009

[2] G S Vennila, L P Suresh & K L Shanmuganathan, Dermoscopic Image Segmentation and Classification using Machine Learning Algorithms, ICEET-2012

[3] Angelia S, L. Padma Suresh & S.H Krishna Veni, Image Segmentation based on Genetic Algorithm for region growth and region merging, ICEET-2012

[4] L Jinali & Z Baoqi, The Segmentation of skin cancer images based on genetic Neural Network.

[5] Shyam M. Guthikonda, Kohonen Self-Organizing Maps, Wittenberg University, December 2005

[6] A.Ultsch and H.P. Siemon, Kohonen's SeIf Organizing Feature Maps for Exploratory Data Analysis, Institute of Informatics University of Dortmund.

[7] Guilherme DE A. Barreto & Aluizio F. R. Araújo, Self-Organizing Feature Maps for modelling and control of robotic manipulators.

[8] R J Kuo, L M Ho & C M Hu, Integration of Self organizing feature map and K-means algorithm for market segmentation, Computers & Operations Research 29 (2002) 1475-1493, Elsevier Feb-2001.

[9] Teuvo Kohonen, The Self Organizing Map, Proceedings of the IEEE, VOL. 78, NO 9, SEPTEMBER 1990.

[10] Dmitri G Roussinov & Hsinchun Chen, A Scalable self-organizing map algorithm for textual classification: A Neural Network approach to thesaurus generation, Building the Interspace: Digital Library Infrastructure for a University Engineering Community," PIs: B. Schatz, H. Chen, et al., 1994-1998, IRI9411318

[11] S. Haykin, Neural Networks: A Comprehensive Foundation, Prentice-Hall, 1999

[12] Harpreet Kaur & Aashdeep Singh, Enhanced Skin Cancer detection techniques using Otsu segmentation method. IJARCSSE, Vol5 issue 5, May 2015

[13] Mahesh Yambal & Hitesh Gupta, Image Segmentation using Fuzzy C-means Clustering: A survey, IJARCCE, Vol. 2 Issue 7, July 2013.

[14] D A Santana-Calvo, Vargas Olivares, S Pichardo, L Curiel & JE Chong-Quero. Evaluation methods of image segmentation quality applied to magnetic resonance guided high-intensity focused ultrasound therapy. VI Latin American Congress on Biomedical Engineering CLAIB 2014, Paraná, Argentina 29, 30 & 31 October 2014, IFMBE Proceedings 49.

[15] David W Shattuck, Gautam Prasad, Mubeena Mirza, Katherine L. Narr, Arthur W Toga, Online resource for validation of brain segmentation methods, Elsevier-NeuroImage-Nov 25 2008.

[16] Aaron Fenster, Bernard Chiu, Evaluation of Segmentation algorithms, Proceedings of the 2005 IEEE Engineering in Medicine and Biology 27th Annual Conference, September 1-4, 2005

[17] Teresa Mendonça,Pedro M. Ferreira, Jorge Marques, Andre R. S. Marcal, Jorge Rozeira, PH² - A Dermoscopic image database for research and benchmarking, 35th International Conference of the IEEE Engineering in Medicine and Biology Society, pp.5437-5440, July 3-7, 2013.

Perspective and orthogonal CBCT/CT digitally reconstructed radiographs compared to conventional cephalograms

J.Jesús Montúfar[1], Marcelo Romero[1], V. Muñoz-Jiménez[1], Rogelio J. Scougall-Vilchis[2] and Brissa Jiménez[2]
Facultad de Ingeniería[1] y Facultad de Odontología[2]
Universidad Autónoma del Estado de México

{jdmontufart, mromeroh, vmunozj, rscougallv, bijimenezv}@uaemex.mx

***Abstract*—The aim of this paper is to compare conventional radiographs, with those synthesized from CBCT/CT volumes. Four methods for generating Digitally Reconstructed Radiographs (*DRR's*) were compared: Ray-Sum, Radon Transform, Siddon's Algorithm and an hybrid approach. Three random skulls were used as the CT/CBCT input, each one with their conventional cephalometric lateral radiograph to validate results. Volume data in *DICOM* format were imported into Matlab, and orthogonal and perspective lateral projection were created. The PSNR (peak signal-to-noise ratio) measured the difference between DRR's and conventional digital radiographs. Finally, applications of the most similar *DRR* to a conventional cephalogram are discussed, considering that the use of CBCT images in orthodontics also allows 3D cephalometry and provides full information about the structure of each patient.**

***Index Terms*—reconstructed radiography, cone beam tomography, cephalometry, projections**

I. Introduction

A cephalogram is primarily used to describe the morphology of the craniofacial skeleton in orthodontics. A cephalometry is a procedure in which human skull measures are defined from lateral cephalogram [16], is a standardized method that is part of the diagnostic, treatment and planning process in different types of maxillofacial surgery and orthodontics. Recently, Computed Tomography (CT) and Cone Beam CT (CBCT), were introduced to the dental community as a diagnostic tool and has became a standard imaging technique in orthodontics [10], [16]. This is because tomography scans provide accurate 3D information of size and position of the patient volume. Both, CT and CBCT images allow reforming the three-dimensional structure of the skull into 2D conventional simulated X-ray images or *DRR's* for cephalometry, keeping size and position, then *DRR's* can be defined as a 2-D simulated approximation of a radiograph [2]. *DRR* rendering, is a DVR (Direct Volume Rendering) technique consisting in virtual x-rays passing through a reconstructed CT volume and is also called simulated X-ray volume rendering.

Nowadays, three-dimensional arrays of data are usually generated by Cone Beam Computed Tomography (CBCT) to be analyzed and visualized by volume rendering techniques to ease interpretation. These methods allow experts to see interior structures and spatial relationships of a patient skull. Then, cephalometry can be performed by using not only a single X-ray image, e.g. Moshiri *et al.* [9] presented a cephalometry method for *DRR's* with CBCT showing the importance of using *DRR* for this procedure. Figure 1.1 shows the general scheme for DVR by using the original slices of a CT scan viewed as a three-dimensional array that can be processed to obtain a *DRR*. Finally, the main problem of this ray-driven methods is still connected with a long computation time especially in CBCT high resolution sets [8].

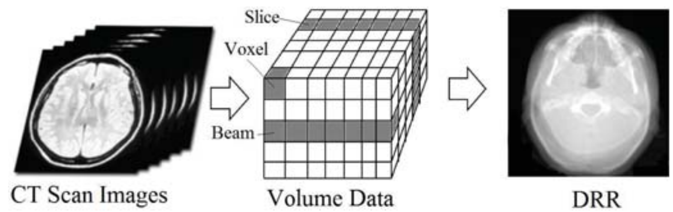

Figure 1.1. Direct volume rendering scheme. From volumetric CT scan formed by a set of N images a 3D array of voxels can be created and finally by using a ray casting algorithm for rendering, a new image of a reconstructed X-ray image is created.

II. Materials and Methods

In this study, we used the examinations of the head of three patients, two head CBCT volumes provided by the Faculty of Odontology, Autonomous University of the State of Mexico and a CT public volume dataset provided in the DICOM sample image sets from OsiriX [11] (MANIX). The CBCT volumes consists of 528 and 503 slices and isometric voxel 0.4mm size. The third volume is a CT scan consisting of non-isometric voxels with 460 slices separated for 0.7 mm. All volumes are in DICOM format and were used and analyzed to test the reconstruction algorithms. Figure 2.1 shows the Multiplanar Reconstructions (MPR) of the used volumes, rendered in 3DSlicer. The DICOM data were loaded into Matlab without any preprocessing to generate *DRR's*. All volume keeps voxels with density values of the digitized material as it is. Then,, generation of *DRR* is treated as volume rendering or X-ray simulation. The technique consists of simulated x-rays passing through the MPR volume and is directly based on the law of attenuation absorption [7]. *DRR's* can be directly rendered from the volume by a variety of algorithms using the operations called *ray-driven*, as *DRR* rendering is a special case of volume rendering. Techniques by *ray-driven* for rendering *DRR* images can be grouped into two categories: image-based (backward-projective) or object-based (forward-projective) [14]. A 3D virtual patient head was created from each study and the Frankfort plane of each volume was oriented horizontally based on the sagittal plane. An orthogonal and perspective radiographs were built from the reoriented volumes. Parallel beam rays created the orthogonal projections and for perspective projections, the source of the rays was the center of projection (focus) 1000-1500 mm away from the projection plane. In perspective, the location of an object between the focus and the projection plane determines its size. A scheme is in Figure 2.5. The orthogonal radiographs were created with 0% magnification and perspective radiographs were created using 5-8% magnification in the mid-sagittal plane.

Figure 2.1. Volumes created from CBCT (left/center), and volume created from a conventional CT from the public dataset MANIX provided in the DICOM sample image sets from OsiriX [11] , all MPR in 3DSlicer [12].

A. Ray-sum Algorithm

Ray-Sum is a technique whereby hypothetical X-ray are sent from each pixel of a source towards the volume to a final image in the screen. The objective is to sum all the ray lengths through all the voxels in CT volume data multiplied by voxel densities to get the radiological path.

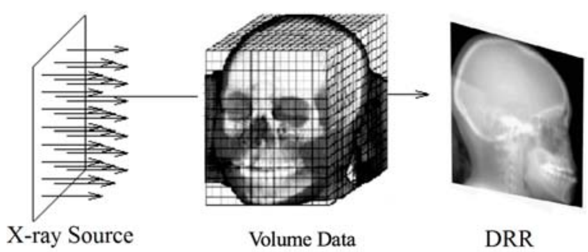

Figure 2.2. In Ray-Sum, 3D data (voxels) is displayed by the average of all intensities from the rays source to the projection plane forming the *DRR*.

The values associated with the voxels determine what happens to each ray and therefore what image is finally reconstructed. For each pixel of the final image on the screen, a ray is used to intersect parallel voxels in the volume (just one direction). Each pixel of the projection gets a 12-bit value by averaging all intensities of the intersected pixels. This view has a translucent appearance analogous to conventional radiographs. Figure 2.2 shows the scheme of the source of simulated rays, volume and detector configuration to get a *DRR*.

Ray-sum algorithm is a forward projection $\rho(i,j,k)$ denote the voxel attenuation (gray level intensity) in a 3-dimensional CT volume and $l(i,j,k)$ the length of the intersection of an X-ray with that voxel, then the radiological path is defined as:

$$d = \sum_i \sum_j \sum_k l(i,j,k)\rho(i,j,k) \quad (1)$$

The value d represents the sum of the contribution of the intensities associated to a density value (in Hounsfield units) of the simulated radiological path of the ray [13]. The simulated radiological path is parallel, and this approximation is away from the physics involved when an X-ray image is generated, but the resultant *DRR* has no distortion or magnification as in the conventional X-ray capture. Computing *DRR's* using this algorithm is $O(n^3)$ and may result inefficient because many voxels and paths values will be zero [1]. The *DRR* created by this projection must be post-processed with filters to get better contrast and sharpness in radio-lucid and radio-opaque zones to correctly detect cephalometric landmarks by an orhodoncist, surgeon or a computer program.

B. Radon transform

In this method, *DRR's* are generated from the CT volume data by computing the attenuation of a monoenergetic beam due to different material in the human body (e.g., bone, soft tissue, water, etc.).

$$I = I_0 exp - \int_0^D \mu(x)dx \quad (2)$$

By equation (2), the Beer's Law [4], the Radon transform is applied to the intensity image formed by each slice of the volume data i a discrete way. The Radon transform is the projection of the image intensity along a radial line oriented at a specific angle. For *DRR's,* a projection of a 2D function $f(x,y)$ is a set of line integrals, and the radon transform computes the line integrals from a source along parallel paths, or beams. The beams are spaced by each pixel unit in the detector. To represent a *DRR*, parallel-beam projections of an image from the same angle for each slice in volume data are calculated. The following Figure shows a single projection at a specified rotation angle.

When an individual ray has passed through the volume data, its value is:

$$I = I_0 \sum_{i=1}^{n} e^{-\mu_i d_i} \quad (3)$$

where I_0 is the original ray value, i is the voxel through which the ray passes, μ_i is the linear attenuation coefficient of the material in voxel i and d_i is the segment between the entrance and output point of the ray in voxel i. The attenuation coefficient of the material for each voxel can be obtained by:

$$CTnumber = 1000*[(\mu_i - \mu_w)/\mu_w] \quad (4)$$

where μ_w is the linear attenuation coefficient of water for the average energy in the CT beam.

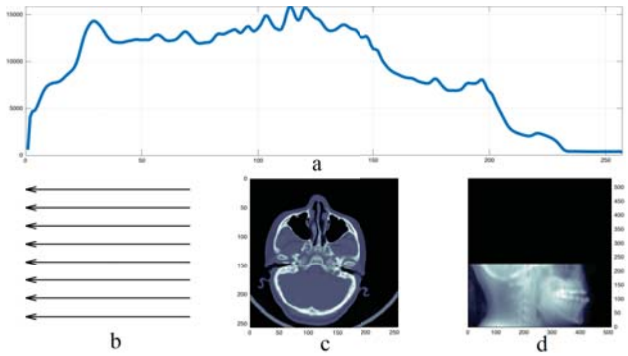

Figure 2.3. For each slice in the CT volume data, radon transform is used to obtain an attenuation profile (a) following the direction of the X-ray beam (b), in this case to reconstruct a sagittal projection. Image (c) is the actual slice and (d) is the set of the acumulated transforms that construct the *DRR*.

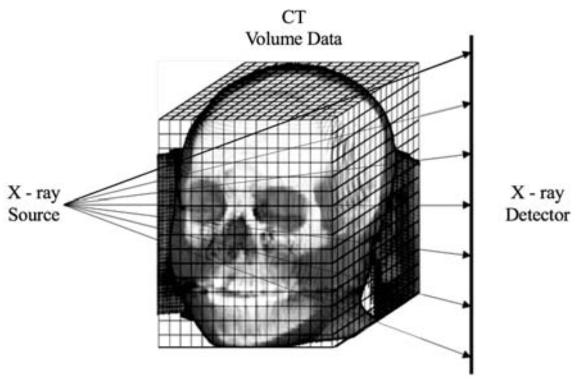

Figure 2.4. This scheme illustrates a 3D ray tracing though a volume data array. The lines from the simulated X-ray source on parametric planes indicate the tracing. The tracing can be done in any plane to get *DRR's* from any angle.

C. Siddon´s Algorithm

The equation (1) can be evaluated over all voxels in the volume, but results inefficient and time consuming, Siddon [15] proposed a more efficient method by viewing volume data voxels as the intersection of equally spaced, parallel planes. The intersection of the ray with the planes is then calculated, rather than the intersection of the ray with the different voxels. The intersection with the first plane is calculated and the rest follows at fixed intervals because the planes are equally spaced. The data in the CT array may be considered as the intersection areas of orthogonal sets of the equally spaced, parallel lines. Two equally spaced sets give the intersections of the ray with the lines: one set for the horizontal lines and another set for vertical lines [15].

D. Ray-Sum and Radon transform for cone beams.

The fourth method is an hybrid approach that takes algorithms A and B and transforms the parallel beam shape rays into a cone beam shape. A conventional radiograph capturing scene is reconstructed. Radiological paths are conducted from a source of X-rays centered on a point around 1000mm away from the volume centroid. A detector of nxn pixels is also placed from 300 to 500 mm of the centroid of volume in opposite side to the source. Figure 2.5 shows the scheme of

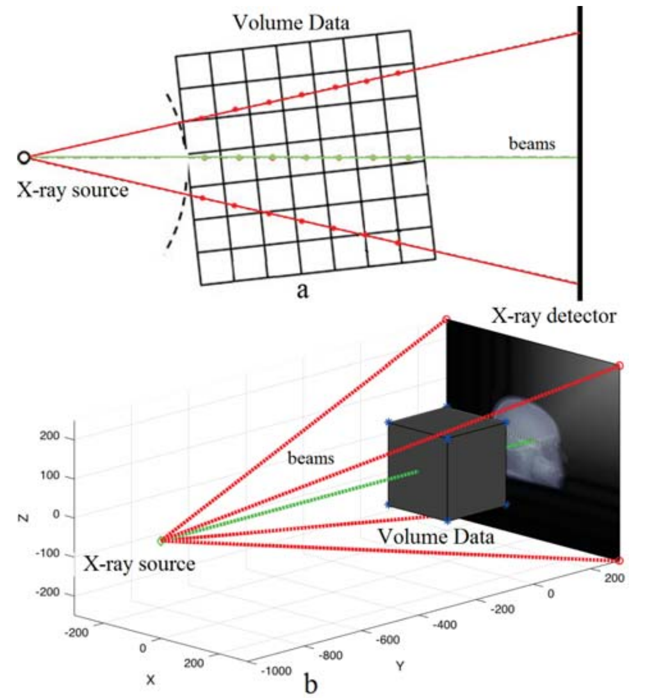

Figure 2.5. 2-D (a) and 3-D (b) illustrations of the configuration when X-rays in a cone beam intersect with a CT/CBCT volume. In some cases sample points can be located within the same voxel producing blurred projections.

the configuration used for generating *DRR* using this method. The magnification in *DRR's* was calculated using conventional digital radiographs parameters, the distance between the source and the mid-sagittal plane in the volume was 1500mm, and the distance between the detector and the mid-sagittal plane in the volume was 100mm [5]. Thus, the *DRR's* magnification was [5]:

$$Magnification = \frac{100}{1500}x100\% = 6.66\%$$

Perspective CBCT projections were adjusted for the 6.66% magnification to simulate conventional digital radiographs.

III. Results

The generation of a *DRR* comprises the calculation of line integrals over the Hounsfield values along the rays through the voxel volume. The rays are defined by the focal spot of the (virtual) X-ray source, and a discrete point on the (virtual) detector grid.

For the evaluation of the *DRR's*, we compute the difference between the outputs of intensity-based registrations of the calculated *DRR's* and the conventional X-ray image by applying a rigid transformation. Differences between radio-opaque and radio-lucid zones were the reference to determine which image could be better for cephalometry. Figure 3.4 shows this process, and the PSNR between the conventional digital Radiograph and all generated *DRR's*. PSNR and Mean Square Error (MSE) [3] were used to compare the squared error between the original image and the reconstructed image. There is an inverse relationship between PSNR and MSE. A higher PSNR value indicates the higher quality of the image. The answer in decibels (dB), in our tests using the method of the Radon

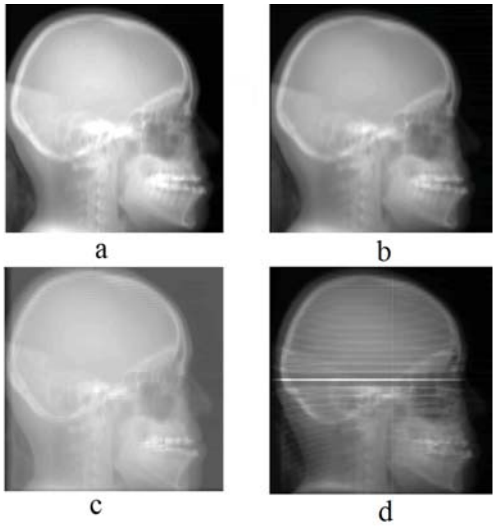

Figure 3.1. Example for *DRR* generation of a skull in its sagittal view from CT using the four methods (a) shows a sample using Ray-Sum, (b) shows the use of Radon transform, (c) shows the use of Siddon´s Algorithm and (d) the Radon transform with cone beams.

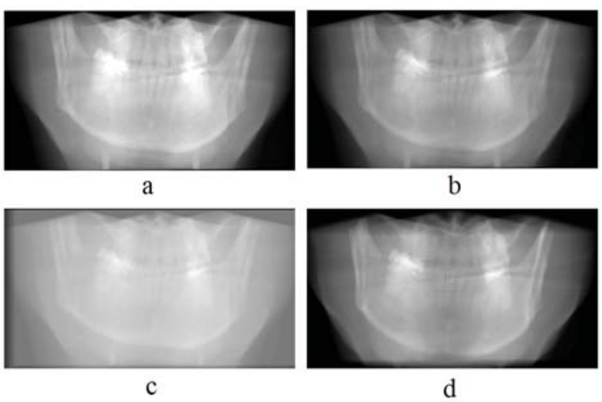

Figure 3.2. Example for *DRR* generation of mandible-maxilla in its coronal view from CBCT using the four methods (a) shows a sample using Ray-Sum, (b) shows the use of Radon transform, (c) shows the use of Siddon´s Algorithm and (d) the Radon transform with cone beams.

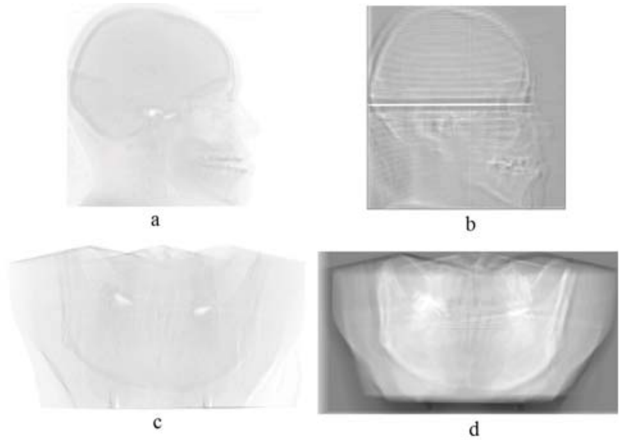

Figure 3.3. Image (a) shows the difference image, formed after registering images, by pixel subtraction between image 3.1a and 3.1b while (b) shows the difference image formed by pixel by pixel subtraction between image 3.1c and 3.1d. Image (c) shows the difference image, formed after registering images, by pixel by pixel subtraction between image 3.2a and 3.2b and (d) shows the difference image formed by pixel by pixel subtraction between image 3.2c and 3.2d (white pixel = no difference).

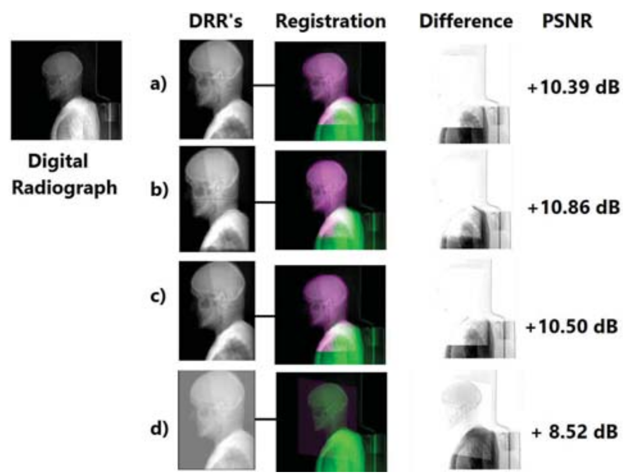

Figure 3.4. Sample *DRR's* generated using the for methods tested compared with a conventional digital radiograph generated using X-ray. The *DRR's* are computed in sagittal direction from a CT image of the head region using (a) Ray-Sum, (b) the Radon transform with cone beam, (c) the Radon transform and (d) Siddon´s Algorithm. The conventional digital radiograph is shown on the left. The next column shows *DRR's* generated from all tested methods. The next column shows difference images between the conventional digital radiograph and each method. The last column showns the PSNR values, the highest value indicates less difference between the images.

transform with perspective cone beams get the highest value with +10.86 db, that indicates this *DRR* is the most similar to the conventional digital radiograph. In the other hand, the next better value was +10.50 obtained by the method of the Radon transform with orthogonal parallel beams. It indicates that the generated *DRR* is very similar to the conventional digital radiograph but with the main difference that is has not magnification. The *orthogonal projections DRR's* shows that radiographs without magnification can be matched to its CT/CBCT volume and the cephalometric landmarks in the mid-sagittal plane should be the same, therefore, *orthogonal projections DRR's* could be used for the 2D conventional cephalometric analysis and in the future for 3D cephalometric analysis.

IV. Discussion

Before discussing our results, it is important to reiterate that the motivation to evaluate different methods for generating *DRR's* is to use them for cephalometry. In orthodontics lateral and frontal cephalograms, both with facial photographs are currently the main diagnostic imaging modalities for diagnostic. A CBCT/CT scan provides good quality medical information and also allows 3D cephalometry, providing to patients and practitioners a better understanding of the 3D skull structure. In conventional cephalograms, structures overlap by the projection onto a 2D plane. Using 3D CBCT images in cephalometry, has more advantages apart from the 2D reconstructed radiographs like reduced radiation exposure, natural shape of the soft-tissue facial mask, reduced occlusion and in-office imaging.

In this study, we explore the feasibility of using *DRR's* from

Figure 4.1. Conventional cephalogram with inherent magnification of 7.5% [6] (left) and the orthogonal cone-beam computed tomography projection without magnification (right).

CT that can be used to perform a cephalometric analysis. The *DRR* needs to be post-processed. Beside, there is a low contrast between radio-lucid and radio-opaque zones which makes landmark identification difficult and with low accuracy. The difference errors of both *DRR* were mostly by the distortion and magnification by the distances between object and source and the object and detector. The importance of generation of X-ray images from CT is to use all the information provided by only one CT scan to get explicit depth information of all structures of a patient as it is mentioned before. Advances in CBCT imaging for cephalometry will be more readily accepted by clinicians if the cephalograms can be synthesized similar to the ones they are familiar with and have used for several decades.

The orthogonal CBCT projections provided images closest to the skull and were more precise than the perspective projections by the absolute differences. Magnification and distortion in perspective projections affect the sizes of this kind of projections in comparison to the orthogonal ones and even with the real patient's head. New studies have to be developed to improve capturing protocols to get better projections for a reconstructed image. In the other hand, introducing new concepts for virtual planning and diagnosis for maxillofacial treatments, promotes the use of new technologies while leaving aside traditional methods. Virtualize orthodontics and maxillofacial diagnosis by automatic cephalometric analysis permits prior interventions and prevents improvisations while achieving more precise procedures, not only in 2D. If an acceptable cephalogram can be reconstructed, an automatic 2D and 3D cephalometric analysis can be performed and new concepts for cephalometry can be applied to three-dimensional images.

V. Conclusions

We have described four methods for generation of Digitally Reconstructed Radiographs (*DRR's*), by processing intensity-Hounsfield voxel values, in 3D CT/CBCT datasets. The slices are then projected onto a virtual detector, where the projected values are added or changed. The presented approaches do not require any pre-processing, apart from the transfer of the volume data to the *Matlab workspace* where the *DRR's* are generated. We analyzed the effects of two types of simulated x-rays beams. According to the PSNR values, both projections, orthogonal and perspective *DRR's* can be considered similar to a conventional radiograph. Therefore, they can be used to perform a cephalometric analysis. Orthogonal projection *DRR* could provide greater accuracy in the localization of mid-sagittal cephalometric landmarks than both, perspective projection *DRR* and conventional cephalometric images, because *orthogonal projection DRR's* produce matches to actual CT/CBCT that do not require any adjustment, e.g. scaling.

Acknowledgment

Authors thank the Research Department of the Autonomous University of the State of Mexico and the National Council for Science and Technology (CONACYT) for their support (CVU 468208).

Conflict of interest

The authors declare that they have no conflict of interest.

References

[1] Cobus Carstens and Neil Muller. Fast calculation of digitally reconstructed radiographs using parallelism. In *Proceedings of the Eighteenth Annual Symposium of the Pattern Recognition Association of South Africa*, pages 57–62. Durban, South Africa, 2007.

[2] Osama M Dorgham, Stephen D Laycock, and Mark H Fisher. Gpu accelerated generation of digitally reconstructed radiographs for 2-d/3-d image registration. *Biomedical Engineering, IEEE Transactions on*, 59(9):2594–2603, 2012.

[3] Rafael C Gonzalez et al. Re woods, digital image processing. *Addison–Wesely Publishing Company*, 1992.

[4] AC Kak and M Slaney. Principles of computerized tomographic imaging (piscataway, nj: Ieee). 1988.

[5] Vandana Kumar, JB Ludlow, A Mol, and L Cevidanes. Comparison of conventional and cone beam ct synthesized cephalograms. *Dentomaxillofacial Radiology*, 2014.

[6] Vandana Kumar, John Ludlow, Lucia Helena Soares Cevidanes, and André Mol. In vivo comparison of conventional and cone beam ct synthesized cephalograms. *The Angle orthodontist*, 78(5):873–879, 2008.

[7] Xiaoliang Li, Jie Yang, and Yuemin Zhu. Digitally reconstructed radiograph generation by an adaptive monte carlo method. *Physics in medicine and biology*, 51(11):2745, 2006.

[8] B De Man and S Basu. Distance-driven projection and backprojection. In *Nuclear Science Symposium Conference Record, 2002 IEEE*, volume 3, pages 1477–1480. IEEE, 2002.

[9] Mazyar Moshiri, William C Scarfe, Michael L Hilgers, James P Scheetz, Anibal M Silveira, and Allan G Farman. Accuracy of linear measurements from imaging plate and lateral cephalometric images derived from cone-beam computed tomography. *American Journal of Orthodontics and Dentofacial Orthopedics*, 132(4):550–560, 2007.

[10] P Mozzo, C Procacci, A Tacconi, P Tinazzi Martini, and IA Bergamo Andreis. A new volumetric ct machine for dental imaging based on the cone-beam technique: preliminary results. *European radiology*, 8(9):1558–1564, 1998.

[11] OsiriX. Osirix advanced open-source pacs workstation dicom viewer. http://www.osirix-viewer.com/datasets/, January 2016.

[12] Steve Pieper, Michael Halle, and Ron Kikinis. 3d slicer. In *Biomedical Imaging: Nano to Macro, 2004. IEEE International Symposium on*, pages 632–635. IEEE, 2004.

[13] Daniel Ruijters, Bart M ter Haar Romeny, and Paul Suetens. Gpu-accelerated digitally reconstructed radiographs. *BioMED*, 8:431–435, 2008.

[14] Aodong Shen and Limin Luo. Point-based digitally reconstructed radiograph. In *Pattern Recognition, 2008. ICPR 2008. 19th International Conference on*, pages 1–4. IEEE, 2008.

[15] Robert L Siddon. Fast calculation of the exact radiological path for a three-dimensional ct array. *Medical physics*, 12(2):252–255, 1985.

[16] Peter J Taub, Pravin K Patel, Steven R Buchman, and Mimis Cohen. *Ferraro's Fundamentals of Maxillofacial Surgery*. Springer, 2014.

Medical Images Verification using Statistical Features and Back Propagation Neural Network

Prof. Dr. Adil AL-Rammahi
Mathematic Department
Faculty of Computer Science and Mathematics
Kufa University, Iraq
adilm.hasan@uokufa.edu.iq

Prof.Hind Rustum Mohammed
Computer Department
Faculty of Computer Science and Mathematics
Kufa University, Iraq
hindrustum.shaaban@uokufa.edu.iq

Hasan Abd Al-Hussein
Mathematic Department
Faculty of Computer Science and Mathematics
Kufa University, Iraq
hassanmath89@gmail.com

Abstract

In the present paper, Medical Image Verification using statistical factors and back propagation Neural Network is proposed. Database consists of 200 images (100 image for satisfactory skin cancer, 100 image for unsatisfactory skin), types for image .jpg , .png and .bmp image formats. Database prepared in our conditions. Indeed the images obtained (50 image for satisfactory skin cancer, 50 image for unsatisfactory skin), other images obtained from internet (50 image for satisfactory skin cancer, 50 image for unsatisfactory skin). Testing stage consists of 80 images (20 image for satisfactory skin cancer, 20 image for unsatisfactory skin cancer) from in Al-Seder Hospital and (20 image for satisfactory skin cancer, 20 image for unsatisfactory skin cancer) from internet. The experiment results confirm the effectiveness of the proposed algorithm.

Keyword Back propagation Neural Network, statistical parameters

1. Introduction

A simple and effective recognition scheme is to represent and match images on the basis of color histograms as proposed by Swain and Ballard [2].

An Artificial Neural Network (ANN) is an information processing paradigm that is inspired by the way biological nervous systems, such as the brain, process information. The key element of this paradigm is the novel structure of the information processing system. It is composed of a large number of highly interconnected processing elements (neurons) working in unison to solve specific problems. ANNs, like people, learn by example. An ANN is configured for a specific application, such as pattern recognition or data classification, through a learning process. Learning in biological systems involves adjustments to the synaptic connections that exist between the neurons. This is true of ANNs as well [3].

The applications of ANNs in medical image processing have to be analyzed individually, although many successful models have been reported in the literature. ANN has been applied to medical images to deal with the issues that cannot be addressed by traditional image processing algorithms or by other classification techniques. By introducing artificial neural networks, algorithms developed for medical image processing and analysis often become more intelligent than conventional techniques [4].

For updated related works, Andrius Ušinskas etal described a new method to segment ischemic stroke region on computed tomography images by utilizing joint features from mean, standard deviation, histogram, and gray level co-occurrence matrix methods. Presented unsupervised segmentation technique shows ability to segment ischemic stroke region [11]. Researcher FEI GAO has a master thesis about a survey of image segmentation methods and their possible applications to identify Cervical Intraepithelial Neoplasia (CIN) [12]. Huajun Ying *et al.* proposed an algorithm to detect the optical disk location in retinal images depends on the fractional dimension [13]. Dr. J. Abdul Jaleel *et al* .presented a paper about the early detection of skin cancer using Back-Propagation Neural Network. It classifies the given data set into cancerous or non-cancerous [14].Ahmed Sami introduced A master thesis about bone cancer and it has been classified into groups based on a variety of different features of statistical and neural network with the deployment of reverse discrimination images represent different samples of bone disease [20].

2. The Segmentation of Image

The autonomous machine perception task is achieved by a number of steps. The initial step is the segmentation of the image into a meaningful region or object. When analyzing a region or object in an image it is vital that we distinguish between the object of interest and the background. From this division, the object can be identified by its shape or from other features. The segmentation task usually starts with the extraction of the limits of the object. These limits are commonly called "edges". Moreover, an object contour, which may be constructed from the compacted information provided by these edges, can facilitate the measurements on the object [1].

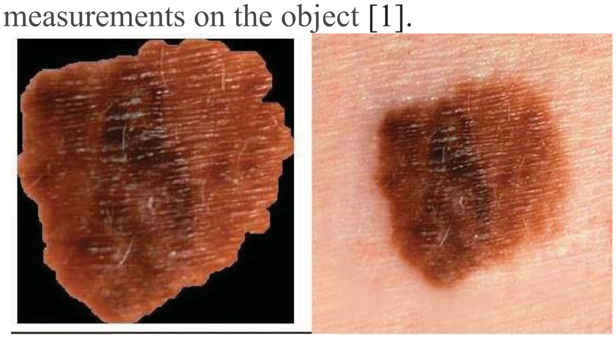

Figure 1: segmentation of the image(the right is the original image while the left is the segmented image using Otsu's method)

3. Feature extraction and Back propagation neural network

Feature extraction is a general term for methods of constructing combinations of the variables to get around these problems while still describing the data with sufficient accuracy [3]. There are different types of features such as global, grid, texture, and local feature. Global features provide information about specific cases concerning the structure of the signature. Many object recognition systems use global features that describe an entire image. Most shape and texture descriptors fall into this category. Such features are attractive because they produce very compact representations of images, where each image corresponds to a point in a high dimensional feature space. As a result, any standard classifier can be used[4]. There are many Global features such as in Table(1) [5.6].

4. The Structure of Neural Network

We used a feed forward backpropagation neural network with adaptable learning rate. The NN have 3 layer; an input layer (10 neuron), a hidden layer (50 neuron) , and output layer (2 neuron), We have put a desired output 1 for Sick skin images and 0 for Intact skin images. The activation function used is the tan sigmoid function, for both the hidden and the output layer. The input to the neural network is the feature vector containing 10 components, the neural network classifier structure consists of Input layer, Hidden layer and Output layer. The hidden and output layer adjusts weights value based on the error output in classification. The output of the network is compared with desired output. If both do not match, then an error signal is generated. This error is propagated backwards and weights are adjusted so as to reduce the error. The modification of the weights is according to the gradient of the error curve, which points in the direction to the local minimum. In BPN, weights are initialized

Table (1): Statistical Features Equations

Statistical	Mathematical Formula
Mean	$m = \sum_{i=0}^{K-1} r_i g(r_i)$
Stander Deviation	$\mu_n(r) = \sum_{k=0}^{K-1} (r_i - m)^n g(r_i)$
Perimeter	$T = \sum_{i=1}^{L} d_i = \sum_{j=1}^{L} \lvert X_i - X_{i+1} \rvert$
Area	$M_{KL} = \sum_{i=1}^{K} \sum_{j=1}^{L} i^k j^l A(i,j)$
Centroid	$j_c = \frac{\sum_i \sum_j j \times A_{i,j}}{\sum_i \sum_j A_{i,j}}$ ، $i_c = \frac{\sum_i \sum_j j \times A_{i,j}}{\sum_i \sum_j A_{i,j}}$
Equiv.diameter	$D = max_{X_k, X_l \in R}\, d(X_k, X_l)$
Euler	$E = C - H$
Roundness	$\lvert k(t) \rvert^2 \triangleq \left(\frac{d^2 x}{dt^2}\right) + \left(\frac{d^2 y}{dt^2}\right)^2$
B Box	$y\ max \quad xmax \quad ymin \quad x\ min$
Entropy	$E = \sum_{i=0}^{L-1} r(i) \log g(r_i)$

randomly at the beginning of training. There will be a desired output, for which the training is done. Supervisory learning is used here. The aim of this network is to train the net to achieve a balance between the ability to respond correctly to the input patterns that are used for training [10]. During forward pass of the signal, according to the initial weights and activation function used, the network gives an output. That output is compared with desired output. If both are not same, an error occurs.

Error = Desired Output - Actual Output

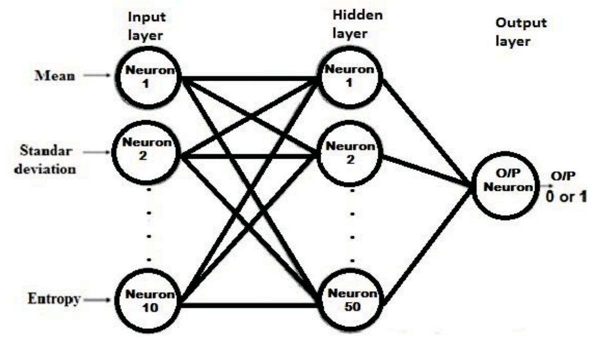

Figure 2: The Neural Network Structure.

5. Results and Experiments

In this section a detailed experimental skin image Recognition has been presented. We have used Data base contain (50 image for satisfactory skin cancer, 50 image for unsatisfactory skin), other images obtained from internet (50 image for satisfactory skin cancer, 50 image for unsatisfactory skin).

Testing stage consists of 80 images (20 image for satisfactory skin cancer, 20 image for unsatisfactory skin cancer) from in Al-Seder Hospital and (20 image for satisfactory skin cancer, 20 image for unsatisfactory skin cancer) from internet.

Figure (2) show the sample of Sick skin images while figure (3) show the sample of intact skin images testing for one person in this paper.

The next stage is feature extraction concerns finding for images. To be able to recognize Sick skin images or intact skin images testing for one person in automatically. In feature extraction, we generally seek invariance properties so that the extraction process does not vary according to chosen (or specified) conditions. Features are sensitive to clutter and occlusion. As a result it is either assumed that an image only contains a single object, or that a good segmentation of the object from the background is available[4].

Table 2: Statistical features for image 1, image 2 and image 3 in sick skin images and intact skin images.

no.	Statistical	Image -1-		Image -2-		Image -3-	
		Intact	Sick	Intact	Sick	Intact	**Sick**
1	Mean	145.205	134.332	130.310	133.478	149.894	**130.116**
2	Stander Deviation	21.675	19.999	20.3604	39.486	17.728	**31.328**
3	Perimeter	0	4	0	0	6	**6.828**
4	Area	1	4	1	1	6	**5**
5	Centroid	8 164	12.500 125.500	90 19	10 102	62.000 30.500	**1.200** **41.400**
6	Equiv.diameter	1.128	2.256	1.1284	1.1284	2.764	**2.523**
7	Euler	1	1	1	1	1	**1**
8	Roundness	Inf	3.1416	Inf	inf	2.0944	**1.3475**
9	B Box	7.500 163.500 1.000 1.000	11.500 124.500 2.000 2.000	89.5000 18.5000 1.0000 1.0000	9.500 101.500 1.000 1.000	60.500 29.500 3.000 2.000	**0.500** **39.500** **2.000** **4.000**
10	Entropy	6.451	6.191	6.0238	7.149	5.9954	**6.926**

Table 3: Statistical features for image 4, image 5 and image 6 in sick skin images and intact skin images.

no.	Statistical	Image -**4**-		Image -**5**-		Image -**6**-	
		Intact	Sick	Intact	Sick	Intact	Sick
1	Mean	151.507	134.852	144.851	144.379	156.216	138.080
2	Stander Deviation	56.4351	44.8704	21.391	37.924	25.748	34.923
3	Perimeter	4	95.1127	2	0	4	13.656
4	Area	4	453	2	1	3	19
5	Centroid	127.500 38.5000	90.4680 9.8631	40.500 133.000	44 40	198 174	63.210 44.947
6	Equiv.diameter	2.2568	24.0162	1.595	1.128	1.954	4.918
7	Euler	1	1	1	1	1	1
8	Roundness	3.1416	0.6293	6.283	Inf	2.356	1.280
9	B Box	126.500 37.5000 2.0000 2.0000	73.5000 0.5000 30.0000 25.0000	39.500 132.500 2.000 1.000	43.500 39.500 1.000 1.000	196.500 173.5003.0 00 1.000	60.500 42.500 5.000 5.000
10	Entropy	7.0156	7.3504	6.4235	6.8462	6.5226	6.9203

Figure (3) : sample of Sick skin images

In this research was used back propagation neural network and that the results of accurate and efficient in image verification and distinctiveness . Based network in its work on the values of the Statistical features of the image. Where the network receives mono a matrix include 10 values are the results of the Statistical features of the image . To the output for neural network verification image if Sick skin images or Intact skin image.

Figure (4): sample of intact skin images

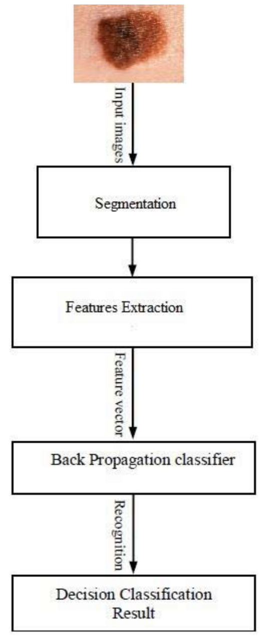

Figure (5) :Diagram for our method

Mean square error performance function (MSE) and Mean absolute error performance function (MAE) to find out the amount of divergence in between them using Elman neural network and which is defined as discrimination and signature and identify the person concerned.

phase begins training the network where they are taking the values of the results of the features of the input of the network where the network is trained on error rate (0.001) and the number of cycles of (1000) cycle to reach the desired goal concept of used Mean square error performance function (MSE) and Mean absolute error performance function(MAE) to find out the amount of divergence in between them using neural network and which is defined as discrimination and image and identify the person concerned.

Table 4 MSE and MAE for Intact skin images

No. of image	MSE	MAE
1	2.2589e-021	1.9670e-011
2	3.5296e-021	2.4648e-011
3	6.9190e-021	3.4949e-011

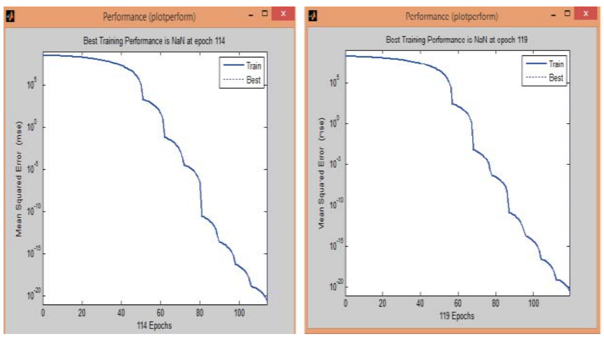

Figure 6 performance NN effects for Intact skin image(1 and 2).

Table 5 MSE and MAE for Sick skin images

No. of image	MSE	MAE
1	2.8594e-021	2.2389e-011
2	1.9650e-022	1.1833e-011
3	1.7299e-021	1.7512e-011

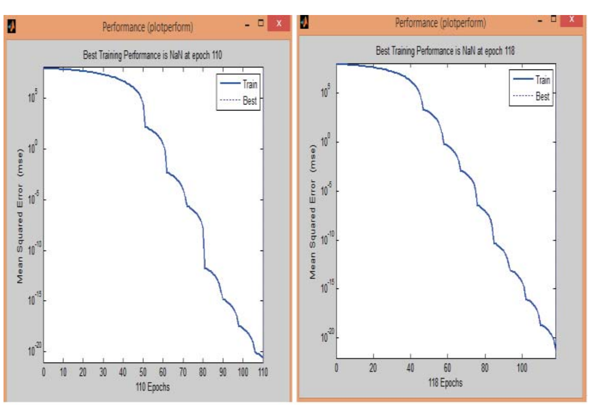

Figure 7: performance Neural Network effects for sick skin image(image 1 and image 2).

Some of the suggestions of artificial neural network used in MATLAB:-

net.trainFcn = 'trainlm'; for training function
net.trainParam.epochs = 1000; for max number of iterations
net.trainParam.lr = 0.05; for the learning rate
net.performFcn1 = 'mse'; Mean square error performance function(MSE) net.performFcn2 = 'mae'; Mean absolute error performance function (MAE)
net.divideFcn = 'dividerand'; how to divide data

[net,tr] = train(net, input, target); for training

5. Conclusion

When the technique of neural network was applied on Data base contain sick skin images and Intact skin images, the fowling remarks can be considered in this paper:

1 - We applied ten statistical parameters as input of ANN. After training, five of them distinguishes the type of test image(sick or intact).

2- In sick skin image Mean square error performance function(MSE) and Mean absolute error performance function(MAE) are Convergent values while in Intact skin image are spaced.

3-Tabel 6 showed the final results for greater and smaller Statistical features in sick skin images and Intact skin images.

Table 6: Statistical Criteria results in paper

No.	Statistical Criteria	Sick Image
1	Mean	Greater
2	Stander Deviation	Greater
3	Perimeter	Variable
4	Area	Less
5	Centroid	Variable
6	Equivalent diameter	Greater
7	Euler	No change
8	Roundness	Variable
9	B Box	Variable
10	Entropy	Greater

References

[1]Stephen Gould, Tianshi Gao and Daphne Koller," Region-based Segmentation and Object Detection", Advances in Neural Information Processing Systems 22 (NIPS 2009), Stanford University, {sgould,tianshig,koller}@cs.stanford.edu

[2] M.J. Swain, D.H. Ballard, Color indexing, Int. J. Computer. Vision 7(1) (1991) 11—32.

[3] Ms Jyoti C Chaudhari ,"Design of artificial back propagation neural network for drug pattern recognition", International Journal on Computer Science and Engineering (IJCSE),2010.

[4] J. Jiang, P. Trundle, J. Ren, "Medical image analysis with artificial neural networks", Computerized Medical Imaging and Graphics (34), 2010, pp. 617–63.

[5] Gonzalez, R.C. and R.E. Woods, “Digital Image Processing” 1992, Reading, Massachusetts: Addison-Wesley.

[6] ANM Enamul Huque ,Shape Analysis and Measurement for the HeLa cell classification of cultured cells in high throughput screening, School of Humanities & Informatics University of Skövde, Sweden,2006.

[7] R. Haralick, K. Shanmugam, and I. Dinstein “Textural Features for Image Classification”, IEEE Trans. on Systems, Man and Cybernetics, SMC–3(6):pp 610–621, , 1973.

[8] Biswajit Pathak, Debajyoti Barooah, "Texture analysis based on the gray-level co-occurrence matrix considering possible orientations", International Journal of Advanced Research in Electrical, Electronics and Instrumentation Engineering, Vol. 2, Issue 9, 2013.

[9] Dhanashree gadkari, “ Image Quality analysis using GLCM“,Master of Science in Modeling and Simulation in the College of Arts and Sciences, University of Central Florida Orlando, Florida,2000.

[10] Sarika Choudhari, Seema Biday, "Artificial Neural Network for Skin Cancer Detection", *International Journal of Emerging Trends & Technology in Computer Science (IJETTCS),* Volume 3, Issue 5, September-October 2014

[11]Andrius Ušinskas, Romualdas A. Dobrovolskis And Bernd F. Tomandl,2004," Ischemic Stroke Segmentation on CT Images Using Joint Features",Institute of Mathematics and Informatics, Vilnius, INFORMATICA, 2004, Vol. 15, No. 2, 283–290

[12]Fei Gao, 2005,"An Efficient Approach To Automated Segmentation In Medical Image Analysis", Requirements for the Degree of Master Of Science In Electrical Engineering, Submitted to the Graduate Faculty of Texas Tech University.

[13]Huajun Ying, Ming Zhang, Jyh-Charn Liu, 2007, "Fractal-based Automatic Localization and Segmentation of Optic Disc in Retinal Images", Department of Computer Science, Texas A&M University College Station, TX, USA,

[20] Ahmed Sami,2014,"Comparison Recognition of some Bones Diseases By Neural Networks with Image Processing Technology and Neural Networks with Wavelet Transform"", Requirements for the Degree of Master Of Science In Physics, Submitted to the Council of Education College of AL-Mustansiriyah University

SESSION

POSTER PAPERS

Chair(s)

TBA

Structural Model of Eidetic Memory

Irina Samoylo [1*], Dmitry Zhukov [2], James William Brooks[3] and Victoria Hodges[4]

[1*] Irina Samoylo, PhD – I.M. Sechenov First Moscow State Medical University, Professor, Address: 40 Vostochnaya Street, Apt 23, Dolgoprudniy, Moscow Reg., Russia

[2] Dmitry Zhukov, Director of the Institute of Information Technologies, Moscow State University of Information Technologies, Radio Engineering and Electronics (MIREA), Address: 78, Vernadskogo Prospect, Moscow, Russia

[3] James William Brooks – Salem International University, Consultant, Address: 7138 Dolphin St. West, Sugarloaf Key, FL, 33042, USA

[4] Victoria Hodges – I.M. Sechenov First Moscow State Medical University, Consultant, Address: 361 Fairview Rd., Westbrook, CT, 06498, USA

Abstract: *The purpose of this research is to introduce a model of an eidetic memory. The structure of the model is based on the curved tubes of memory, which are formed during the training of a multilayer and multiply connected neural network. This model has capacity to process simultaneously a large number of the input images of different objects. The eidetic memory is characterized by its plasticity, stability, and distributed structural biochemical nature. Research of the mechanisms of the eidetic memory has an enormous potential in education, health services, and other areas. The application of the developed training technics and approaches resulted from the research will simplify the process of memorization of complicated information without any need in multiple repetitions or cramming.*

Keywords: memory, imagery, neural networks, modeling, mathematics

1 Introduction

An accidentally thrown word, some smell, or taste, at times, can give rise to the whole range of feelings or bright images in a person's mind. That person can clearly see some objects, smell them or hear sounds that vanished a while ago. This clearly indicates that the eidetic memory mechanisms started to work in the person's mind. The study of the laws of an eidetic memory reveals enormous opportunities for its application in teaching and training because this type of memory is formed instantly and does not require multiple repetitions to consolidate the new incoming information.

Multiple world researchers were able to make a significant progress in the memory modelling based on artificial neural networks, after they established the models' structure and functioning as close as possible to the biological neural networks of the cerebral cortex. Hence, to insure the effective work of the created models, the perception of the information must meet two basic requirements [1]:

1. Plasticity, i.e. it should be able to adapt to any new information, and
2. It should not destroy the memory of the old images.

2 Topology and work of a multilayered and multiple coherence resonant network

Based on the biological structure of the cerebral cortex, we can state that the topology of a real biological neural network may be similar to the multilayered and multiple coherence resonant network (MMRS) [2]. This network can be formed of a plurality of inhibitory and excitatory neurons, which are hierarchically interconnected both vertically and horizontally (see Fig. 1). The neurons in their turn form vertical and horizontal conditional planes.

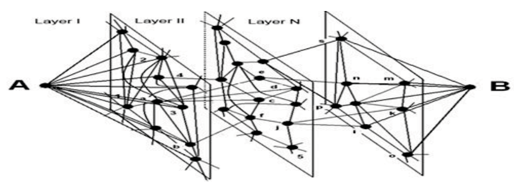

Fig. 1. Topological structure of a multilayered and multiple coherence resonant neural network

The network function must ensure the memory plasticity on one hand and its stability on the other hand. Let us consider how this can be implemented by using the structure shown in Figure1. The network self-adjustment takes place at the recognition of the input images. Only the most excited and experienced neurons must be trained in a given area of each layer. At the input of the first training image, the chain of the interconnected and strongly excited neurons (see fig. 2A) must be formed in the network shown in Figure 1. It passes through all neuronal layers from the entry point A to the output point B (see Fig. 1). An increase in strength of excitation of the already excited neurons in the chain can take place at the input of the next training image, which leads to the increase in the strength of the neurons and to the connection to the chain of the new highly excited neurons (see Fig. 2B and 2C). The structure of the type shown in Fig. 2C, that was formed after the training in the network shown in Figure 1, can be represented as a conventional curved tube (see Fig. 3).

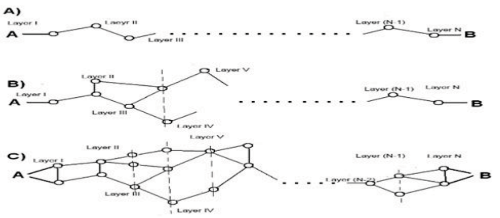

Fig. 2. Formation of the structures of highly excited neurons at training of a multilayered and multiple coherent resonant neural network

This tube is the entry area associated with the entry point A (the left end) and the exit area (the right end), associated with the exit point B. When a new image is introduced to a trainee, the following process can happen. If a chain of highly excited neurons passes from the entrance area to the exit area within any of the previously formed curved tubes, then the input image is identified as a related to a certain earlier presented image and therefore at this point, it is recognized as a familiar to the trainee object (the resonance effect occurs).

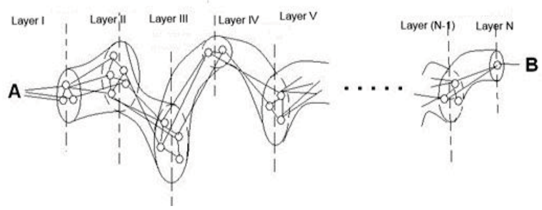

Fig. 3. Graphic representation of the curved tube of the memory, formed during training of a multilayered and multiple coherent resonant neural network

If the chain of strongly excited neurons, which appeared after the new image input, does not pass or passes partially through the previously formed curved tube, then in the network shown in Figure 1, the formation of a new tube begins, in accordance with the model shown in Figure 2. In the above case, the adaptation process to the new input information takes place. It is characterized as the plasticity of memory. The formation of the recognition structures (automatic recognition) is possible after the conducted training that was based on the introduction of multiple sets of different image samples. The new formed structures will look like those shown in Figure 4. The curved memory tubes (M-1) and M overlap partly (in layers IV and V) see Fig. 4. However, they will relay to different classes of images. With significantly similar combinations of the curved memory tubes, the excitation of the chain of neurons at the recognition of the input images (the appearance of resonance) will result in the excitation of the neurons in another chain. Therefore, the resonating ensemble of the interacting curved memory tubes is formed. Supposedly, a similar mechanism of information perception and recognition arises in real biological structures when an eidetic memory activates, after which some images evoke the appearance of different objects, smells, etc. in the human brain. Synesthesia is the foundation of the eidetic memory phenomenon. It is a combined, synchronized sensation. In fact, this phenomenon is described as followed: any stimulus of a certain sense organ causes aside from a person's will, a particular feeling and, at the same time, it trigs additional sensations.

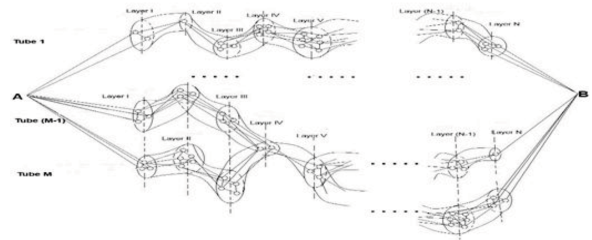

Fig. 4. Graphic representation of the recognition structures (the automatic recognition) and multilayered, multiple coherent resonant neural network

The authors of this paper have an intention to further study the phenomenon of an eidetic memory by performing diverse tests of the described above eidetic memory model, which will involve the eidetics participation. Eidetics are those people who are able to recall images with unusual vividness and detailing. Either they possess a very well developed eidetic memory by birth or they obtained after the training (for example, after taking a speed-reading course). At the first phase of the experiment, it is expected to identify the areas of the white matter, which would serve as the marker of the expressed eidetic memory in the eidetics. The Diffusion Tensor Imaging (DTI) will be used as an instrument. At a later stage, it is planned to establish the functional connections between the areas of the white matter, using the Functional Magnetic Resonance Imaging (fMRI).

3 Conclusions

The proposed model of an eidetic memory possesses the ability to process simultaneously a large number of the input images due to the presence of the plurality of the curved tubes in training. It is characterized by both plasticity and stability, as well as by a distributed structural biochemical character.

This model is recommended for implementation in the theory of teaching and training, development and application of learning technics and in the field of artificial intelligence systems.

4 References

[1] S. Rose. "The Memory Device. From Molecules To Consciousness Lane". Translated from English - M: World, 1995.

[2] S. Ja. Berkovich. "Cellular Automatic Machines, As a Reality Model: the Search For the New Concepts of Physical and Information Processes" - M: Moscow University, 1993

A Stable Digital Blood Pressure Measurement Method

Boyeon Kim[1] and Yunseok Chang[2]
[1]Department of Computer Engineering, Daejin University, Pocheon, Korea
[2]Department of Computer Engineering, Daejin University, Pocheon, Korea

Abstract – *This work contains a stable method for non-invasive and non-Kortokoff type blood pressure measurement method using the digital sensor unit without air pressure cuff. In this work, we designed and implemented a digital wireless blood pressure measurement system includes digital air-pressure sensor unit, Bluetooth communication network, and smartphone app that can handle the arterial pulse waveform into the blood pressure and pulse count. To get the exact blood pressure, we have to maintain a stable initial sensor pressure over the skin on blood vessel. Since it is very hard to sustain the initial sensor pressure all over the measurement process, we made a sort of adoptable smartphone app that can compensate the measurement result against the initial sensor pressure variation instead of all pressure stabilizing efforts at every trial. With this smartphone app, we can maintain the stability of measurement result without any additional mechanism or process to sustain the initial sensor pressure variation in an easy way*

Keywords: Digital blood pressure measurement, Initial sensor pressure variation, Measurement stability, Arterial pulse, Smartphone app

"Extended abstract/Poster paper"

1 Introduction

Most of the existing commercial tonometer has been designed and implemented with air pressure cuff based on the traditional Kortokoff method or oscillometric method. But traditional methods have to block off the artery with high air pressure, they cannot be applied on the continuous blood pressure measurement [1]. Thus, although most of the digital electronics tonometer still designed based on the oscillometric method, some recent researches are focusing on the non-invasive and non-Kortokoff type digital blood pressure measurement method. Since there is no air pressure or no cuff to oppress the artery in non-Kortokoff method, digital air pressure sensor has to check out the blood pressure outside the artery or blood vessel [2]. The digital air pressure sensor contacts to the skin on the blood vessel, it is very important to maintain the initial sensor pressure constantly not to be varied during all over the measurement process, and in many cases, we need some additional mechanism to maintain the initial sensor pressure constantly against the initial sensor process variation. But in this work, we implemented the digital blood pressure measurement system just with the software technology that can compensate the initial sensor pressure variation without any additional mechanism or circuit.

2 Measurement environment

2.1 Arterial pulse measurement system

In this work, we designed and implemented the digital blood pressure measurement system as shown in Figure 1. The measurement system is composed of wrist-banded digital arterial pulse sensor unit and digital arterial pulse measurement app on smart phone. The wrist-banded sensor unit includes air pressure sensor, DSP processor, battery, and Bluetooth communication unit. The measurement app produces blood pressure by using blood pressure estimation algorithm and can run any Android OS based smartphone supports BT 2.1+EDR [3].

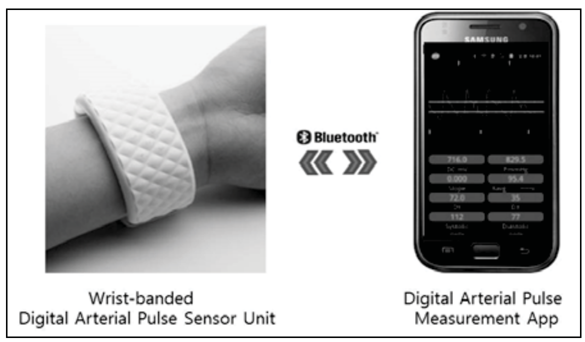

Figure 1 implemented arterial pulse measurement system

Blood pressure estimation algorithm is the key feature of the digital blood pressure measurement system. The app estimates the systolic pressure and the diastolic pressure by using BP (Blood Pressure) relation function and differential value of the arterial pulse waveform.

2.2 Differential value and BP relation function

To estimate the blood pressure with the digital blood pressure measurement system, the smart phone app includes blood pressure estimation algorithm based on the BP relation function that is a sort of 1st order linear function of blood pressure values from the commercial tonometer for the differential values of the arterial pulse waveform from the digital measurement system. To estimate exact blood pressure, all the differential values of the waveform should be measured under the same initial sensor pressure. Therefore, we have to compensate the pressure variation of the initial sensor pressure during all over the measurement process.

3 Digital compensation against the ee variation

3.1 Digital compensation method

To compensate the variation of the initial sensor pressure ΔP_{init}, the digital sensor unit should send the current air pressure value P_{air} to the smart phone app. Therefore, the blood pressure estimation algorithm also should be modified to reflect the variation as a differential value ΔP_{diff} on the *k*th differential value ΔP_k of the waveform W instantly as follows:

$$\Delta P_{diff} = \Delta P_k - (\Delta P_{init} - P_{air}),\ \Delta P_{avg} = avg(\sum \Delta P_{diff}) \quad (1)$$
$$Systolic\ (\Delta P) = Reg(Systolic_{avg}, \Delta P_{avg}) \quad (2)$$
$$Diastolic\ (\Delta P) = Reg(Diastolic_{avg}, \Delta P_{avg}) \quad (3)$$

3.2 Digital compensation against the variation

The digital pressure compensation method is embedded in the smart phone app. This app originally designed to performs the Bluetooth connection with digital sensor unit and blood pressure estimation corresponds to the differential value. In this work, we implemented the current air pressure value P_{air} as PmmHG, and modified the blood pressure estimation program to compensate it for the estimated blood pressure. Figure 2 shows the P_{air} at every 8 peaks interval as toast message.

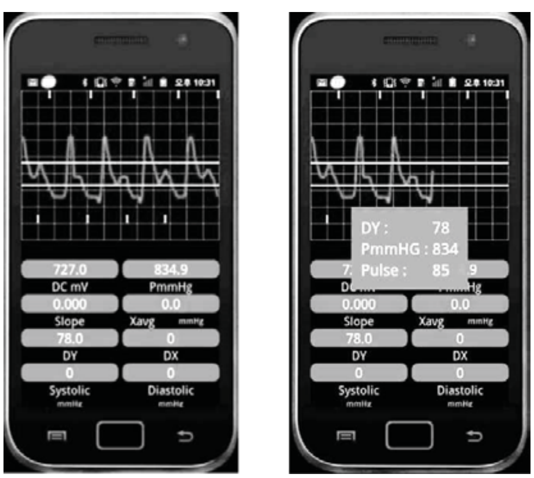

Figure 2 Digital pressure compensation app

The PmmHG value on the toast message in Figure 2 shows the current air pressure P_{air} on the blood vessel. The smart phone app reflects the P_{air} to calculate the ΔP_{diff} and ΔP_{avg}, and finally estimates the systolic pressure and diastolic pressure by using function (1), (2), (3) and BP relation function. Table 1 shows the results of accuracy enhancement before and after the digital compensation. In this experiment, 54 volunteers participated include 11 hypertensives, 32 normal persons, and 11 hypotension patients. As the results of experiment shows the digital compensation method can enhance the precision of the blood pressure estimation.

Table 1 Accuracy enhancement of the digital compensation

	Before compensation		After compensation	
	Systolic	Diastolic	Systolic	Diastolic
Hypertension	93.1%	86.3%	95.7%	88.8%
Normal	91.4%	85.5%	94.3%	90.4%
Hypotension	84.3%	64.4%	87.8%	71.9%

4 Current situation and further works

To stabilize the initial sensor pressure against the pressure variation, we need many mechanical parts in the measurement system. But in this work, we had compensated the digital sensor pressure for estimated systolic pressure while the smart phone app of the measurement system estimates the blood pressure. In the experimental environment, we are finding out that the digital compensation method can help enhancing the accuracy and stability of systolic pressure estimation process. At further work, we will advance the digital compensation process of the smart phone app in detail and make the BP relation equation more precisely to get higher blood pressure estimation accuracy.

5 Acknowledgement

This work was supported by the National Research Foundation of Korea(NRF) grant funded by the Korea government(MEST)(No. NRF-2015R1D1A1A01057703)

6 References

[1] Bryan. Williams. "Achieving Blood Pressure Control in Clinical Practice"; Journal of the American Society of Hypertension, Vol. 2 No. 4, 10-15, Aug 2008.

[2] Myung Cheon. Ahn, Jong Gu Choi, Il Ho Son, Sang Seok Lee and Keun Ho Kim. “Estimated Blood Pressure Algorithm of Wrist Wearable Pulsimeter using by Hall Device”; Journal of the Korean Magnetics Society, Vol. 20 No. 3, 106-113, Jun 2010.

[3] Boyeon Kim, Wenhai Jin, Sung Hoon Woo and Yunseok Chang. “A New Approach on Digital Blood Pressure Measurement Method for u-Healthcare Systems”; International Journal of Bio-Science and Bio-Technology, Vol. 7, No. 1, 169-178, Jan 2015.

Flexible dry electrodes made from CNT/Textile Paint Composite for ECG sensor

Jaehyo Jung, Siho Shin, Seokeun Park and Youn Tae Kim[+]
IT Fusion Technology Research Center, Chosun University, Gwangju, Korea
[+]petruskim@chosun.ac.kr

***Abstract*— An electrode, which uses a composite of Carbon Nano Tube (CNT) and textile paint and which can be printed on a cloth (fabric), was fabricated in this research. The electrode was printed on a cloth, and compared with the existing Ag/AgCl electrodes based on an experiment that detects ECG signals. Research on the effects of various factors such as the cleanliness, physical shock, and frequency of use of the electrode is ongoing. In addition, based on this research, we expect to develop a U-healthcare system that would make it possible to consistently detect bio-signals in daily life.**

Keywords— Carbon Nano Tube(CNT), Electrodes, Electrocardiography(ECG), Textile Paint, U-healthcare

Type of the Submission – Extended Abstract/Poster Paper

I. INTRODUCTION

Because of the improvements in information technology and diagnostic techniques, and the changes in living environments, the development and demand for U-healthcare systems is growing steadily [1]. Such systems monitor bio-signals to identify abnormal statuses and prevent diseases, and are used in various fields such as sports, medicine, and healthcare. To measure the bio-signals, electrodes that are connected to the measuring instrument are needed. Wet and dry electrodes are mainly used for this purpose [2]. However, these electrodes have several disadvantages; it is difficult to attach and detach these electrodes (used for measuring the signal) from the body, and the user may suffer an allergic reactions or some other trouble in case of long-term use of these electrodes [3]. To solve these problems, we studied the fabrication of electrodes that use a composite of CNT and textile paint and can be printed on cloth. The performance of these electrodes was evaluated by measuring ECG signals. This helps in the development and study of portable U-healthcare devices, which continuously monitor the bio-signals without causing dermatological problems or discomfort.

II. ELECTRODE DESIGN

An electrode was fabricated to measure the ECG signal in the main study. We printed the electrode on fabric for measuring the ECG signal, as shown in Figure 1.

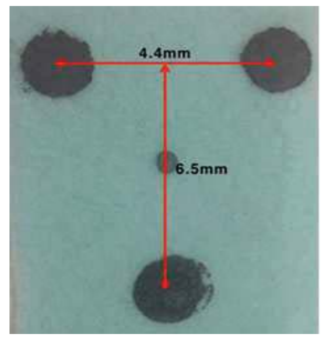

Fig.1 Screen Printed dry electrode

Textile paint (ShieldColor Corp.) and MWNT (multiwall Carbon Nanotube, WorldTube Corp., CNT-3.0 wt.%) were mixed using an agitator for 30 min. The electrode was manufactured by dehydrating this mixture for 3h, after printing on the fabric using a frame. The electrodes, which would be used as the +, -, and Right Leg Driver (RLD) were connected to the ECG module through conductive wires.

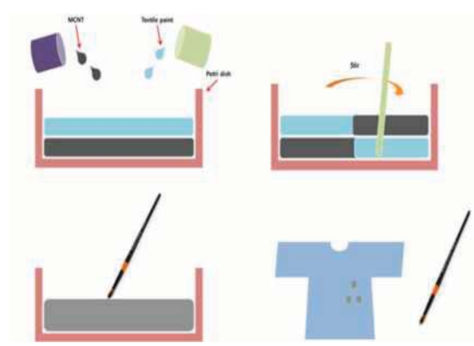

Fig. 2 Dry Electrode Fabrication

III. RESULT AND DISCUSSION

In this research, we measured the ECG signals using the existing Ag/AgCl electrode and the proposed composite CNT electrodes. Because the impedance of the composite CNT electrode is slightly higher than that of the Ag/AgCl electrode, the maximum voltages of the signals measured using the CNT and Ag/AgCl electrodes were 3 V and 3.5 V, respectively. Although the voltage of the signal measured using the CNT electrode was 0.5 V lower than that using the Ag/AgCl electrode, it was possible to measure the ECG signal accurately without distortion.

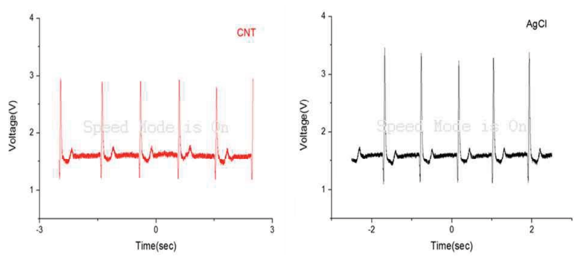

Fig. 3 ECG signal measurement using the proposed dry electrode (left) and wet Ag/AgCl electrode (right)

Because these electrodes can be printed or drawn on fibrous clothes, they can be applied in various fields such as wearable devices. The printing of the electrode on fabric enables the monitoring of body movements and bio-signals, and these electrodes are expected to replace existing ones. In addition, bio-signal detectors such as Holter systems using wearable electrodes can provide the user with a comfortable fit during long-term use of the sensing device [4]. Because continuous ECG monitoring is quite important in cardiovascular patients, research and development in the field of wearable electrodes would be more or less continuous [5].

IV. Conclusion

In this research, an electrode using a composite of CNT and textile paint was developed for detecting bio-signals. Comparative experiments were conducted with the common wet electrodes. An exact ECG signal was measured using the developed electrode, and it was not significantly different from that measured using the Ag/AgCl electrode (except for the amplitude). However, this electrode has a few unsolved issues such as signal reduction because of higher impedance, reduced durability against external damage or washing, and absence of an efficient method for the transmission of the electrical signal to the circuit. If these problems are solved completely, various bio-signal detectors that are simple and comfortable to use can be developed.

Acknowledgment

This research was supported by the MSIP(Ministry of Science, ICT and Future Planning), Korea, under the ITRC(Information Technology Research Center) support program (IITP-2015-R0992-15-1021) supervised by the IITP(Institute for Information & communications Technology Promotion).

References

[1] J Jung, J Lee, J Lee and YT Kim, “Development of Service network for Wearable type Acute Myocardial Infarction Diagnosis System” , IEEE Sensors conference 2013, 3 November 2013, pp. 1200-1203

[2] H. P. Xu, X. Tao Zhang, “Textile-structured electrodes for electrocardiogram” ,Textile Progress, 2008, pp.183–213.

[3] D Pani, A Dessi, E Gusai, JF Saenz, G Barabino, and A Bonfiglio, “Evaluation of Novel Textile Electrodes for ECG Signals Monitoring Based on PEDOT:PSS-Treated Woven Fabrics”, Engineering in Medincine and Biology Society(EMBC), 2015, pp. 3197-3200

[4] McAdams, E., Krupaviciute, A., Gehin, C., Grenier, E., ea al., “Wearable sensor systems: The challenges” In Engineering in Medicine and Biology Society(EMBC), August *2011* pp. 3648-3651

[5] McAdams, Eric, et al. "Wearable electronic systems: Applications to medical diagnostics/monitoring." Wearable Monitoring Systems. Springer US, 2011. Pp.179-203

Regional changes in left ventricle myocardial compliance in pig model of ischemic cardiomyopathy

N. Popovic[1], R. Driesen[2], C. Kadur Nagaraju[2], P. Claus[1]
KU Leuven, Department of Cardiovascular Sciences, Belgium
[1]Division of Cardiovascular Imaging and Dynamics
[2]Division of Experimental Cardiology

Abstract— *Left ventricle (LV) remains the most researched cardiac chamber in terms of passive mechanical characterization, however data in pathological cases is still sparse. In this study, we examine passive mechanical behavior of LV wall in pigs, in a healthy state and six weeks after the copper-coated stent implantation. This procedure has resulted in mild myocardial infarction of 10% of the LV mass. We have investigated passive mechanical behavior of the scar region as well as remote and adjacent regions in pigs that have undergone this procedure, and corresponding regions in the healthy animals. Tissue characteristics were investigated using the bi-axial tensile testing framework. We have found significant differences in tissue compliance between scared tissue and other regions, but no difference between remote and adjacent regions.*

Keywords: *Ischemic cardiomyopathy, Constitutive modeling, Tissue Mechanics*

1. Introduction

Ischemic cardiomyopathy (IC) is a condition that is strongly associated with a weaken hart muscle, and is usually a result of a myocardial infarction (MI) or an artery narrowing. Post MI, heart goes through different remodeling phases, first of which is largely mechanical. MI has been shown to have a great impact on local myocardial structure remodeling. Structural cardiac remodeling inevitably leads to mechanical remodeling. Studying of mechanical remodeling can significantly increase our predictive capabilities related to the IC.

There have been multiple attempts on passive mechanical characterization on the LV wall over the years [1], both in healthy and various pathological states. Still, to this day there has been little interest in identifying mechanical changes among different regions of LV. In this report, we will focus on LV regional myocardial compliance investigation. Besides scar region, we will investigate if the remodeling effects are detectable in the adjacent and remote regions,and we will compare these results to the analogous regions in the healthy LV, anterior and posterior.

2. Methodology

2.1 Animal Model

Previously developed pig model of IC [2] was used. Copper-coated stents were implanted into the left anterior descending coronary artery of porcine hearts in eight animals, and results were compared to the nine sham animals. Stent implantation has led to MI of 10% of the LV mass.

2.2 Bi-axial testing

Animals were sacrificed 6 weeks post stent implantation. Agar embedded tissue blocks were sliced into $3 \pm 0.84mm$ thick slices, with constant $x \times y$ dimensions of $7.7 \times 7.7mm$. Mechanical tissue characterization was performed with a bi-axial tissue tester (BioTester 5000, CellScale Biomaterials Testing, Waterloo, Canada), using two $2.5N$ load cells of $25mN$ precision. Five different loading protocols were used in testing (with $X : Y$ axis force ratios of $1:1$, $1:.75$, $1:.5$, $.75:1$, $.5:1$) with maximal tensile pressure set to $20kPa$. Stress strain data were collected based of optical following of four markers placed in the central part of the specimen. Data were analyzed based on the standard procedure, described in [3].

3. Results

3.1 Areal strain

Normalized maximal areal strain is given as $\Omega_{nr} = (\lambda_1\lambda_2 - 1)/h$, where λ_i is the maximal principal strain in x and y directions, and h is sample thickness. Figure 1 shows the distributions of the values of normalized areal strain in the different areas of the LV in both groups of animals. We have found no significant difference between areal strains when comparing adjacent and remote regions in IC animals, nor between anterior and posterior regions in sham animals. However, scar tissue shows to be significantly stiffer than other regions.

3.2 Constitutive modeling

Two main groups of constitutive models are phenomenological and micro-structural. Micro-structural models have shown to be very useful in the characterization of the healthy cardiac tissue. The healthy LV is composed of

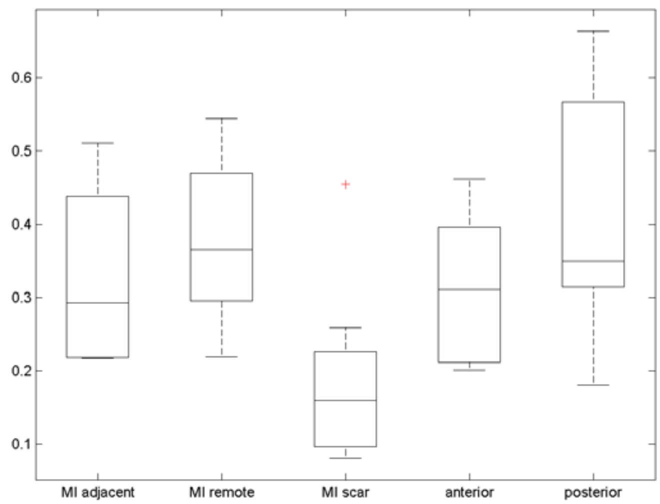

Fig. 1: Normalized maximal strain strain per region

parallel myofiber sheets. Myofibers form a helical warp across the LV. Fiber angle change over the cardiac wall is approximately 100° [4]. LV tissue that has been affected by cardiac injury usually responds with structural remodeling. This remodeling limits application of the micro-structural models. Therefore we, will focus on to the phenomenological models.

We fitted the experimental data to the well known Fung-type model [5], where strain density function is defined with (1). Fitted parameters are given in the table 1. Based on these parameters, we have generated the general stress train response per region, as shown in the figure 2, where we can clearly see that scar region reaches the targeted Cauchy stress of $20kPa$ at lower strain, when compared to the other regions.

$$W(Q) = \frac{1}{2}C_F(e^Q - 1) \quad (1)$$

$$Q = b_1E_{11}^2 + b_2E_{22}^2 + 2b_4E_{11}E_{22} \quad (2)$$

$$S_{11} = C_Fe^Q(b_1E_{11} + b_4E_{22}) \quad (3)$$

$$S_{22} = C_Fe^Q(b_2E_{22} + b_4E_{11}) \quad (4)$$

	C_F	b_1	b_2	b_4	R^2
MI adjacent	5,73	9,45	6,57	0,75	0,98
MI remote	4,91	8,86	6,45	0,50	0,98
MI scar	7,71	9,49	9,99	5,13	0,98
Anterior	6,52	6,74	6,30	0,34	0,97
Posterior	7,08	6,17	5,29	0,18	0,97

Table 1: Fitted Fung-type material parameters

4. Conclusion

We have used the pig model of IC, where we have implanted a copper-coated stent in the left anterior descending coronary artery of porcine hearts. Eight animals have undergone this procedure, and results were compared to nine sham animals. This procedure has resulted in the moderate MI, measured to be 10% of the LV mass. We have investigated the changes in the passive mechanical properties of the porcine LV wall between these two groups. Three regions were identified in the IC animals: adjacent, remote and scar, and two regions in the sham group: anterior and posterior. We have found a significant decrease in myocardial compliance of the scar region compared to the other regions, but we found no significant difference when comparing adjacent and remote region, nor between corresponding regions between two groups of animals.

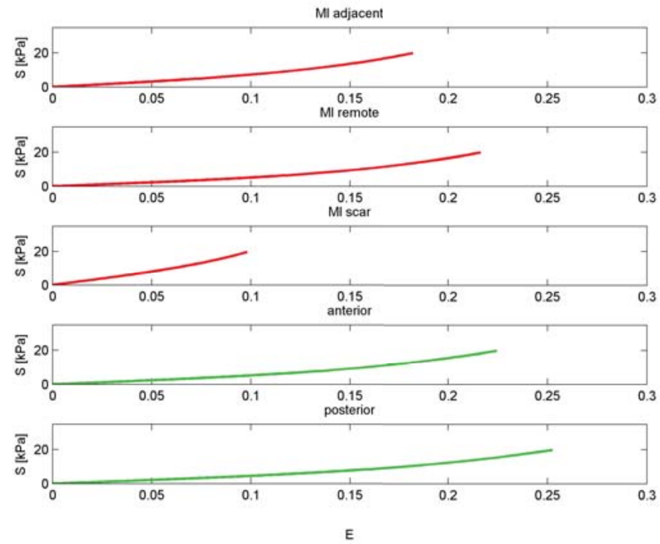

Fig. 2: Generated second Piola-Kirchhoff stress versus Green Lagrange strain response based on Fung-type model fitting

References

[1] G. Sommer, M. Eder, L. Kovacs, H. Pathak, L. Bonitz, C. Mueller, P. Regitnig, and G. a. Holzapfel, "Multiaxial mechanical properties and constitutive modeling of human adipose tissue: A basis for preoperative simulations in plastic and reconstructive surgery," *Acta Biomaterialia*, vol. 9, no. 11, pp. 9036–9048, 2013.

[2] M. Wu, J. Bogaert, J. D' hooge, K. Sipido, F. Maes, S. Dymarkowski, F. E. Rademakers, and P. Claus, "Closed-chest animal model of chronic coronary artery stenosis. Assessment with magnetic resonance imaging," *The International Journal of Cardiovascular Imaging*, vol. 26, no. 3, pp. 299–308, 2010.

[3] M. S. Sacks, "Biaxial Mechanical Evaluation of Planar Biological Materials," pp. 199–246, 2001.

[4] I. J. LeGrice, B. H. Smaill, L. Z. Chai, S. G. Edgar, J. B. Gavin, and P. J. Hunter, "Laminar structure of the heart: ventricular myocyte arrangement and connective tissue architecture in the dog," *Am J Physiol*, vol. 269, no. 2 Pt 2, pp. H571–82, 1995.

[5] P. Tong and Y.-C. Fung, "The stress-strain relationship for the skin," *Journal of Biomechanics*, vol. 9, no. 10, pp. 649 – 657, 1976.

Standing Balance Assessment of the Elderly Using Kinect Sensor with Wii Balance Board

ST. Yang[1], JW. Seo[1], DH. Kim[1], DW. Kang[2], JS. Choi[1, 2], and GR. Tack[1,2]
[1] Dept. of Biomedical Engineering, Konkuk University, Chungju, Korea
[2] BK21 Plus Research Institute of Biomedical Engineering, Konkuk University, Chungju, Korea

Abstract - *Portable low-cost Kinect sensor with Wii balance board was used to analyze standing balance ability of the elderly. Four subjects (age: 75.25 ± 8.44years, height: 153.38 ± 7.43cm, weight: 57.05 ± 8.26kg), who can walk alone and have a normal cognitive level, participated in this experiment. Based on Berg Balance scale (BBS) test, four subjects were divided into Healthy older (HO: 2 persons, BBS: 56.00 ± 0.00) and Impaired older (IO: 2 persons, BBS: 48.00 ± 2.00) group. Each subject performed one-minute standing balance test. Mediolateral & anterior-posterior movements of the center of mass and center of pressure of IO group were higher than those of HO group, which means the decreased balance ability in IO group compared with HO group. Therefore, it was possible to estimate simple balance assessment using Kinect sensor and Wii balance board at the same time.*

Keywords: Kinect sensor, Wii balance board, Elderly, Standing Balance.

1 Introduction

One third of over sixty-five years old elderly have an experience of fall accident [1]. Since fall can easily lead to other diseases, it is regarded as serious problem for the elderly. One of reasons for fall accident is decreased balance ability due to aging. Thus, it is important for the elderly to do balance ability test regularly. Balance assessment consisted of various movements for maintaining balance. In general, the 3D motion capture system is used to get kinematic data [2], and the force plate is used to acquire kinetic data [1] for the analysis of balance assessment. These systems are high-priced and spatially-limited. To overcome these limitations, simple and portable systems such as Microsoft Kinect [3] for the analysis of postural sway and Nintendo Wii balance board [4] for the replacement of the force plate have been used. However these studies are still in progress. Therefore the purpose of this study was to analyze standing balance of the elderly by using Kinect sensor with Wii balance board at the same time.

2 Method

2.1 Subjects

Four subjects (age: 75.25 ± 8.44years, height: 153.38 ± 7.43cm, weight: 57.05 ± 8.26kg), who can walk alone and have a normal cognitive level, participated in this experiment. The local Ethics Committee approved the study and all participants provided informed consent (Konkuk Univ. IRB, 7001355-201507-HR-068).

2.2 Experiments

Before actual experiment, based on Berg Balance (BBS) scale test, four subjects were divided into Healthy older (HO: 2 persons, BBS: 56.00 ± 0.00) and Impaired older (IO: 2 persons, BBS: 48.00 ± 2.00) group. As shown in Figure 1, each subject performed one-minute standing balance test on the Wii balance board and Kinect sensor that installed with 2 meters ahead of the subject.

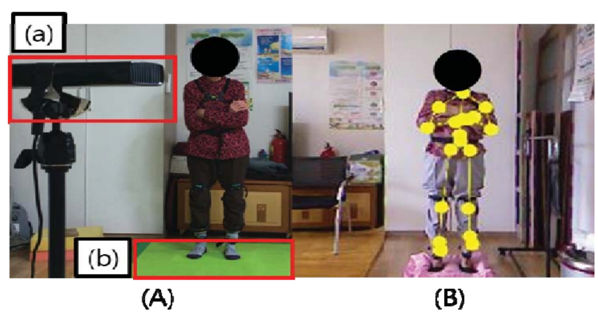

Figure 1 Experimental setup with (a) Kinect sensor (b) Hided Wii balance board (A) standing position (B) skeleton data by Kinect sensor.

2.3 Analysis & Variables

Data from Kinect sensor and Wii balance board was acquired with 30Hz sampling frequency and filtered with 7.5Hz low-pass-filter. Initial 30 seconds data was used for the analysis. The hip center trajectory (assumed as the center of mass trajectory, COM) in Kinect and the center of pressure trajectory (COP) in Wii balance board were used for postural sway analysis. Mediolateral (ML) & anterior-posterior (AP) directional components of root mean square (RMS), mean velocity (MV), mean distance (MDIST), and range of distance (ROD), and 95% ellipse sway area (AREA) of COM & COP were calculated. Matlab 2014a (MathWorks, Inc., USA) was used for all data collection and calculation.

3 Result

Table 1 showed the comparison between HO and IO using data from Kinect and Wii balance board. Results by two groups divided by the BBS score showed that data of IO group were bigger than those of HO group.

4 Discussion & Conclusion

As shown in Table 1, the results measured by using the Kinect and Wii balance board can be divided into two groups successfully almost same as BBS scores. The ML & AP directional movements of COM & COP of IO group were higher than those of HO group, which means the decreased balance ability in IO group compared with HO group. Therefore, it was possible to estimate simple balance assessment using Kinect sensor and Wii balance board, and it could be applied to studies of fall of the elderly. Further studies such as the increased number of subjects and the statistical analysis are necessary to enhance the purpose of this study. Correlation study between the variables by Kinect sensor and the variables by Wii balance board is in progress for find parameters for proper fall prediction in the elderly.

5 Acknowledgement

This research was supported by the National Research Foundation of Korea (NRF) Grant funded by the Korea government (MSIP) (Nos. 2013R1A1A1009571 and 2013R1A2A2A030 14511).

6 References

[1] JW. Kim, GM. Eom, CS. Kim, DH. Kim, JH Lee, BK Park, JH Hong. “Sex Differences in The Postural Sway Characteristics of Young and Elderly Subjects During Quiet Natural Standing”; Geriatrics & Gerontology International, Vol. 10, Issue 2, 191—198, Apr 2010

[2] BL. Day, MJ. Steiger, PD. Thompson, CD Marsden. “Effect of Vision and Stance Width on Human Body Motion when Standing: Implications for Afferent Control of Lateral Sway”; Journal of Physiology, Vol. 469, 479—499, Sep 1993

[3] RA. Clark, YH. Pua, K. Fortin, C. Ritchie, KE. Webster, L. Denehy, AL. Bryant. “Validity of Microsoft Kinect for Assessment of Postural Control”; Gait & Posture. Vol. 36, 372—377, Mar 2012.

[4] A. Huurnink, DP. Fransz, I. Kingma, JH. Van Dieen. “Comparison of a Laboratory Grade Force Platform with a Nintendo Wii Balance Board on Measurement of Postural Control in Single-leg Stance Balance Tasks”; Journal of Biomechanics, Vol. 46, Issue 7, 1392—1395), Apr 2013.

Table 1 Comparison between two groups using Kinect sensor and Wii Balance Board.

			Medio-Lateral				Anterior-Posterior				
			RMS	**MDIST**	**ROD**	**MV**	**RMS**	**MDIST**	**ROD**	**MV**	**AREA**
HO	**Subject 1**	**COM**	1.15	0.94	6.20	6.88	3.33	2.81	14.39	2.48	72.81
		COP	0.75	0.59	4.20	5.19	3.69	2.91	19.16	6.69	49.72
	Subject 2	**COM**	1.27	1.10	4.83	1.08	2.08	1.63	9.66	1.29	39.74
		COP	0.87	0.72	4.99	4.50	2.36	1.91	11.56	7.18	38.53
IO	**Subject 3**	**COM**	8.34	7.24	31.75	6.37	5.52	4.24	28.64	6.18	869.06
		COP	9.00	7.47	46.46	10.21	7.20	5.54	40.93	13.90	1191.55
	Subject 4	**COM**	7.05	5.25	30.70	4.67	5.66	4.67	28.31	5.11	754.57
		COP	7.99	6.20	37.20	9.67	7.81	6.33	46.92	14.80	1180.37

RMS: root mean square (mm), MDIST: mean distance (mm), ROD: range of distance (mm), MV: mean velocity (mm/s), AREA: 95% ellipse area (mm²), HO: healthy older, IO: Impaired older, COM: hip center trajectory from Kinect sensor, COP: center of pressure trajectory from Wii Balance Board.

Characterization of left atrial passive tissue parameters

N. Popovic[1], P. Haemers[2], R. Willems[3], P. Claus[1]
KU Leuven, Department of Cardiovascular Sciences, Belgium
[1]Division of Cardiovascular Imaging and Dynamics
[2]Division of Experimental Cardiology
[3]Division of Cardiology

Abstract— *One of the important problems in the field of cardiac mechanics research is the wall stress distribution. Wall stress prediction under different physiological and pathological conditions relies on the accurate modeling of the bio mechanical soft tissue characterization. Reliable tissue characterization relies on the well-defined mechanical testing protocol, as well as accurate identification of constitutive models. In this research, we aim to assess both mechanical testing protocol and applicability of different constitutive models, developed for the cardiovascular system on the thin wall of the left atrium (LA).*

Keywords: *Atrial fibrillation, Constitutive modeling, Tissue Mechanics*

1. Introduction

Mechanical characterization of the soft tissue constituents of the cardiovascular system can provide a deeper understanding of the cardiac function in both physiological and pathological sense. There have been multiple attempts on characterization of the left ventricle (LV) [1] and aortic tissue [2], and few on the LA [3] [4].

LA wall characterization needs to take account for the LA wall structure, which differs significantly from the LV wall structure. Here we will focus on the possible application of the already developed cardiovascular constitutive models on the LA.

2. Methodology

2.1 Bi-axial testing

Mechanical tissue testing was performed using a bi axial tissue tester (BioTester 5000, CellScale Biomaterials Testing, Waterloo, Canada). The setup was equipped with two 2.5 N load cells, with a $25mN$ precision.

Sheep LA was used for characterization. Four small surgical thread markers were glued onto the midsection of each specimen (Fig. 1). The maximal loading pressure was set to 20 kPa. Samples were tested under 5 different loading protocols with different ratios between maximal loading in the x and y direction (x:y axis loading force ratios $1:1$, $1:.75$, $1:.5$, $.75:1$, $.5:1$).

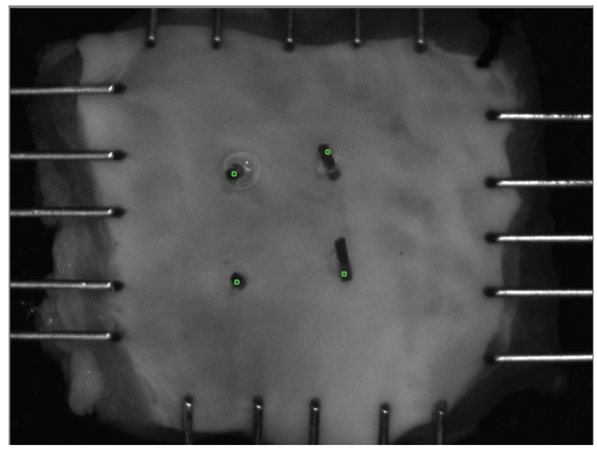

Fig. 1: Sample mounted on the Cell Scale system.

3. Data analysis

Numerous soft tissue mechanical characterization studies consider myocardium as an incompressible continuous medium, meaning that the sample volume is preserved during the experiment. Besides this assumption, we consider also homogeneous deformation and kinematics to be affine. We considered basic bi-axial test kinematics as given in [5].

The momentum balance law for a continuous medium can be expressed in terms of stresses and strains. During a bi-axial stress test, the tissue undergoes large deformations. Large deformation, strain measures the relationship between an undeformed and deformed body configuration. While displacement is defined as a relationship between point locations, the deformation gradient is defined by a change in material vector between both configurations.

The assumptions that were made about the atrial tissue justify the use of a strain energy function W to define the stress-strain relationships in this tissue. A subset of materials for which such a function exists are called Green elastic materials. The stored energy solely depends on the strain value, and not on the deformation path.

4. Result

4.1 LA myocardial wall structure

Unlike the left ventricle (LV) wall structure, which is believed to be organized in sheets of muscle fibers wounded helically around the ventricles [6], LA myocardial wall structure is shown to be highly anisotropic. Depending on the region, the atrial wall thickness is highly variable, and overall significantly thinner than LV wall. It consists of complexly arranged fibers [7], who's direction have not been fully determined, except for major fiber bundles [8]. A huge effort has been made to map the complete fiber structure of the atria [9].

4.2 Constitutive models

Constitutive models can be divided into structural and phenomenological. Most famous phenomenological model is Fung-type model [10]. Although phenomenological models can provide excellent fit to the experimental data, they provide no physiological explanation, nor do they guarantee strain energy convexity.

Based on the Holzapfel arterial model [2],and [3] a similar approach was taken into developing a tissue microstructural model, based on dominant fiber directions. The original arterial model decomposed the strain energy into an isotropic and an anisotropic part, which represent the ground collagen matrix and the fiber structure respectively $W = W_{iso} + W_{aniso}$

The anisotropic part of the original model, as it was developed for the artery, accounted for two separate layers, each of which consists of two fiber families. This model adaptation accounts for one tissue layer, that consists of two fiber families with independent crossing angle, embedded into the ground collagen matrix.

$$
\begin{aligned}
W &= W_{iso} + W_{aniso} && (1)\\
W_{iso} &= C_{iso}(I_c - 3) && (2)\\
a_0 &= [cos\alpha_i, sins\alpha_i, 0] && (3)\\
A_0 &= a_0 \otimes a_0 && (4)\\
I_{(2i+2)c} &= max(C : A_0, 1) && (5)\\
W_{aniso} &= \frac{k_1}{2k_2}[e^{k_2 * p_i (I_{(2i+2)c} - 1)^2} - 1] && (6)\\
S_{11} &= 2C_{iso}(1 - C_{22}C_{33}^{-2}) \\
&\quad +2k_1(I_{(2i+2)c} - 1)e^{k_2 * p_i (I_{(2i+2)c} - 1)^2} && (7)\\
S_{22} &= 2C_{iso}(1 - C_{11}C_{33}^{-2}) \\
&\quad +2k_1(I_{(2i+2)c} - 1)e^{k_2 * p_i (I_{(2i+2)c} - 1)^2} && (8)
\end{aligned}
$$

The explanation of the used parameters is as follows: C_{iso} is an isotropic material parameter; k_1 a stress-like parameter; k_2 a weighting parameter; p_i the contribution of the fiber family, with a condition that $p_1 + p_2 = 1$, and α_i the fiber family angle.

The data were fitted with a custom made routine that combines least-square data fitting and graphical fitting. The least-square fitting was performed with multiple starting parameter combinations. The goodness of the fit was assessed with a graph fitting method. In a graph fitting method, goodness of the fit is estimated by the maximal absolute distance from the original points. To avoid over fitting, we discarded 5% of the points with the worst fit. We were able to obtain total accuracy of the fit R^2 of $0,98$.

5. Conclusion

Investigation of mechanical remodeling requires an accurate mathematical description of the material. This characterization was performed using continuum mechanics.

Structurally motivated constitutive models integrate information about the underlying tissue composition, and can offer further understanding of the tissue characteristics. These models should have greater predictive potential, as it is possible to analyze parameters with physiological meaning.

Structurally motivated models are proposed for different types of soft tissue. Here, we have adapted an aortic model proposed by Holzapfel [2]. This model describes the behavior of tissue that is composed of an isotropic grand matrix, and anisotropic part that consists of multiple fiber families, each described by a main fiber angle and pressure characteristics.

In the original model, tissue is composed of two equally contributing fiber families with symmetrical opening angles. Here, we have adapted the model so that it can describe multiple fiber families with independent opening angle and different contribution.

References

[1] G. Sommer, M. Eder, L. Kovacs, H. Pathak, L. Bonitz, C. Mueller, P. Regitnig, and G. a. Holzapfel, "Multiaxial mechanical properties and constitutive modeling of human adipose tissue: A basis for preoperative simulations in plastic and reconstructive surgery," *Acta Biomaterialia*, vol. 9, no. 11, pp. 9036–9048, 2013.

[2] G. A. Holzapfel, T. C. Gasser, and R. A. Y. W. Ogden, "A New Constitutive Framework for Arterial Wall Mechanics and a Comparative Study of Material Models," pp. 1–48, 2001.

[3] C. Bellini and E. S. Di Martino, "A mechanical characterization of the porcine atria at the healthy stage and after ventricular tachypacing.," *Journal of biomechanical engineering*, vol. 134, p. 021008, Feb. 2012.

[4] C. Bellini, E. S. Di Martino, and S. Federico, "Mechanical Behaviour of the Human Atria.," *Annals of biomedical engineering*, Dec. 2012.

[5] M. S. Sacks, "Biaxial Mechanical Evaluation of Planar Biological Materials," pp. 199–246, 2001.

[6] S. Göktepe, S. N. S. Acharya, J. Wong, and E. Kuhl, "Computational modeling of passive myocardium," no. June 2010, pp. 1–12, 2011.

[7] S. Y. Ho and D. Sánchez-Quintana, "The importance of atrial structure and fibers.," *Clinical anatomy (New York, N.Y.)*, vol. 22, pp. 52–63, Jan. 2009.

[8] S. Y. Ho, J. A. Cabrera, and D. Sanchez-Quintana, "Left atrial anatomy revisited.," *Circulation. Arrhythmia and electrophysiology*, vol. 5, pp. 220–8, Mar. 2012.

[9] J. Zhao, T. D. Butters, H. Zhang, A. J. Pullan, I. J. LeGrice, G. B. Sands, and B. H. Smaill, "An image-based model of atrial muscular architecture effects of structural anisotropy on electrical activation," *Circulation: Arrhythmia and Electrophysiology*, vol. 5, pp. 361–370, 2012.

[10] S. Federico, A. Grillo, G. Giaquinta, and W. Herzog, "Convex Fung-type potentials for biological tissues," *Meccanica*, vol. 43, pp. 279–288, Nov. 2007.

Gesture-based controller using wrist electromyography and a neural network classifier

Siho Shin, Seokeun Park, Jaehyo Jung and Youn Tae Kim+
IT Fusion Technology Research Center, Chosun University, Gwangju, Korea
+petruskim@chosun.ac.kr

Abstract - *In this paper, we present an electromyography (EMG)-based band type controller that recognizes finger or palm moves. The proposed band type controller detects the electric signals associated with the desired finger movements using surface EMG. The obtained signal is then filtered by an adaptive filter to remove noise. After feature extraction in both the frequency and time-frequency domains, the movement of each finger is detected, using a neural network for pattern recognition. This device can be used in various applications and roles, such as game controller, internet of things control device, rehabilitation equipment control, and so forth.*

Keywords: EMG; adaptive filter; FFT; wavelet; neural network

1 Introduction

In today's modern society, many highly sensorial advanced technologies are being studied and pursued; that is the case of the Internet of Things in various smart home applications and is also the case of Virtual Reality and Augmented Reality applied to various technologies, games, and fitness equipment [1]. To operate the aforementioned systems, physiological signals are required, and a variety of controllers integrating physical sensors such as acceleration sensors or gyroscopes are often used. Examples of such controllers currently being commercialized are the finger type "Dexmo" controller [2], the "Leap motion controller" for personal computers [3], the bluetooth based "Nuimo" controller [4], and the band type "Myo armband" controller [5]. These products do have some disadvantages such as uncomfortable fit and limited signal recognition abilities. In this paper, we propose a band-type controller device based on the wrist's electromyography (EMG) signal. The signal measured by the electrode attached to the bottom part of the controller is amplified and filtered. It is then processed with some signal processing techniques, such as the fast Fourier transform (FFT), wavelet transform, and neural network based algorithms. We expect this EMG-based controller to become a useful tool.

2 Method

A. System configuration

The proposed band-type EMG controller can be described as follows: a measuring electrode is built into the surface where skin and device meet; the signal received by the measuring electrode is amplified and passed to an adaptive filter [6]. After that, the signal components related with finger movement are obtained through FFT and wavelet transform processing [7]. Those components are then passed to a neural network for further processing, finalizing the identification, and classification of the detected finger movements. The processed data is then used to pass the orders implied by those finger movements to the various devices, which are therefore controlled in this manner [8].

B. Electromyography

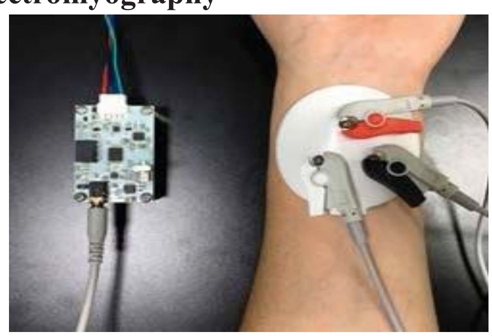

(a)

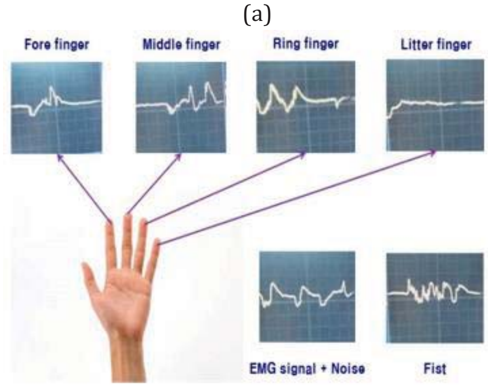

(b)

Fig. 1 (a) EMG measurement. (b) EMG signal of individual fingers.

Using a surface EMG in this context means that we are measuring the electrical signal generated when the finger muscles contract, at the surface of the skin. This work was preceded by (and builds upon) a study where the electrical signals generated from each finger (see Fig.1 (b)) were measured by attaching a wet electrode to the wrist and using an EMG module of PhysioLab Co. (PSL-iEMG2). The signals were measured when each finger was bended, starting from a spread hand initial state. In this work, we designed a system to classify the finger-generated signals using wavelets, FFTs, and neural network algorithms.

C. Signal processing

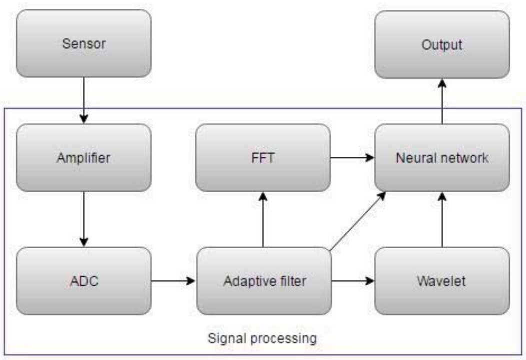

Fig. 2 System diagram.

Figure 2 shows a diagram of the system configuration. The raw EMG signal detected with the wrist electrode has a very small amplitude (in the microvolts to millivolts range). Therefore, it is amplified before being sampled. From then on, all processing is digital. First, the noise in the amplified signal is removed by an adaptive filter to clean the signal as much as possible. Figure 3 shows a schematic diagram of the adaptive filter. In this figure, s1, n1, and n2 represent the raw EMG signal, the additive noise in the raw signal, and a sequence of reference noise, respectively. The overall effect of this filter is to subtract the additive noise contained in the collected EMG signal using an adaptively controlled version of the reference signal (y), as seen in Equation (1).

$$e = (s1 + n1) - y \qquad (1)$$

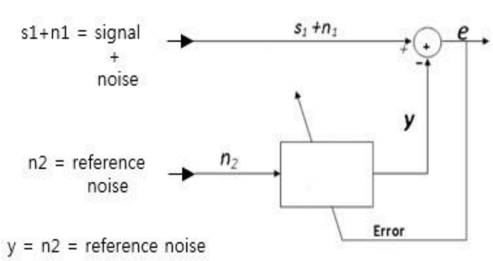

Fig. 3 Schematic diagram of the adaptive filter.

The filtered signal then goes through an FFT and a wavelet transform to obtain both its frequency and time-frequency characteristics. The obtained information is finally fed to a neural network based algorithm to exactly determine (classify) the observed finger movements.

3 Conclusions

We suggested a band-type controller that can identify the user's finger movements by processing the wrist EMG signal measured on the wrist. The wrist controller is simple to wear and operate; the control actions are performed by simply moving the individual fingers in accordance with the chosen control patterns. The proposed system needs further study, namely to address the problems of the adaptive filter vulnerability to unexpected types of noise, and the differing body structures between different people. We expect to apply this controller to various systems such as home automation systems, Internet of Things applications, virtual reality systems, and augmented reality systems.

4 References

[1] Y. M. Aung A. Al-Jumaily, "Rehabilitation exercise with real-time muscle simulation based EMG and AR", Hybrid Intelligent Systems (HIS), 2011 11th International Conference on, 5-8 Dec. 2011, pp.641 - 646 [2] Dexmo. Available at http:// www.dextarobotics.com/ products.php?div=dexmo

[3] P.Chophuk, S.Chumpen, S.Tungjitkusolmun and P.Phasukkit, " Hand Postures for Evaluating Trigger Finger Using Leap Motion Controller ", The 2015 Biomedical Engineering International Conference (BMEiCON-2015)

[4] Nuimo. Available at https:// www.kickstarter.com/ projects/ 802159142/ nuimo-seamless-smart-home-interface

[5] R. Lipovsky H. A. Ferreira, "Hand therapist: A rehabilitation approach based on wearable technology and video gaming ", 26-28 Feb. 2015, pp. 1- 2

[6] Md. Zia Ur Rahman, Rafi Ahamed Shaik, D V Rama Koti Reddy, "Noise Cancellation in ECG Signals using Computationally Simplified Adaptive Filtering Techniques: Application to Biotelemetry" Md. Zia Ur Rahman, Rafi Ahamad Shaik & D V Rama Koti Reddy,

[7] Nayan M. Kakoty, Mantoo Kaibarta, Shyamanta M. Hazarika "Electromyographic Grasp Recognition for a Five Fingered Robotic Hand", International Journal of Robotics and Automation, Vol. 2, No. 1, March 2013, pp. 1 – 10 [8] Y. Matsumura Y. Mitsukura, M. Fukumi, N. Akamatsu, "Recognition of EMG signal patterns by neural networks", Neural Information Processing, 2002. ICONIP '02. Proceedings of the 9th International Conference on (Volume:2), 18-22 Nov. 2002, pp.750 - 754 vol.2

Preliminary Study on Finger Gestures for Surface Electromayograph (sEMG) based Number Recognition

C. Kwon[1], J. Park[1], and H. Kang[2]
[1]Department of Medical IT Engineering, Soonchunhyang University, Asan, ChungNam, South Korea
[2]Department of Sports Medicine, Soonchunhyang University, Asan, ChungNam, South Korea

Abstract – *Wide use of surface electromyograph (sEMG) has been made for efficient recognition of finger gestures due to its convenient to use and distinguishing signal patterns along finger movements. For high classification accuracy, it is important to have a consistent feature of sEMG signal feature for each finger gesture of a number. However, feature of sEMG signal for identical finger gesture can be different because of different muscle activation even in identical shape of gesture. Thus the experimental results in this work may motivate further study on how to make consistent muscle activation for a finger gesture at each try.*

Keywords: Number recognition, Finger gestures, Surface electromyograph

1 Introduction

Surface electrograph (sEMG) has been widely used in gesture recognition based application such as gross hand, wrist and arm movement recognition [1]-[3]. These movements provide consistent sEMG signals to distinguish sEMG activation patterns since gestures may accompany consistent engagement of the related muscles [1]-[2].

However, finger movement recognition is generated by flexon and extension of the individual thumb, index, middle, ring and little fingers whose are placed at three layers in the forearm [3]-[5]. Therefore, identical finger gesture may not always make consistent sEMG signals at every gesture. This possible inconsistency between finger gesture and sEMG signal brings motivation to this work.

To this end, this work carried out comparative study between sEMG signals from one paper in the literature and sEMG signal measured in this work for the same finger gesture. The comparative study tells that there were inconsistent sEMG signals even in identical finger gestures. This may motivate further research to set up guidelines for finger gestures with degree of muscle activation.

2 Materials and methodology

For comparative study to see inconsistent sEMG signals for identical finger gesture, reference [4] is selected. Therein, ten Chinese finger gestures for natural number from zero to nine. Ten Chinese finger gestures as illustrated in Fig. 1. With this, sEMG signals are measured and recorded for each Chinese natural numbers and compared to the results in reference paper [5]..

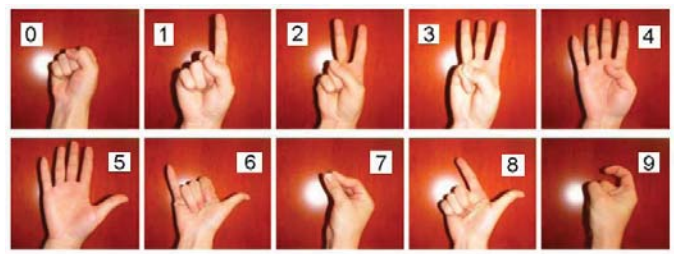

Fig. 1. Illustration of the Chinese number gestures signifying the natural numbers zero through nine [1]

2.1 Surface EMG system

Surface electromayograph (sEMG) used in this work is ActivII system of Biosemi, Inc. .This system has 24-bit high resolution Analog-to-digital device. In ActiveII system, differential sEMG signals at each channel between two electrodes on the measuring muscle are acquired by subtracting from sEMG signal at the one electrode to that at the other electrode

2.2 Experiment

2.2.1 Electrode placement

To measure sEMG signal at forearm when ten finger gestures are made, sEMG signal on four muscles are measured through the sEMG system. Those selected muscles are extensor pollicis brevis, extensor digitorum, flexor digitorum profundus for little finger and flexor digitorum superficialis..The electrode placements are depicted in Fig. 2.

2.2.2 Experimental protocol

To collect sEMG signals for comparison study, sampling frequency was set to be 1024Hz and bandpass filtered from 10Hz to 450 Hz. To acquire sEMG signals in high accurarcy, active electrode is used in ActiveII system.

ISBN: 1-60132-429-4, CSREA Press ©

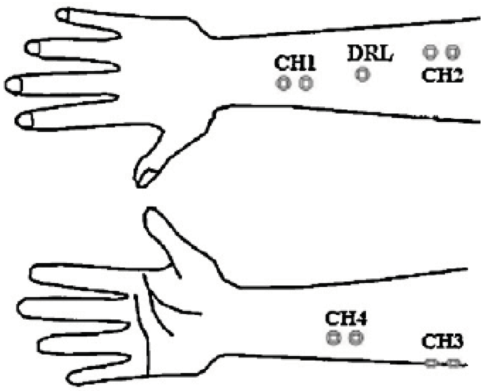

CH1:Extensor pollicis brevis, CH2:Extensor digitorum
CH3:Flexor digitorum profundus
CH4:flexor digitorum superficialis

Fig. 2. Electrode placements on forearms

2.3 Results

sEMG signals measured in this study are depicted in Fig. 3(a). For convenience purpose, the 4-channel sEMG is depicted in Fig. 3(b) [5]. Therein, it can be observed that overall pattern of sEMG signals for most finger gestures are similar with degree of tolerance but pattern of sEMG signals for finger gesture of zero, one, and seven are quite different. This is because degree of muscle activation made difference even in identical finger gesture.

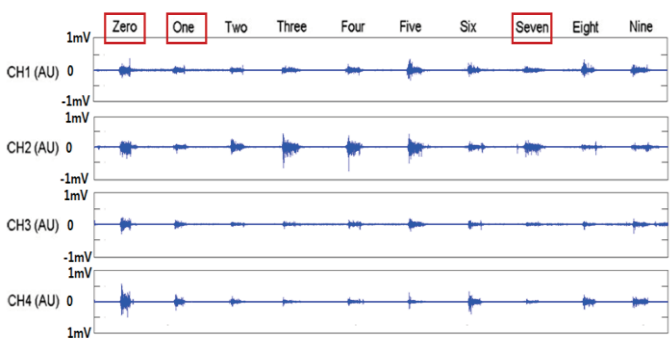

(a) 4-Channel sEMG signals measured for replication of [5]

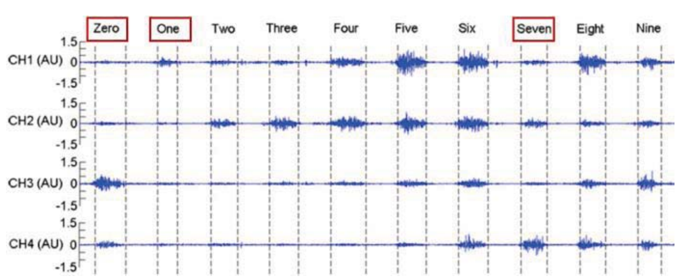

(b) An example of 4-channel sEMG signals in [5]

Fig. 3. An example of 4-channel sEMG signals corresponding to Chinese number gestures

3 Conclusions

Surface electromayograph (sEMG) has been one of the active recognition tools for finger gesture recognition. However, as the result in this work shows, sEMG signal could be different depending on how strongly the related muscles are activated even for identical gesture of the number to be recognized. This cause sEMG signals inconsistent to provide wrong feature, thus resulting in wrong classification. Therefore, it is important to set up the protocol for muscle activation of individual finger gesture corresponding to a number to be recognized. Thus, this work highlight further research to get consistent features for sEMG based finger gesture recognition.

4 Acknowledgement

This work was supported in part by Soonchunhyang University Research Fund and in part by Basic Science Research Program through the National Research Foundation of Korea(NRF) funded by the Ministry of Science, ICT and Future Planning (NRF-2013-R1A1A1013430)

5 References

[1] K.R. Wheeler and C.C.Jorgensen, "gestures as input : neuroelectric joysticks and keyboards". Pervasive Computing 2, 56-61, April 2003.

[2] M.A. Oskoei and H. Hu, "Myoelectric control systems-a survey"; Biomedical Signal Processing and Control 2, 275-294, October 2007.

[3] Maria Hakonen, Harri Piitulainen, Arto Visala, "Current state of digital signal processing in myoelectric interfaces and related applications"; Biomedical Signal Processing and Control, Vol. 18, 334-359, 2015.

[4] Maria Claudia F Castro, Sridhar P Arjunan and Dinesh K Kumar, "Selection of suitable hand gestures for reliable myoelectric human computer interface"; BioMedical Engineering, 2015.

[5] Xue Chen and Z. Jane Wang, "Pattern recognition of number gestures based on a wireless surface EMG system"; Biomedical Signal Processing and Control, Vol. 8, 184-192, 2013.

Wireless Spectrum-Capnography System for Detecting Cholesterol Levels in the Blood

J. Villatoro, and V. Vakilian
Department of Computer and Electrical Engineering & Computer Science
California State University, Bakersfield, California, United States

Abstract— *Cardiovascular disease is burdensome on healthcare system due to its associated cost of care and the fact that it is a silent killer. The disease kills in absence of symptoms. Nonetheless, regular screening for cholesterol may help determine onset and presence of the cardiovascular disease. In this paper, we propose a spectrum-capnography system that is able to detect the concentration of pCO_2 and isoprene and therefore measure the cholesterol ($C_{27}H_{26}O$) levels present in the blood. To achieve this, we use wireless sensor networking to design our low-cost spectrum-capnography prototype. Moreover, the proposed prototype provides the heart and respiratory rates employing the electrocardiographic (ECG) signal. We use the ZigBee technology to display the biomedical signals in mobile devices.*

Keywords: Isoprene, cholesterol, capnography, electrocardiographic signal, and ZigBee.

1. Introduction

Poor air exchange decreases the levels of oxygen and increases carbon dioxide levels. The poor gas exchange can lead to severe, life-threatening conditions such as cardiovascular disease [1], [2]. A popular method employed in clinics to detect and measure cholesterol levels is blood sampling that requires patients to present at health facilities. Blood sampling is invasive and painful, as well as unpleasant for many people. Breath sampling, on the other hand, is an efficient non-invasive and painless method to -measure cholesterol levels in the blood. The obtained information is very crucial for people with cardiovascular diseases.

Historically, early physicians knew that the human breath is associated with some asymptomatic diseases. However, they were unable to diagnostic those diseases due to their present technology. We propose a new way to take advance of breath diagnostic method using the spectrum-capnography prototype that measures the concentration of carbon dioxide (CO_2) in the human breath. The concentration of carbon dioxide is measured in percent of CO_2 the total air or the partial pressure of CO_2 in the total air. Infrared technology is used in capnography to detect and measure the concentration of carbon dioxide in the air [3]. The infrared rays are absorbed by non-elementary gasses, which are composed of dissimilar atoms (CO_2 composed of carbon and oxygen atoms), while certain gasses absorb a specific wavelength that produces absorption bands on the infrared electromagnetic spectrum.

The intensity produced by the infrared light is projected through a gas mixture containing carbon dioxide that this allows the carbon dioxide absorption band to be identified and is proportional to the amount of carbon dioxide in the mixture [4]. Moreover, carbon dioxide possesses a strong absorption ability infrared radiation [5]. With this infrared and carbon dioxide characteristic, infrared light is used in capnography to detect and measure the amount of concentration of carbon dioxide in breathing air. According to Linus Pauling, there are more than 200 different volatile organic compounds (VCOs) in the exhaled air that can be used as disease markers [6]. When carbon dioxide reacts with water, it forms carbonic acid (H_2CO_3). Carbonic acid is involved in the transport of CO_2 out of the body via respiratory gas exchange.

The hydration reaction of CO_2 is very slow when a catalyst is not present. However, red blood cells contain an enzyme, carbonic anhydrase, which is responsible for increasing the dissociated reaction rate with hydrogen ion (H^+) from the resulting carbonic acid, leaving bicarbonate (${HCO_3}^-$) dissolved in the blood plasma [7]. This reaction increases the production of isoprene (C_5H_8) that is associated with cholesterol [8]. Lack of standard procedure for respiration analysis, and also high cost of the monitoring breath devices, limits exploiting the full potential of this biological fluid for clinical diagnosis [9]. The goal of this research is to propose a low-cost non-invasive monitoring device that can read the cholesterol levels in the blood using the concentration of carbon dioxide with ZigBee wireless technology [10]. It incorporates analog and digital blocks such as (IR light, electrodes, and pressure) sensors, and LabVIEW in order to display the biomedical signals in mobile devices.

2. Signal Models

The first model uses to measure the concentration and absorption of CO_2 and isoprene gasses is the Beer's law equation:

$$R = \frac{\log_{10}(I_{\mathrm{ac}})\lambda_1}{\log_{10}(I_{\mathrm{ac}})\lambda_2}, \tag{1}$$

where λ_1 is the wavelength of red light at 660nm and λ_2 is the wavelength of infrared light at 940nm.

The second model mixes the persons air fluid with H_3O^+ that performs proton transfer with VCOs organic compounds:

$$\mathrm{H_3O^+} + R \to^{\kappa} R\mathrm{H^+} + \mathrm{H_2O}, \tag{2}$$

where R is the gas constant and κ is the proton transfer rate constant [11]. The Third model is the Henry's law equation:

$$\mathrm{C}_D(V) = \mathrm{C}_{V_0} \exp(-\frac{V_{br}}{H.R.T.V_0}.\frac{V}{HBV}), \tag{3}$$

where V is the volume, H is the Henry's law constant, T is the temperature, V_0 is the total volume of the lungs, HBV is the heartbeat volume, and $C_D(V)$ is the concentration that chance from one differential volume of the lung.

3. Results

In this section, we present the results of measuring the pCO_2 concentration using a CO_2 sensor, infrared light, and visible light. We study the pCO_2 concentration of a female adult during exercise using a CO_2 sensor. As shown in Fig.1, we measure the breath rate continuously during thirty seconds using the MG811/MG-811 CO_2 Carbon Dioxide Sensor for Arduino; however, the experimental results only show the CO_2 concentration. Within 15 s, CO_2 decrease from 65 to 5 mmHg. Thereafter, CO_2 increased steadily similarly to that from starting values. We then use the obtained results to compare with the isoprene values that are strong related to the pulmonary CO_2 exchanges.In addition, Isoprene has a high adherence with CO_2. Therefore, the ratio values between CO_2 and isoprene are used in order to obtain the cholesterol ($C_{27}H_{26}O$) levels present in the blood.

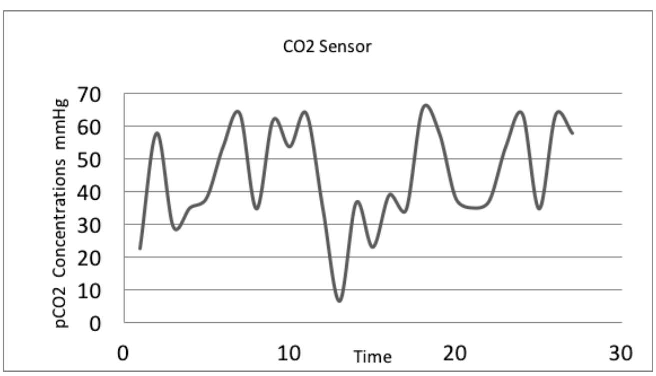

Fig. 1: Analysis of breath CO_2 concentration of a female adult during exercise.

We also use the infrared and visible lights to determine the pCO_2 concentration in the venous and arteries, respectively. The results are summarized in Table 1. The physiological range of venous CO_2 concentration is between 30-50 mmHg, and arterial CO_2 concentration is between 80-105 mmHg. Those values are compared with the venous blood isoprene concentration that helps us to reveal the cholesterol levels in blood.

Table 1: Analysis of CO_2 concentration in the veins and arteries.

CO_2 Concentration During Exercise								
Venous	22	29	38	64	64	23	34	IR light
Arterial	58	35	54	35	35	37	34	Red light

To eliminate measurement noise, the bioelectrical data obtained from sensors are processed by digital signal processing (DSP).

4. Conclusions

In this paper, we propose a new breath sampling method to determine the cholesterol levels in the blood. The main idea is to sense the exhaled breath gas using infrared (IR) light, CO_2 sensor, and a spectrophotometer to measure the isoprene concentration. The obtained data from these sensors contain information about the pCO_2 and isoprene (cholesterol biosynthesis) concentrations that help to measure the cholesterol levels in blood. We process the measured data via a microcontroller and ZigBee card to determine the cholesterol levels and display these values in a mobile device. In addition, we use the ECG signal obtained by electrode sensors to support the results of the capnograph for detecting cardiovascular disease, which is a disease, associated with an elevated cholesterol level.

References

[1] S. Chatterjee and A. Miller, *Biomedical Instrumentation Systems*. Cengage Learning, 2010.
[2] G. J. Tortora and B. H. Derrickson, *Principles of anatomy and physiology*. John Wiley & Sons, 2008.
[3] A. Prabhakar, "Portable sensors for breath analysis," Ph.D. dissertation, Arizona State University, 2013.
[4] T. T. Kean, A. Teo, and M. Malarvili, "Feature extraction of capnogram for asthmatic patient," in *Computer Engineering and Applications (ICCEA), 2010 Second International Conference on*, vol. 2. IEEE, 2010, pp. 251–255.
[5] J. D. Fenske and S. E. Paulson, "Human breath emissions of vocs," *Journal of the Air & Waste Management Association*, vol. 49, no. 5, pp. 594–598, 1999.
[6] B. Buszewski, M. Kęsy, T. Ligor, and A. Amann, "Human exhaled air analytics: biomarkers of diseases," *Biomedical Chromatography*, vol. 21, no. 6, pp. 553–566, 2007.
[7] P. Kalsi, *Spectroscopy of organic compounds*. New Age International, 2007.
[8] I. Blei and G. Odian, *General, Organic, and Biochemistry Media Update*. Macmillan, 2008.
[9] R. A. Klocke, "Carbon dioxide transport," *Comprehensive Physiology*, 1987.
[10] P. Frehill, D. Chambers, and C. Rotariu, "Using zigbee to integrate medical devices," in *Engineering in Medicine and Biology Society, 2007. EMBS 2007. 29th Annual International Conference of the IEEE*. IEEE, 2007, pp. 6717–6720.
[11] T. Karl, P. Prazeller, D. Mayr, A. Jordan, J. Rieder, R. Fall, and W. Lindinger, "Human breath isoprene and its relation to blood cholesterol levels: new measurements and modeling," *Journal of Applied Physiology*, vol. 91, no. 2, pp. 762–770, 2001.

SESSION

LATE BREAKING PAPERS

Chair(s)

TBA

ISBN: 1-60132-429-4, CSREA Press ©

THE PHOTON IS AN ENERGETIC PROPELLANT

Dr. Boucherit Taieb,
BOUCHERIT Laboratory, Boucherit mounir, Yagoubi Abdelkader Oran, Algeria.
07, road kaddour salah houari Delmonte Oran, Algeria
Sponsored by **Dr.Abdelmalek Boudiaf, Minister of Health**, Algeria

Abstract **–**The VIS system or "vitreous- imaging-system" and the M.MR are techniques that allow us to see the infinitely small in real images with unprecedented accuracy (published at WorldCom'11 WorldComp'13et WorldComp'14) by applying these technicson photons, it allows us to explore an unknown world which is that of the infinitely small and allows us to discover the real images of photons and their internal constitutions, it allows us to discover and understand many things while we encounter the theoretical questions that the current scientific community can not answer. I invite you to discover these extraordinary pictures with me, and judge these explanations and theories arising.

1 Introduction

The images of photons obtained by the V.I.S system or M.M.R system show us photons into real images as well as their internal constitution, with these imaging systems exploring the world of the infinitely small is in our reach, it allows us to answer several questions posed at present by scientists, questions remained without answers since they are based only on theoretical speculations what follows, is unique and is completely changed our view to the infinitely small, the images are extraordinary and the answers are even more astonishing. Be the judge and Ihoping to provide some answers to the questions that today's science incomplete theories.

2 Materials and Methods

2.1 Materials

The material is very simple; it consists of a camera & computer,

2.2 Methods

- Photo of the eye.
- Front view photo of the eye
- Camera without flash
- Environment slightly enlightened without source light
- The "*vitreous imagery system*" makes it possible to visualize the images of the patient's organs in the vitreous humor, these images are laid out in bulk, with sometimes the repetition more than one organ same organ with different view.
  - We resize each image of organs obtained in the humor vitreous to isolate each image.

2.3 Theory and explanation

We know without going into too complicated technical details that light consists of particles called photons, these particles have almost no mass, almost no electric charge and move at a speed of 300.00 km / s constantly. I most of scientific research cases, the most logical and easiest research questions put us on the path to success. In this case we have a particle moving at the velocity of light.

1. ***what are its means of propulsion?***
2. ***Why propulsion is at this speed ?***
3. ***Itinerary of Pathway ?***

1- by what are the propulsion means of a photon ?

All answers given to this question are pure speculations, because there is no scientific equipment that can allow us to study the internal and external structure of the photon. Any physical object (mass or energy) has two ways to gain speed, it is propelled by an external system, or its method of propulsion is internal. The logic allows us to say that any object that is moving at a certain speed with anexternal propulsion (he was pushed) slowed its speed in time (example: a fired bullet)in the other hand, any object that has its own means of propulsion, can have a speed which can increase, decrease or remain constant. The photon travels at a speed of 297,790 km / s at a constant speed (Einstein's theory), so from this, we can say that the propulsion means of the photon are internal. The VIS system can visualize the photon in real image, it can show us its internal and external structure and provide us with an accurate and actual answers on the photon, we will follow step by step and frame by frame everything that relates to this question of propulsion and have the first real image of the photon image obtained from a photonic binary algorithm and non-digital binary system (refer to publications at WorldComp'11 and WorldComp'13 WorldComp'14) or at length I developed the two binary digital systems and photonics.

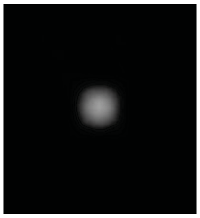
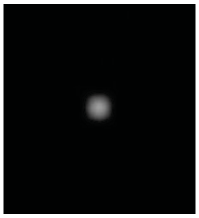
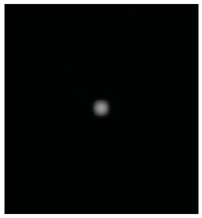

Img : photon img : photon img : photon

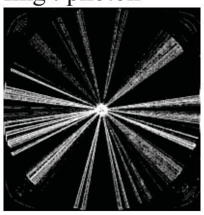
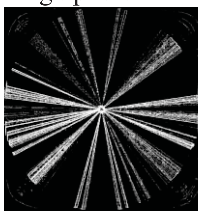
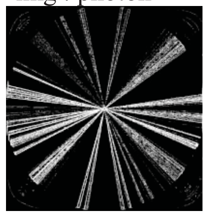

Img001 img002 img003

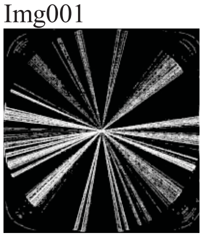
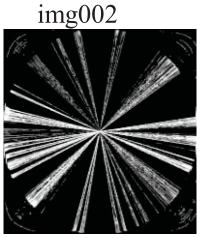
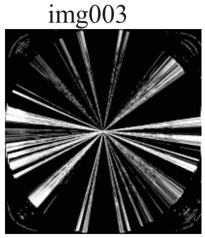

Img004 img005 img006



Img005 img006 img007

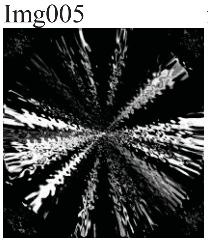
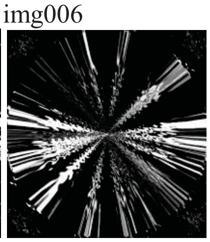
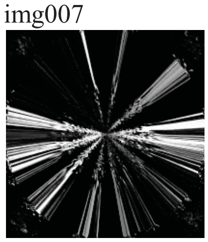

Img008 img009 img010


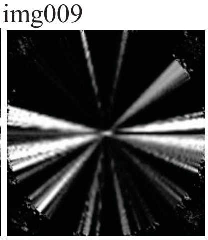
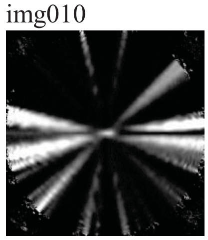

Img011 img012 img013

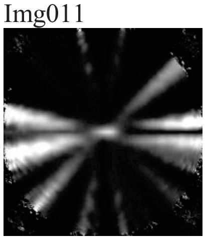

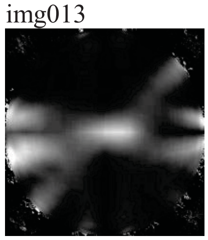

Img014 img015 img016

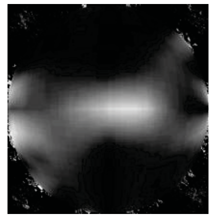
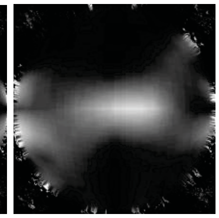
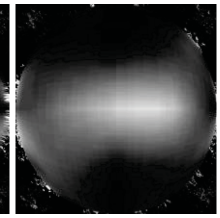

Img017 img018 img019

All images from img001 to img019 show a photon in real acceleration, and images from img001 to img010 display the photon at its departure with the generated fields by its speed of propulsion, in images 011 to 019 its return, always compared to a fixed examiner, V.I.S system is a technique allows us to see the internal photon structure.

We will now study with this technique img019 which is a "Data Bank Images"

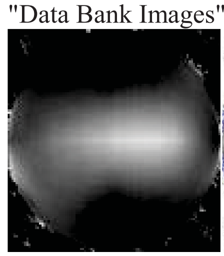
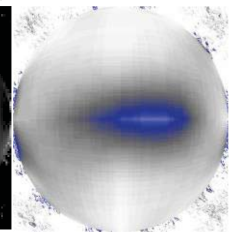
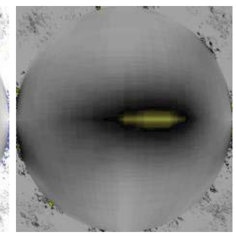

Img020 img021 img022

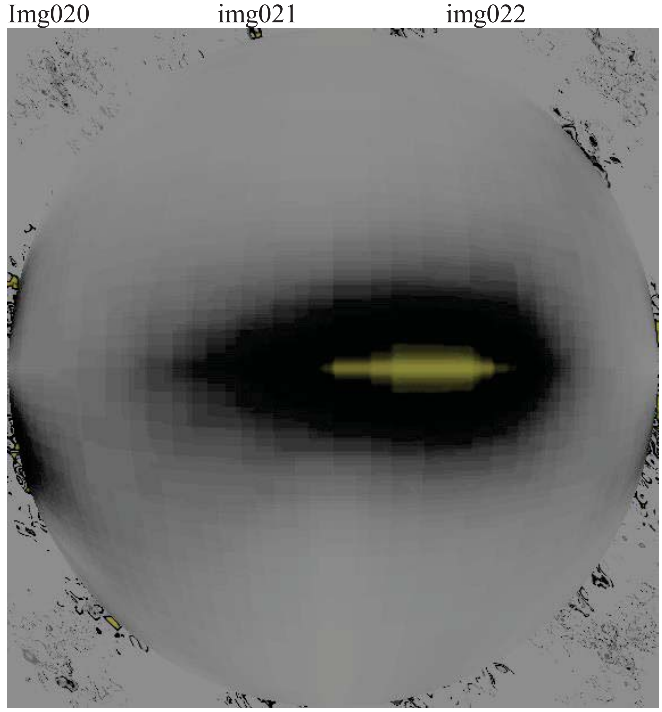

Img022

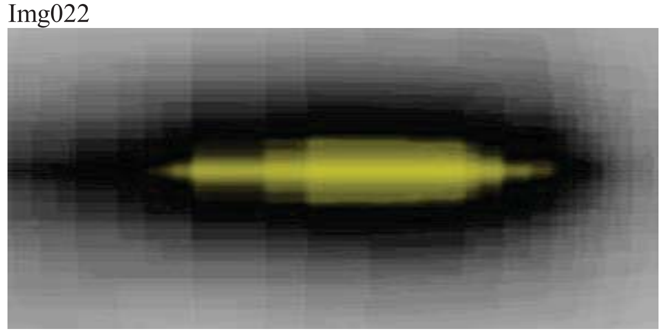

Img023

ISBN: 1-60132-429-4, CSREA Press ©

So, Beginning by a photon, and while passing by these various steps, the V.I.S System will show us the internal structure of the photon and makes us discover his propulsion means (img023 & img024)
We can also study the fields generated by its speed.

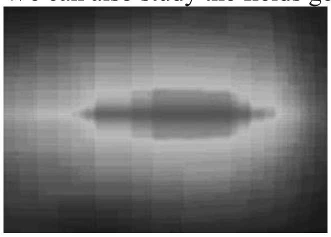
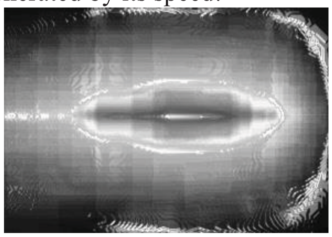

Img025 img 026

We note that the propellant is located inside the img022, as we are exploring the internal structure of the photon, we have the proof that the propulsion mode is done by energetic propellant, because its structure made of energy and non-material, we can conclude that according to the result images from V.I.S System, there exists an propellant surrounded by an energy shield or (energetic sail), it fulfills its propulsion function but it is made of energetic structure, it has no mass, but maintains its structure.

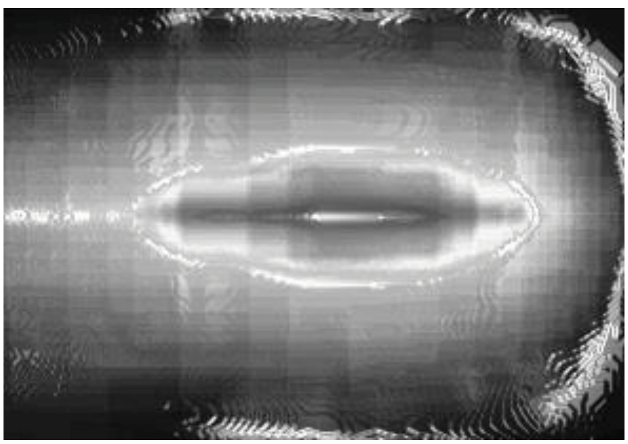

This image img027 shows us clearly the propellant is inside and by examining it at the height enlargement we see the cords which constitute the propellant, so in reality a photon is an energetic propellant. When a mass reaches the speed of light, it becomes energy, but will keep its structure; we see here the propellant was structured by energy, while keeping his mission of propulsion. So what include follows from all this, in reality the photon which is an propellant, that's what gives it its constant speed, which is energetic , when a mass reaches speed of light and more it becomes energy but keeps his original mass structure initial while keeping his physical properties.
To get an accurate picture of the propellant we will continue to study image 023.

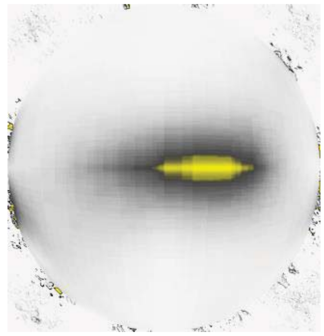
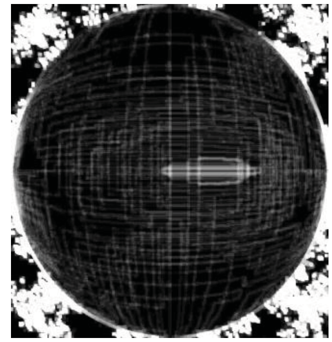

Img023 img028

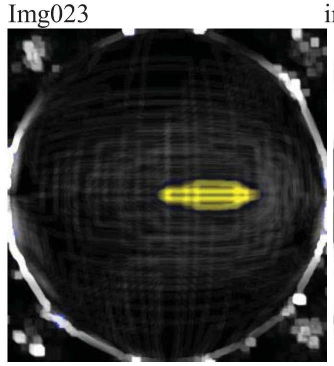
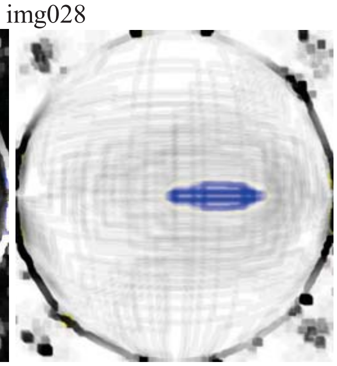

Img029 img030

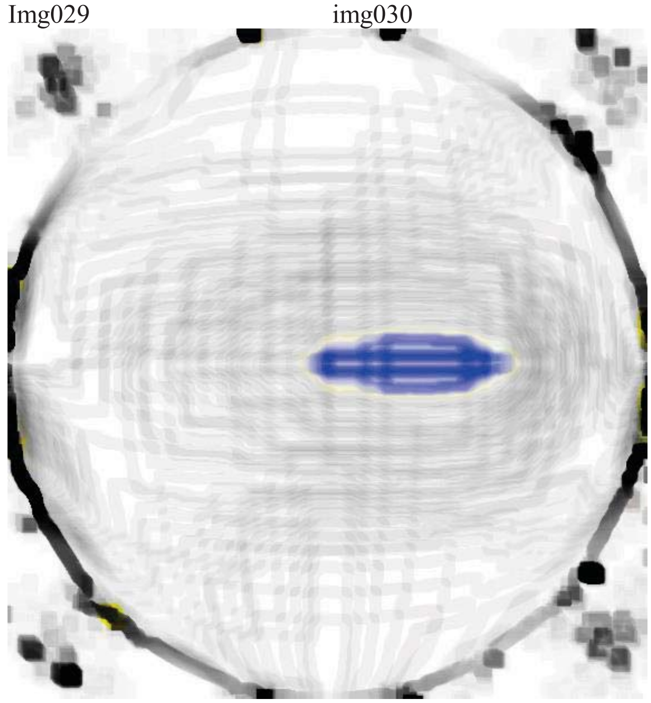

Img030 : enlarging

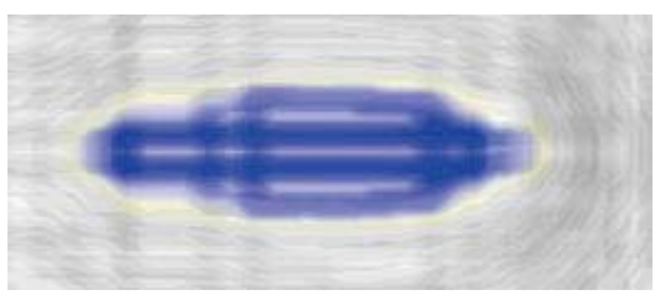

Img031

Enlarging image-030 shows us the true propeller structure as well as his position and its direction, so the proof is there, the photon is moved by a propellant, we have the real image as below.

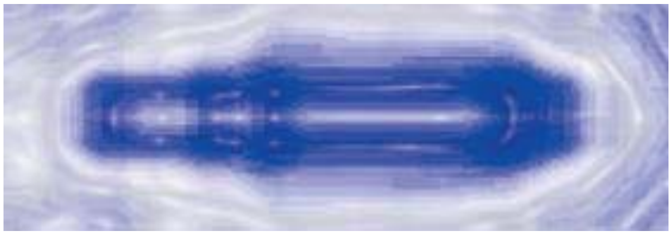

Img032

this propellant in img039 can be studied and reproduced by new technology engineers technique

Img033

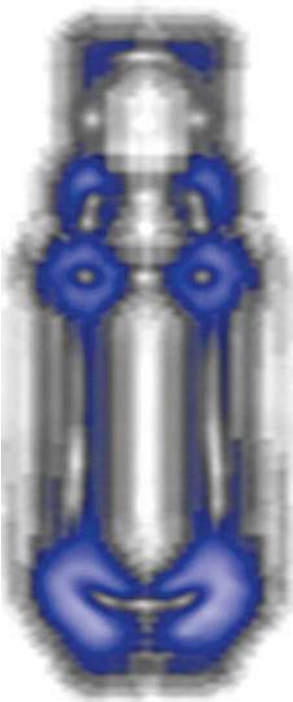

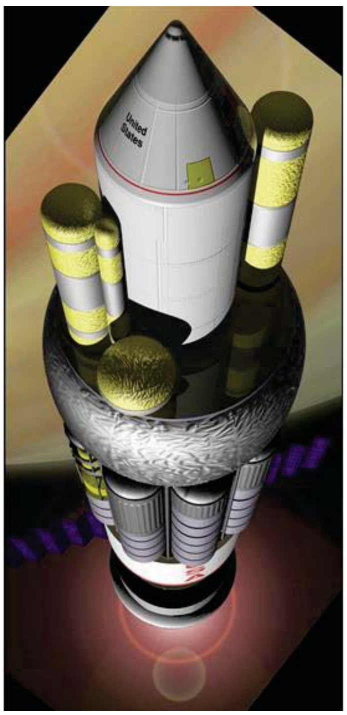

Img033 img034

Img033: which is propellant (or thruster) of the photon. **Img034**: image of "Orion" NASA project.

We can see clearly there is much similarity, namely the Orion project was the first design engineering of a spacial vehicle by nuclear thrust propulsion.

1- quel est son moyen de propulsion ?

The propulsion means of the photon which is done by a propeller energetic structured

2- Why a propulsion at this speed ?

The propellant is energy (almost zero mass) which causes to move very high speed. We can see it through images.

Img035 img036 img037

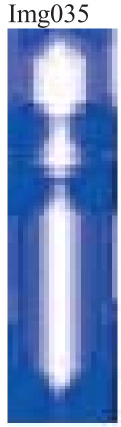

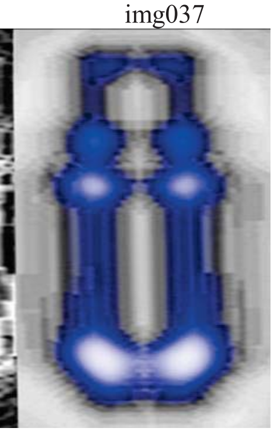

Img038 img039 img040

Img036 and img037 show us the propellant speed rotation of the Photon as well as all constitution details, the three parts from top to bottom, clearly distinct, this propellant in img039 can be studied and reproduced by new technology engineers technique, we can see the central part is dense, as well as rotational movement is well represented.

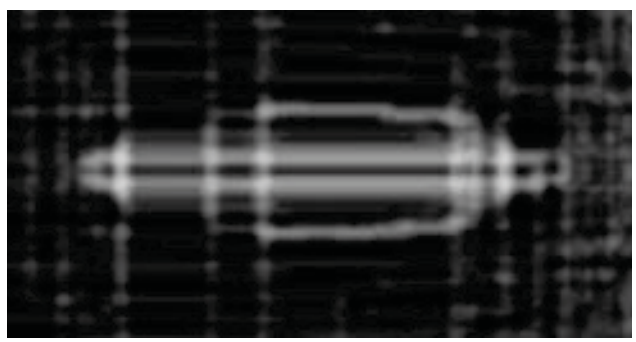

Img041

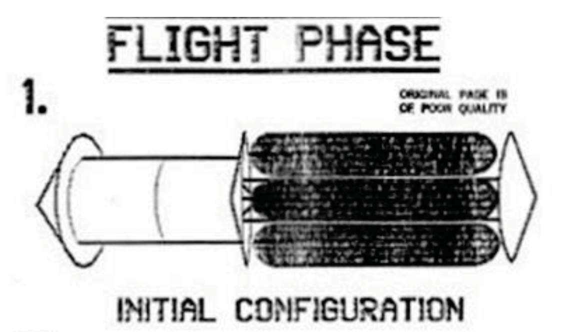

Img042 : comparative

The img042 and img034 show us the similarity with sketches img040 which represents the diagram done by US Navy in draft to build a spacecraft can travel at light speed.

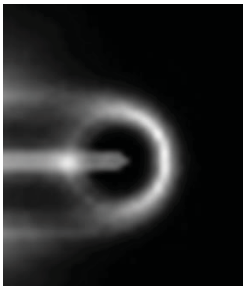

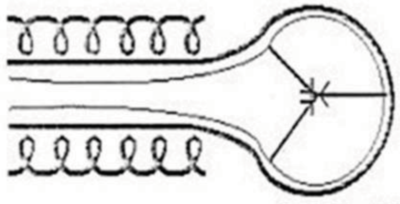

Img044 img045 : comparative

Img040 represents the energy field generated by the energetic propellant in real image, however the img044 which is a diagram of the calculated energy field represented schematically in US Navy project.

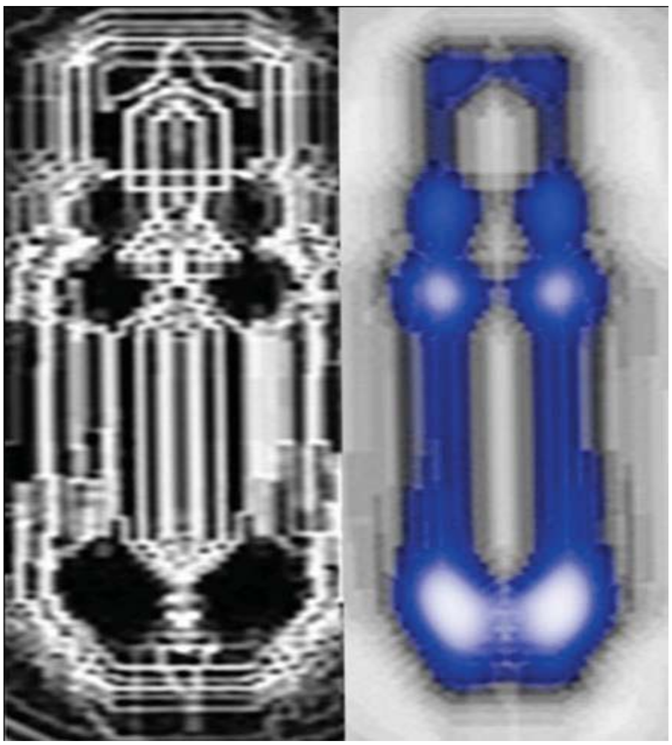

3- Path itinerary ?

Any object which moves follows a precise track programmed in its database use an instrument like a GPS which gives the way between departure place to the destination, while avoiding the obstacles and the long way.

The structur of GPS is made of electronic circuits allowing the geolocalisation of an object anywhere.

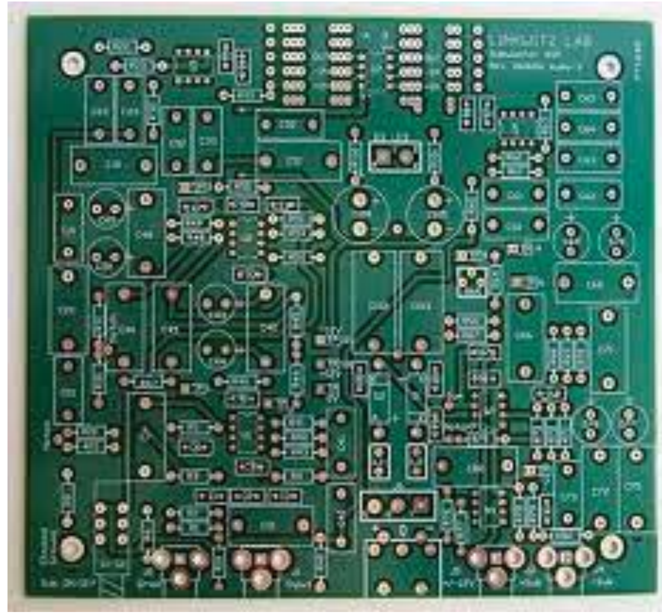

img046

Image 046 representative the Printed circuit board of GPS, which locates the enderoit environmental through satellites,

The shield of the photon (external structure of the photon) which is like a GPS, it collects all environmental information and coordinate them with its own informations

we see it in below images:

Img047

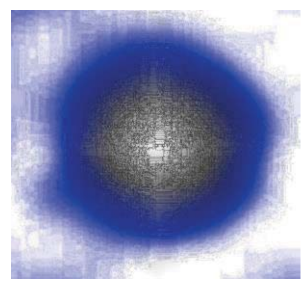

img048

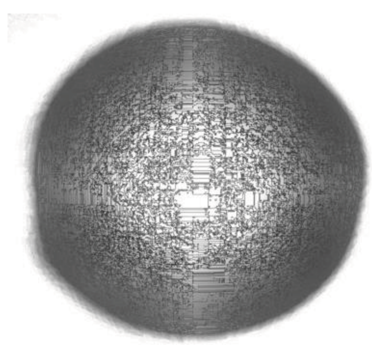

Img049

Img049 (enlarging of image 048)

Img047 which is photon image by V.I.S system, enable us to visualize its external structure, and we discovered a tangle of very complex circuit like a computer circuit network,

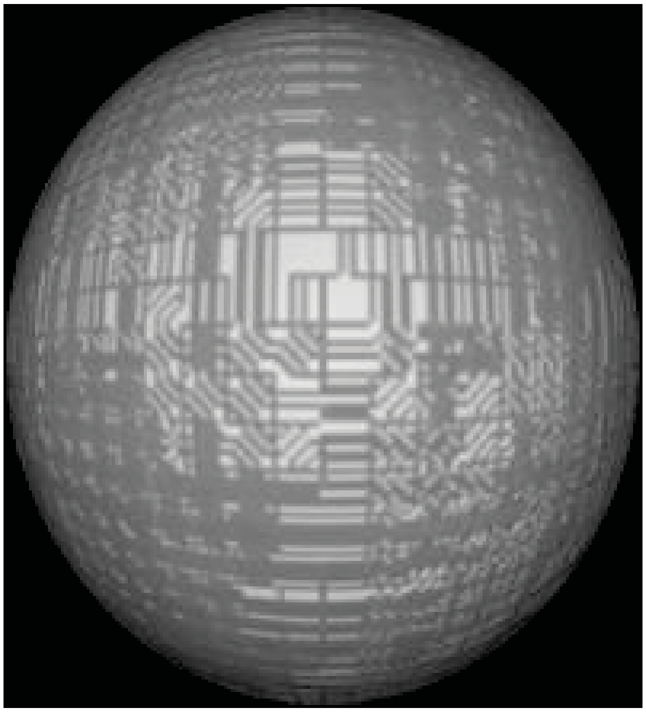

Imgo50

This shield is itself an assembly of tangle circuit connections which according to my humble opinion is used as immense fabric of networks containing information relating to operation of energetic propellant., we will proceed to a series of enlarging to see and understand the complexity of these computer networks of the shield created by energetic propellant, this is possible without pixellisation effect, considering the result image by V.I.S system is “Data Bank” image i.e. it results from a photonic binary algorithm and not of a digital00 binary system. (I already explained in the previous publications in WorldCom’11, WorldComp’13 and worldComp’14).

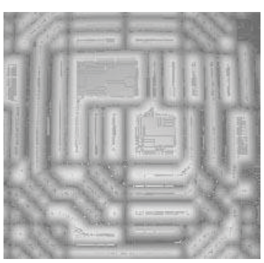

Img051

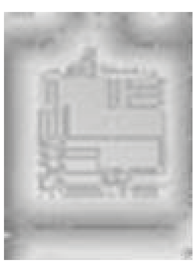

img052

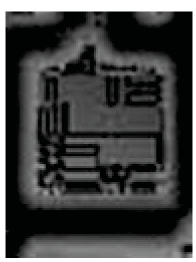

img052 négatif

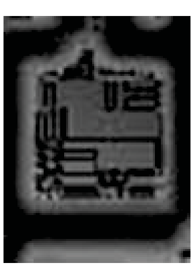

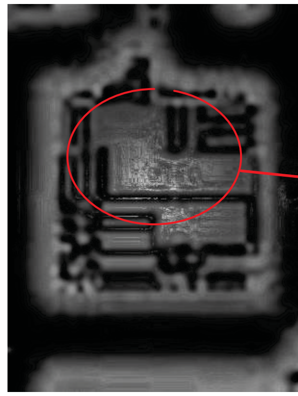

Img052

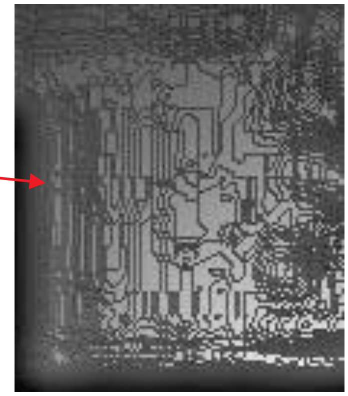

img053

Img053

img054

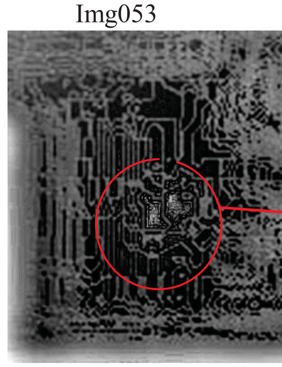

Img054

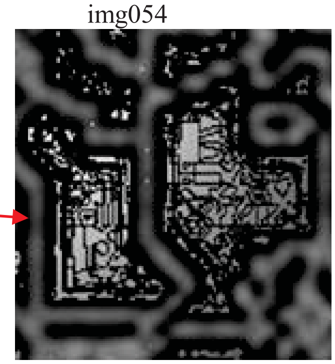

img055

Img055

img056

And so on, these computer circuits are arranged to interact in many ways and over several floors, this shows us the great complexity of this information navigations and universal positioning system. The images speak about themselves, no current technology can visualize neither to draw these circuits, nor these interconnections, the principle of "DATA BANK" image, allows us to visualize in real images, a true exploration in the infinitely small world.

we remind which is it "DATA BANK" image as I have already explained in the last conference (in WorldComp'11, WorldComp'13 et WorldComp'14) une image « Bank de données » est une image formé par un algorithme photonique, elle est formée d'une infinité d'images contenues dans l'image elle-même, toutes ces images contiennent les informations relatives aux informations de l'objet auquel on a pris cette image, à l'instant T ou on l'a pris c'est donc une infinité d'images contenues dans une seul image, au contraire de l'image prise par un algorithme numérique qui est unique et qui ne représente que l'aspect extérieur de l'objet photographié , si on procède à une très grand agrandissement de l'image numérique nous observons une pixellisation au-delà de laquelle l'image est flou , au contraire de l'image photonique prise par un algorithme photonique dont le 0 et le 1 sont remplacés par « les couleurs » et « les formes » il n'y a pas de pixellisation , plus on agrandit l'image plus les détails apparaissent , et ceci jusqu'à l'infiniment petit .(schéma pour expliquer)

Digital images coding:

How are the multimedia contents, particularly, the images coded in the computer? In the computer science each information «text, picture, sound…» is coded under a binary form which means 0 and 1. The smallest information unit is called *«bit» «binary digit»*, a set of 8 bit is called *«byte»*.
A *byte* enables to store a letter, a figure. This grouping of numbers by set of 8 enables the best legibility similar to what we appreciate on decimal base, to group the figures by three in order to distinguish the thousands, Eg: 1 256 245 is more legible than 123245.

How the information is coded in binary system?
For the figures operation is carried via a reconversion in base 2. A natural who he is a positive whole or nil. The number of figures that we want to use. With 1 byte it is possible to obtain 2 (= 2_1) value : 0 and 1
A natural number is a positive integer or zero. The number of bits to use depends on the range of numbers that you want to use. With a bit, it is possible to get 2 (= 2_1) values: 0 and 1
With two bits it is possible to represent 4 (= 2_2) different values: 00, 01, 10 and 11 With a byte (8 bits), it is possible to represent 256 (= 2_8) values or the integers between 0 and 255
For a group of (n bits), it is possible to represent (= 2_n) values or integers from 0 (= 2_n).

So how can we count with 4 bits? With 24 bits?
The base (2) operate exactly as the base (10); except for exactly for its mesur unit. Ex : in base (10) « eleven » is written «11» either «$10_0 + 10_1$».

In base (2) «eleven» is written as «1011» either «$2_0 + 2_1 + 2_3$» ($1*2_0 + 0*2_1 + 1*2_2 + 1*2_3$) n base-2, « onze » s'écrit « 1011 » soit «$2_3 + 2_1 + 2_0$» ($1*2_3 + 0*2_2 + 1*2_1 + 1*2_0$) La valeur d'un octet est comprise entre 0 et 255.

The picture coding : Two categories of coding pictures

1. **Vectorial coding :** The picture is coded by a set of mathematic formulas.
2. **The Bitmap coding** : Image which is encoded as point table (matrix).

Vectorial image, bitmap image
Example: representation of a circle in vector or bitmap coding

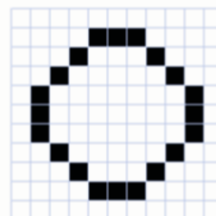

0	0	0	0	0	0	0	0	0	0	0
0	0	0	0	1	1	1	0	0	0	0
0	0	0	1	0	0	0	1	0	0	0
0	0	1	0	0	0	0	0	1	0	0
0	1	0	0	0	0	0	0	0	1	0
0	1	0	0	0	0	0	0	0	1	0
0	1	0	0	0	0	0	0	0	1	0
0	0	1	0	0	0	0	0	1	0	0
0	0	0	1	0	0	0	1	0	0	0
0	0	0	0	1	1	1	0	0	0	0
0	0	0	0	0	0	0	0	0	0	0

Exemple 01: Image represented by digital binary coding

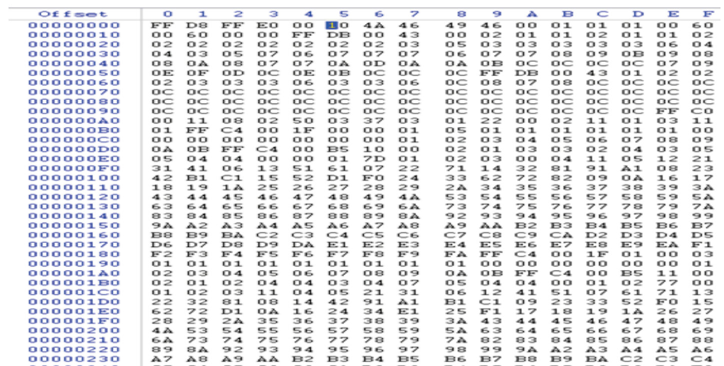

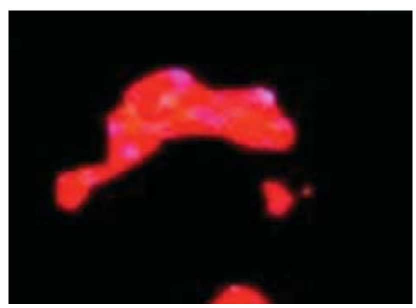

Exemple 02: Image represented by photonic binary coding

- **Form :** which replace **0**
- **Color :** which replace **1**

Forms : Generally all shapes can also be modelled with spheres , from the smallest point possible to infinity imaginary forms possible.

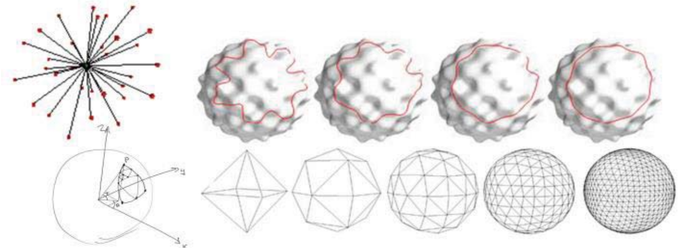

Colors: All colors possible exist (visible or not) which is located between the ultra-violet and infrared.

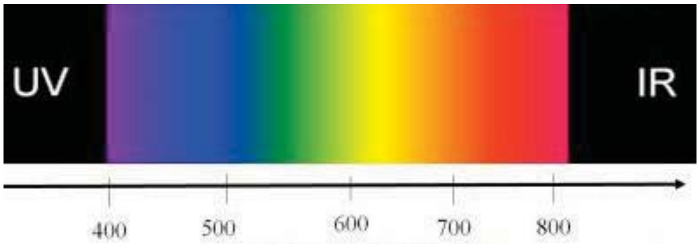

3 Conclusion

Starting from an image light particle, or photon, we made some very important discoveries and provided answers to questions that until now had no answer.

We have been explained from where the speed of the photon comes, we knew the photon which is a propellant (or thruster) made of energy, that we can visualiz it in real image by V.I.S System, The discovery is important, because for the first time one explains from which comes the speed of the photon in real images according to V.I.S System technique, The propellant images are amazing and extraordinary as well as their details & exactness, it has a specific energetic structure, as well as high speed with which it moves in the universe, and its high rotation speed on itself in the same time, its structure made of energy and non-material (null mass), futuristic sketch (in photos) for their project.

We conclude the high speed which it moves into space, and its high rotation speed on itself in the same time, make his own energetic shield (such as solar sail), in order to keep his global energetic state, as well as its protection against external elements.

We come also discover this energetic shield (or photonic sail) which is itself network of complicated computer circuits tangled among them into several levels, we remind that "quantum computer" diagrams, have multidimensional levels until infinitely small.

4 References

[1] Image 034 Orion project which was a design engineering of spacecraft driven by pulsated nuclear propulsion whose idea was proposed by Stanislaw Ulam.

[2] Image 039 and 041 Source: publication and work of US Navy on the possibilities of achievements of spacecraft exceeding light speed.

ISBN: 1-60132-429-4, CSREA Press ©